Plasmon-Mediated Photothermal Phenomena and Nanofabrication of Applicable Devices

by

Daniela Trinidad Marquez Soto

Thesis submitted to the
Faculty of Graduate and Postdoctoral Studies
In partial fulfillment of the requirements
For the Ph.D. degree in
Chemistry

Department of Chemistry and Biomolecular Sciences
University of Ottawa

To Aurora, Gabriel and Trevor

For the love and encouragement

&

To my mentor

Dr. Juan Cesar (Tito) Scaiano

If I have seen further,

It is by standing on the shoulders of giants.

Sir Isaac Newton

Abstract

This thesis studies the different ways in which the localized plasmon heating effect of gold nanostructures -activated by plasmon excitation *via* visible and/or NIR irradiation- can be used to obtain different outcomes following the nanofabrication of applicable devices. Both spatial and temporal control were obtained for each one of the systems developed upon the incorporation of plasmonic gold nanostructures.

Spatial control was enabled in hybrid mesoporous drug delivery systems fabricated in this thesis through the localized surface plasmon heating effect that allowed the modification of the dynamics of diffusion of the cargo being delivered, thus giving rise to different rates of release that can be controlled by plasmon excitation. At the same time, the plasmon heating effect proved to be capable of controlling the start of the release by dismantling thermo-responsive gates previously incorporated, thus enabling also a wavelength-controlled feature that enhances the versatility of these systems.

Spatial control was also conferred to the photo-patterning applications presented in this dissertation by influencing the degree of motility of gold nanorods (AuNRs) embedded in polymer matrices allowing them to self-assemble when the longitudinal plasmon of the incorporated nanostructures was excited; the patterns generated were quite robust and persisted for extended periods of time.

Finally, the feature of spatial heating control was also conferred to catalysis. The Friedel-Crafts alkylation of anisole by benzyl chloride using spherical gold nanoparticles (AuNPs) supported on Nb_2O_5-based catalysts was performed at bulk temperatures below those necessary for the reaction to occur when using bare or modified Nb_2O_5; this was the result of the combination of bulk and localized plasmon heating produced -both- *via* plasmon excitation. This also demonstrates the possibility of using plasmon excitation as an alternative heat source in this type of reactions.

By combining the plasmonic properties of metallic nanostructures with those granted by mesoporous materials, polymer matrices and Nb_2O_5-based materials it was possible to obtain light-activated systems endowed also with temporal control and wavelength control while preserving the original properties of each systems' components.

Overall, the content of this thesis describes in detail the practical aspects of combining gold nanostructures with different materials and the rationale behind the development of systems with customized and controllable properties.

Acknowledgements

When I look back and remember the day I tapped Tito's shoulder at a conference, on the other side of the world, and introduced myself -out of nowhere- to ask for an opportunity it seems unreal. All I had was the initiative and the passion to become someone better and he believed in me without a doubt. It is impossible to express with words the immense gratitude and admiration I feel for you. Thank you for being such an amazing supervisor, for your continuous support, patience, incredible knowledge, for showing me how stunning and fulfilling science can be and for waking up in me the passion for challenge. Above all, I would like to thank you for being there when I needed it the most and for the infinite number of life lessons, starting from the first one you gave me when I tapped your shoulder; to believe in others.

During the years spent in the Scaiano Lab I met wonderful people whose contributions at a scientific and personal level make me be who I am today. I would like to thank you all -previous and current members- for making this journey so enjoyable and for being a great team to work with. Special thanks to my dear friend Anabel Lanterna for the infinite number of deep conversations, countless laughs and for waking up in me the love for "mate". Many thanks to Mr. Michel Grenier for his impressive professional support, for every single joke and all the great times we had working together. I am also very grateful for having the opportunity to meet my friends Emilio and Charles as well as Betty Yakimenko who supported me all along and helped me at all times; thank you for being there.

I will always be grateful to my friend Marcela for these 18 years of friendship. In spite of the distance, you have always known how to support me and encourage me; even in the craziest projects.

My most sincere gratitude to my parents -Aurora and Gabriel- for their infinite support. Thank you for so much love and encouragement, for sacrificing all you have to give me wings and for teaching me to never give up. I love you with all my heart; every single accomplishment is as yours as it is mine.

To my husband Trevor, thank you for being the best life partner and friend I could have ever asked for. Without you this would have never been possible. I will be always grateful for your love and encouragement and I look forward to continue enjoying this life journey by your side.

To my Canadian family, thank you for making me feel at home and for showing me how gorgeous Canada is.

Contents

List of Figures

List of Tables

List of Acronyms

APTES aminopropyl triethoxy silane

AR aspect ratio

AuNPs gold nanoparticles

AuNR gold nanorods

BET Brunauer-Emmett-Teller method

BJH Barret-Joyner-Helender method

CB6 cucurbit[6]uril

CB7 cucurbit[7]uril

CPTES 3-chloropropyl triethoxysilane

C$_{SS}$ concentration of super saturation

C$_{16}$**TAB** cetyltrimethylammonium bromide

C$_{12}$**TAB** tetradodecyltrimethylammonium bromide

DR diffuse reflectance

FT-IR fourier transform infra-red spectroscopy

GC-FID gas chromatography-flame ionization detector

HAuCl$_4$ $\cdot$ **3**H_2**O** tetrachloroauric acid

Hex hexanediamine

ICP-AES inductively coupled plasma-atomic emission spectroscopy

IR infra red

IUPAC International Union of Pure and Applied Chemistry

I-2959 hydroxy-1-[4-(2-hydroxyethoxy)phenyl]-2-methyl-1-propanone (Irgacure-2959)

LED light emmiting diode

LSPR longitudinal surface plasmon resonance

SPP surface plasmon polariton

SPR surface plasmon resonance

TSPR transverse surface plasmon resonance

MCM-41 Mobil Composition Matter No. 41

MSA mercaptosuccinic acid

Nap naproxen

Nb_2O_5 Niobium Pentoxide

NIR near infra red

NMR nuclear magnetic resonance

PDMS polydimethylsiloxane

PEG poly(ethylene)glycol

PMMA polymethyl metacrylate

PPG poly(propylene)glycol

PTC phase transfer catalyst

PTI photon technology international

P-123 pluronic acid

SBF simulated body fluid

SDAs supramolecular directing agents

SEM scanning electron microscopy

SPB surface plasmon band

TEM transmission electron microscopy

TEOS tetraethyl orthosilicate

TGA thermogravimetric analysis

THAM tris(hydroxymethyl)aminomethane

TOAB tetraoctylammonium bromide

XRD X-ray diffraction

Chapter 1

Introduction

1.1 Noble Metal Nanoparticles

1.1.1 Noble Metal Nanoparticles in Ancient History

In the past 200 years many scientist have focused on the colloidal state of matter and physical properties of noble metal nanoparticles (Au, Ag, Cu) motivated by the size dependence of their physical properties, which highlights their potential for an almost infinite number of applications. However, the use of noble metal nanoparticles dates back to much earlier times.

The ancient empires are well known for their impressive architectural and artistic skills, admired until today. Even though their expertise seems to be related to impressive large-scale engineering pieces their dexterity also applies to the other side of the size spectrum, the nanoscale. Surprisingly, they specialized in the art of manipulating bulk materials by adding nanoscale particles in order to improve and/or tune their properties; a concept known in the modern days as nanocomposite fabrication.

Several examples exist related to ancient nanocomposites such as the famous Lycurgus Cup -manufactured by the roman empire about AD400. The cup is made of glass and possesses the remarkable property of adopting different colors depending on where light is shone from. When viewed in reflected light such as daylight, it appears green (Figure 1.1, left panel). However, when light is shone from its inside and transmitted through the glass it adopts a red color (Figure 1.1, right panel).

Upon qualitative spectrographic analyses performed by the British Museum and the General Electric Company Ltd. it was concluded that the phenomenon observed in the Lycurgus cup was due to light scattering and suggested that gold/silver alloy nanoparticles -incorporated during the manufacturing process- contributed to the color; the gold component is mainly responsible for the reddish transmission and the silver for the greenish reflection.[1]

Figure 1.1: Lycurgus cup manufactured in the ancient Rome. Left: Green color adopted due to light reflection; Right: Red color adopted due to light transmission.©Trustees of the British Museum.

Like the Lycurgus cup, there are many other examples related to the development of nanocomposites in ancient times such as the improved strength Damascus steel swords made between AD300 and AD1700, the very stable Maya Blue pigment and the use of nanoparticles in textile dyes, among others. Eventually, through the ages, many more nanocomposites were developed including the incorporation of nanoparticles for stained glass in the medieval times. However, intuitive nanotechnology antiquities were developed spontaneously, without proper understanding of the nature of the phenomena occurring during-synthesis and post-synthesis.

1.2 Some Theory on Metallic Nanoparticles

Considerable efforts made in the past two centuries towards the elucidation and description of the properties of metallic nanoparticles have shown that the size of the object plays a key role in defining the properties of the material being studied. Almost all physical and chemical properties present a dramatic size dependence being responsible for the remarkable differences when going from bulk to nano size. A decrease in the size to a few nanometers leads to materials that exhibit peculiar properties such as increased fracture strength, hardness, chemical selectivity and surface energy. Unlike in bulk, the interaction of noble metal nanoparticles with light results in the resonant absorption of light meaning that the excitation of the electrons on their corresponding conducting band results in an oscillating behavior.[2]

The above mentioned collective oscillating response of the electrons in the conduction band of a noble metal nanoparticle upon excitation by an external electromagnetic field is commonly referred to as localized surface plasmon polariton (SPP). However, this definition is based only on one of the components that sustain a surface plasmon rather than depict what an SPP really is, leaving out key components, important phenomena and requirements that ensure its existence.

It is important to comprehend the two main phenomena that interrelated define an SPP in order to achieve a more accurate depiction and a deeper understanding. This can be done by initially analyzing the phenomena of collective oscillation and surface wave generation separately, to then relate them and obtain a definition for the localized surface plasmon. Furthermore, the surface wave generation phenomenon and how it relates to the oscillation of electrons to produce an SPP and then allow its existence are fundamental to obtain an accurate definition.

1.2.1 Oscillating Behavior

The collective oscillation phenomenon can be better understood by starting from a dielectric material to then extend the theory to metal slabs and finally relate it to metal nanoparticles. Even if it initially seems counter-intuitive to relate noble metal nanoparticles with dielectric materials most of the parameters used for describing the latter -including a modified version of their behavior- can be used to describe -in a simple and general way- a surface plasmon polariton.

Dielectric Materials

A simple analogy can be made between an electron cloud around a nucleus and a solid fixed object attached to a mass suspended on a spring, in the presence of a damper that accounts for loss (see Figure 1.2). As long as there is no force applied to the mass, the system will remain unchanged in an equilibrium state.

A similar situation applies for an electron cloud around a nucleus since the former will remain symmetric in the absence of an electric field. When the mass connected to the spring gets pulled or, alternatively, an electric field is applied -imparting forces on the electron charge- the nucleus gets pulled in one direction and the electron cloud on the other direction due to their opposite charge. The electrons will then spend more time on one side of the nucleus inducing a dipole moment and an off set charge, making the material to be polarized.

If the mass on the spring was released, it would bounce back and forth. Analogous to this, if the electron field was removed the electron cloud would move back and forth on either side of the nucleus -due to a restoring force- resonating at a certain frequency. When an electric field is applied to a dielectric material the polarization from atom to atom varies randomly so when the interest is focused on the macroscale a statistical polarization average must be taken into account.

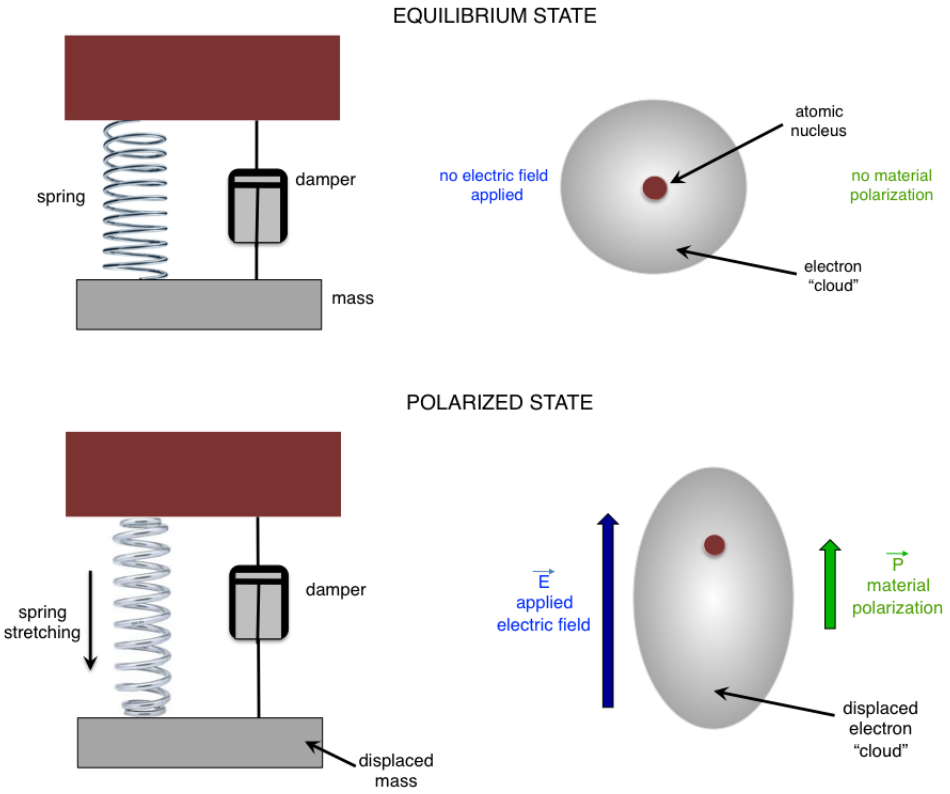

Figure 1.2: Graphical representation of the analogy between an electron cloud and a mass on a spring.

Metal Slabs

In metal slabs, the electrons on the conduction band can be considered free because they are not bound to a nucleus. Hence, the restoring force can be considered negligible. When free charges move around they collide with each other producing loss. Thus, it is often more meaningful to express the loss in terms of collisions. It is worth to mention that in a real material there are multiple resonances contributing to the oscillating behavior.

1.2.2 Surface Waves and Surface Plasmon Polaritons (SPP)

In order to understand the second main phenomenon occurring when an SPP is generated it is necessary to understand what surface waves are. To fulfill this purpose, an infinite half space approximation must be applied. Figure 1.3 (left) shows materials A and B joined by an interface. Material A and B -separately- are a region in space bound at only one edge (interface) to the other material, each of them extending to infinity in all the other directions. Hence, A an B are infinite half spaces. Surface waves are commonly analyzed in the context of a superstrate -material A- and a substrate -material B- being infinite half spaces.

In terms of traditional guided modes, Figure 1.3 (right) shows a slab waveguide composed by a core and a cladding on either side. The core (dark gray) has a higher refractive index than the cladding (light gray). Hence, within the core, a wave will travel slower than in the cladding making it to be compressed.

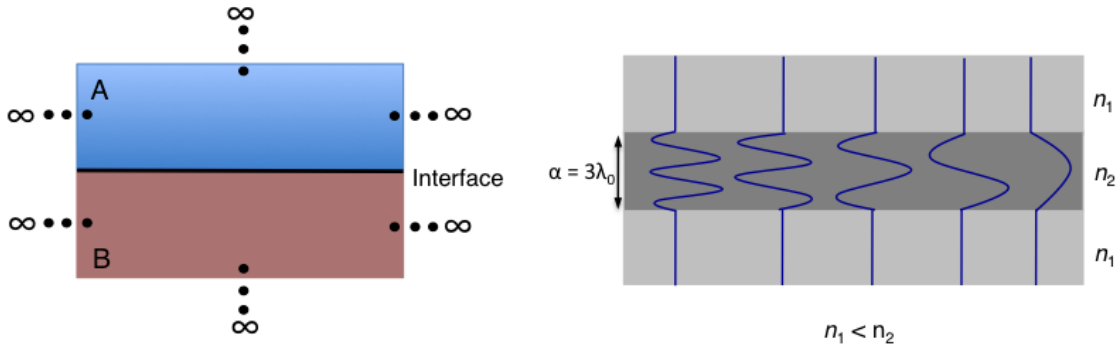

Figure 1.3: Graphical description of infinite half spaces (left) and traditional guided modes (right).

A spatial period at the core-cladding boundary will be produced when a wave is compressed in the core and the cladding's refractive index is sufficiently low. Therefore, the wave will be cut off in the cladding being only supported in the core.

This can also be thought as the core-cladding interfaces being able to support total internal reflexion so the modes shown in the core could be depicted as rays bouncing inside.

A surface wave is analogous to a slab waveguide with the exception that the mode is confined to the interface between two materials comprising two infinite half spaces (see Figure 1.4). The field decays exponentially away from the interface having a certain skin depth -that corresponds to the distance a wave can travel inside the material- yet it is free to propagate without decay on the plane of such boundary. Due to increased interaction, the field right at the interface travels more slowly generating a spatial period -analogous to the one described for traditional guided modes- that varies very abruptly preventing the wave to be supported in either the superstrate A or the substrate B, giving rise to what is called a surface wave.

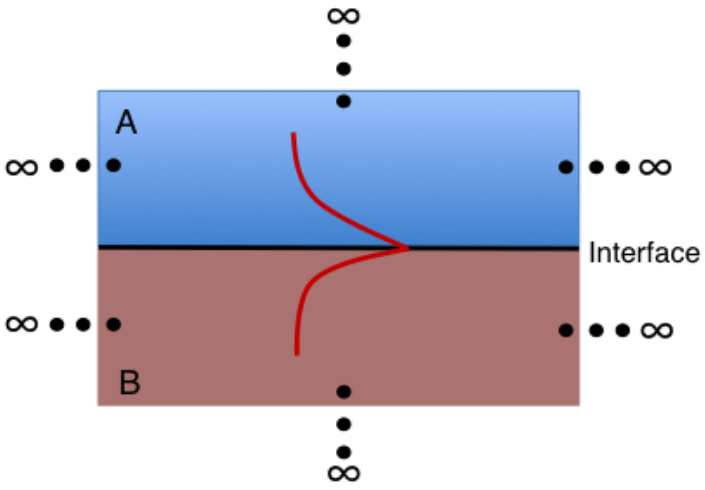

Figure 1.4: Graphical description of a surface wave.[3]

Panel A of Figure 1.5 represents an incident wave traveling from a lower to a higher refractive index material at no specific angle. The incident wave transmits into the higher refractive index material in a more compressed manner. By looking at the interface it is possible to qualitatively see how fast the field is varying at the interface.

As a mode of comparison, panel B shows the opposite scenario where a wave is traveling from a higher refractive index to a lower refractive index material. In this case, transmission is also observed since the incident angle is smaller than the critical angle. Lastly, when the incident angle θ_1 is greater than the critical angle θ_C the incident wave is compressed enough in the material with higher refractive index such that at the interface is varying too abruptly to be able to be supported in the bulk of the lower refractive index material (Figure 1.5 C).

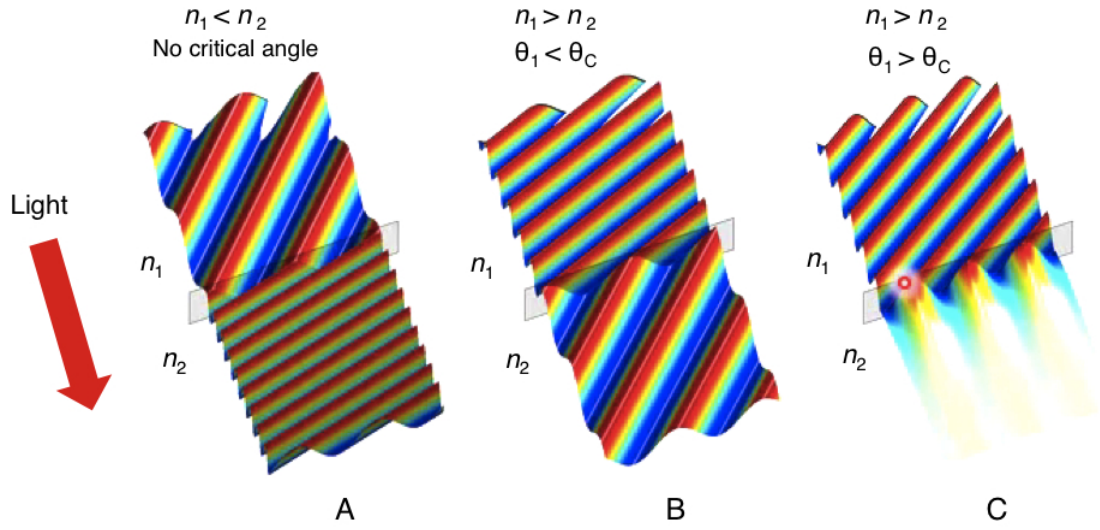

Figure 1.5: Graphical description of a wave going through two materials with different refractive indexes.[3]

Surface Plasmon Polaritons (SPPs)

The area of research focused on surface plasmon polaritons is very active and currently considered a "hot topic" due to the very useful propagation characteristics and the possibilities of miniaturization that SPPs can confer.[4, 5]

When an SPP exists there are two main phenomena occurring at the same time. As described, a collective oscillation of electrons is produced as a response to an electric field being applied. On the other hand, when coupling occurs between the oscillation of electrons and the electromagnetic modes, both travel as a package and a surface wave is generated. The charge periodicity granted by the oscillation of the electrons will constitute a key factor for the surface wave to be maintained. Since the surface plasmon polariton penetrates both materials when propagating, the frequency of the light guided will depend on the dielectric constant of both of materials. Furthermore, the dielectric constant of the surface will also affect the frequency of the guided light making it change drastically upon surface functionalization.

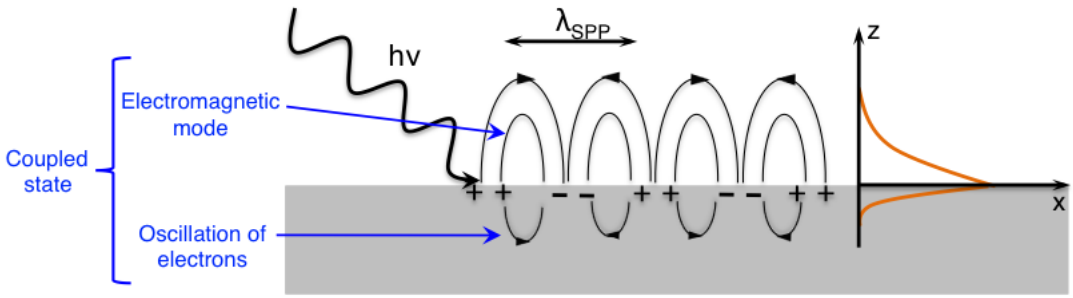

Figure 1.6: Graphical description of a surface plasmon polariton.

The analysis presented in this chapter permits to convey that an SPP is a surface wave produced by the coupling between the electromagnetic modes of the incident light and the collective oscillation of electrons generated when the system is perturbed by the application of an electromagnetic field. This wave is capable of being maintained by the periodicity granted by the oscillation of electrons described by parameters intrinsic to the material such as susceptibility and dielectric function.

Localized Surface Plasmon Polariton in Noble Metal Nanoparticles

A noble metal nanoparticle can be viewed as a small version of a metal slab. If we recall the skin depth concept -which indicates the distance a wave can travel inside the material- we have that nanoparticles are small enough to cover that skin depth allowing the surface plasmon to penetrate through the entire particle. As a result, the electromagnetic wave is trapped in the particle and the totality of the electrons on the nanoparticle's conductive band oscillate together producing a systematic change on the charge of the surface of the nanoparticle while coupling with the incident wave. Since the propagation of the wave is confined to the nanoparticle the phenomenon is described as a localized surface plasmon (see Figure 1.7).

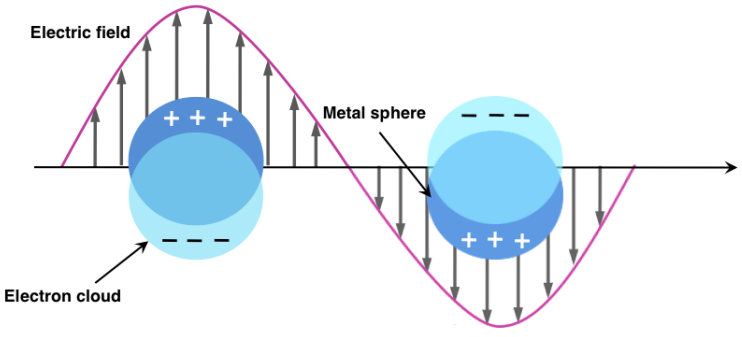

Figure 1.7: Diagram illustrating the localized surface plasmon of a spherical metal nanoparticle, adapted from ref. [6]

The effect of reduction of the incident light generated when light interacts with a metallic nanoparticle -producing a localized surface plasmon- is called extinction and translates into the emission of secondary radiation called scattering. Furthermore, part of the radiation is also extinguished within the particle due to absorption, a consequence of the collision between the oscillating electrons.

In 1908, Gustav Mie described for the first time the phenomenon of particle-light interaction employing the concept of electromagnetic wave and Maxwell's equations to derive the incident, scattered and internal fields. The morphology-dependent resonance feature is of particular interest; various particle resonances are generated by varying the particle size parameter defined as

$$\chi = \frac{2\pi r N_{\mathrm{m}}}{\lambda} \tag{1.1}$$

where, r corresponds to the radius of a particle and $\lambda/\ \mathrm{N_m}$ denotes the wavelength in a surrounding media of refractive index $\mathrm{N_m}$. At a size regime where the radius is much smaller than the wavelength (r $<<\lambda$) only a dipolar mode contributes significantly to absorption and a simplification of the Mie's theory allows to determine that the ability of the particle to absorb light -called polarizability- can be described as

$$\alpha = 3\epsilon_0 V \frac{\epsilon - \epsilon_{\mathrm{m}}}{\epsilon + 2\epsilon_{\mathrm{m}}} \tag{1.2}$$

where, α corresponds to the polarizability, ϵ_0 is the free space permittivity, V is the volume of the particle, ϵ is the permittivity of the material, and ϵ_{m} represents the permittivity of the surrounding medium. Resonance primarily occurs when the ability of the particle to absorb light is at its maximum. From equation 1.2 is possible to see that this condition is satisfied when

$$\epsilon = -2\epsilon_{\mathrm{m}} \tag{1.3}$$

indicating that particle resonance may originate from the optical constants of the bulk material. Equation 1.3 is satisfied when the real part of the dielectric constant is negative as in the case of gold, silver and copper nanoparticles, which can support the plasmon absorption.

The phenomena of absorption and scattering of a metallic spherical particle are related directly to the polarizability by

$$Absorption = kIm(\alpha)\ ;\ Scattering = \frac{k^4}{6\pi}|\alpha|^2 \tag{1.4}$$

where Im(α) is the imaginary part of the dielectric constant, while k is the wave vector of light described by equation 1.5.

$$k = \frac{2\pi\epsilon_m^{1/2}}{\lambda} \tag{1.5}$$

When the symmetry of a particle is broken -as in the case of noble metal nanorods- a particle gains additional plasmon resonance modes which translates into two SPR absorption bands, namely a transverse (TSPR) and a longitudinal (LSPR) localized surface plasmon, see Figure 1.8.

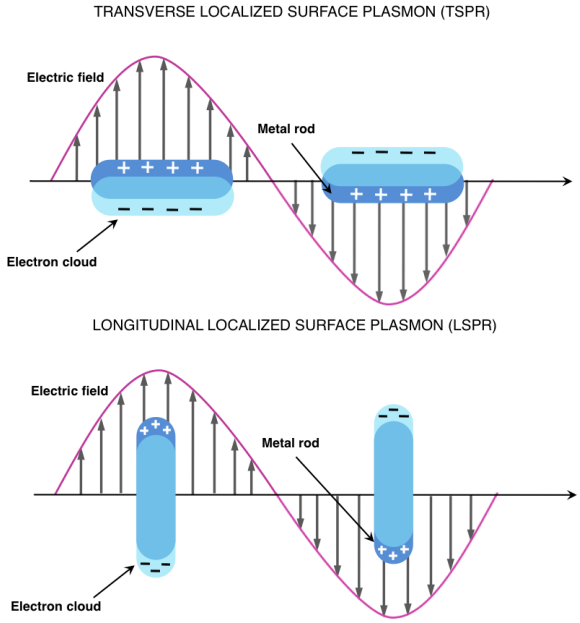

Figure 1.8: Diagram illustrating the transverse (top) and longitudinal (bottom) localized surface plasmon of a metal nanorod.

The optical properties of gold nanorods can be described based on the Gans model for ellipsoids -proposed in 1912- in which the polarizability of metallic ellipsoids is given by

$$\alpha_{x,y,z} = \frac{4\pi abc(\epsilon - \epsilon_m)}{3\epsilon_m + 3L_{x,y,z}(\epsilon - \epsilon_m)} \tag{1.6}$$

where, a,b, and c correspond to the length of the ellipsoid along the axes x,y, and z, respectively, ϵ is the permittivity of the material, ϵ_m refers to the permittivity of free space, and $L_{x,y,z}$ is the depolarization factor for the respective axes which in turns depends on the ellipticity of the particle.[7] As can be seen, the absorption of AuNRs depends on the aspect ratio rather than on the absolute dimensions of the particle.

Noble metal nanorods are more easily polarized longitudinally than transversaly meaning that the LSPR occurs at lower energies, hence, the absorption of the LSPR occurs at higher wavelengths.

Localized Surface Plamon Effects

Various effects of plasmon excitation on the surface and immediate surroundings of the nanostructures are described by Figure 1.9. The characteristic large absorption coefficients of metallic nanostructures - 1 x 10^9 $M^{-1}cm^{-1}$ for a 20 nm gold nanoparticle containing approximately 250,000 atoms [8]- can result in antenna effects promoting energy transfer and consequently the generation of excited states when a suitable receiver is present in the vicinity of the nanostructure. The mechanism behind these observations is known as Non-radiative Resonance Energy Transfer (NRET), also known as Förster Resonance Energy Transfer (FRET) and occurs by the coupling of a donor and an acceptor through dipole-dipole interaction. The energy transfer rate for FRET between molecules varies to the power of 6 with the inverse of the distance (R^{-6}) for a non-radiative transfer. However, in the case of AuNPs the transfer rate varies to the power of 4 with the inverse of the distance (R^{-4}) and results from the coupling of the AuNP's plasmon resonance and the acceptor.[9]

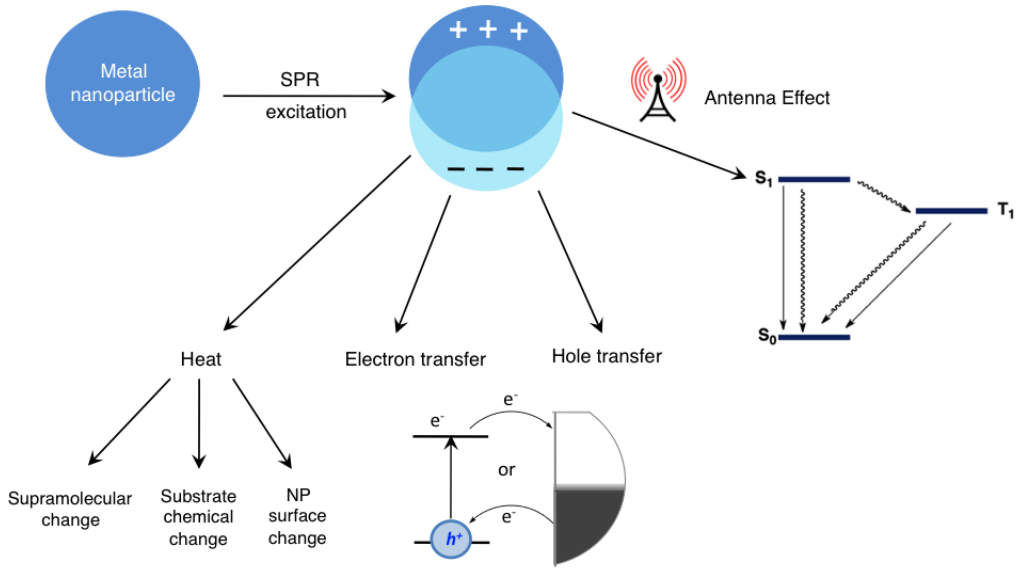

Figure 1.9: Diagram illustrating the various effects of a localized surface plasmon, adapted with permission from [10]. Copyright (2017) American Chemical Society.

Under plasmon excitation, the nanostructures can also engage in electron transfer or hole transfer in the presence of excited molecules, acting either as an electron donor or electron acceptor.

The decay of the localized surface plasmon is very fast -lifetime in the order of a few femtoseconds- and proceeds through dephasing of the collective oscillation of electrons mostly through thermal relaxation. It has been reported that the thermal characteristic of the plasmon relaxation can lead to elevated surface temperatures capable of inducing chemical and/or physical changes at a molecular and supramolecular level as well as -in some cases- changes of the surface of the nanoparticle itself. In the past three decades, the above mentioned plasmon effects have been extensively used in innovative applications, especially related to photo-patterning, drug delivery and catalysis, including the ones found throughout this thesis.

1.3 Synthesis of Metallic Nanostructures

1.3.1 Spherical Nanoparticles

Along the decades, several methods for the preparation of spherical metallic nanoparticles have been developed with the aim of controlling its size, morphology and surface structure ultimately determining their physical and catalytic properties.[11, 12, 13, 14] A chemical approach involves a variety of methods in which a reducing agent is used in solution to transform a source of cations (M^{n+}) -usually a salt- into the corresponding metallic species (zero oxidation state, M^0).

The process can be described by the following general equation:

$$M^{n+} + ne^- \rightarrow M^0 \rightarrow\rightarrow\rightarrow MNP \tag{1.7}$$

The size distributions obtained upon synthesis have shown to largely depend on the rates of nucleation and growth; two important processes that constitute the basis of nanoparticle formation.

Nucleation and Reaction-Limited Growth

In 1950, Lamer and Dinegar proposed a mechanism for explaining the formation of metallic nanoparticles.[15] Figure 1.10 illustrates the proposed mechanism upon mixing of the metal precursor and the reducing agent.

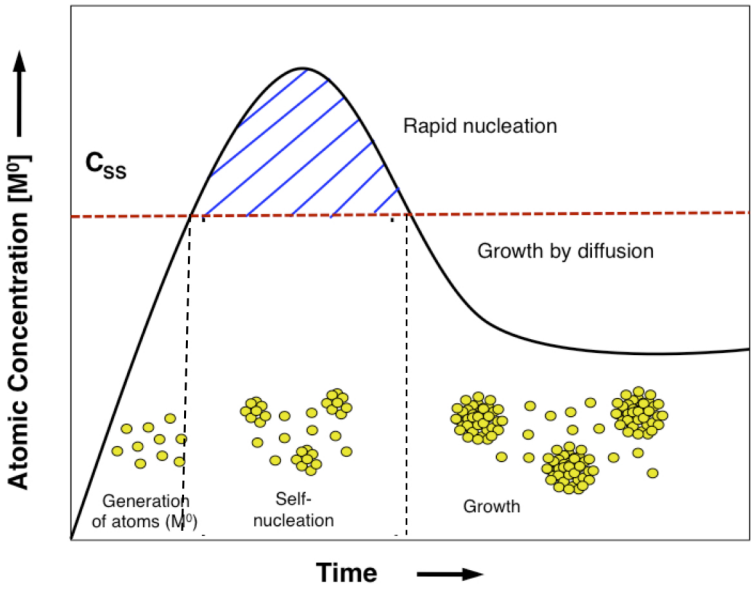

Figure 1.10: Diagram illustrating LaMer and Dinegar's nucleation mechanism.[16]

Initially, the atomic concentration of metallic species increases drastically as the precursor is reduced. Once the atomic concentration reaches a level of supersaturation (C_{SS}), the atoms start aggregating into small clusters through self-nucleation until the atomic concentration decreases to a level below supersaturation. At this point, nucleation stops and no more clusters are formed. The clusters will then continue to grow *via* the consumption of M^0 atoms remaining in solution until forming nanoparticles.

The final nanoparticle size can be controlled by arresting nanoparticle growth using organic molecules as capping agents. In the case of gold nanoparticles -the subject of this thesis- organic molecules that contain S or N are great capping agents due to their affinity for the AuNP's surface.[17, 18]

In 1951, Turkevich *et al.* created a synthetic method to generate AuNPs by reducing gold tetrachloroauric acid ($HAuCl_4$) with citric acid -acting as both, reducing agent and stabilizer- in water. At that point, an in depth study was conducted showing a strong dependence of the gold nanoparticles' shape and size with the ratio between reagents and experimental conditions.[19]

More recently, in 1994, Brust and Schiffrin developed a method for the synthesis of thiol-derivatized gold nanoparticles highly stable in organic solvents, which consisted in growing Au metallic clusters accompanied by the simultaneous attachment of self-assembled thiol monolayers -acting as capping agents- on the growing nuclei by means of a two-phase system. Figure 1.11 shows an overview of the synthetic procedure.

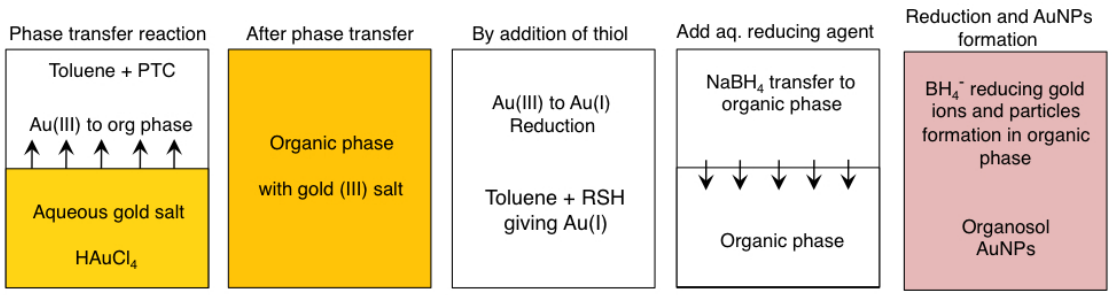

Figure 1.11: Diagram illustrating the synthesis of thiol capped gold nanoparticles by the method of Brust *et al.*[20]. Adapted with permission from [21]. Copyright (2017) American Chemical Society.

The first step of the synthesis involves the dissolution of $HAuCl_4$ -the gold precursor salt- in water followed by phase transfer of Au^{3+} into a toluene organic phase containing tetraoctylammonium bromide (TOAB) which acts as a phase transfer catalyst (PTC). The phase transfer of $AuCl_4^-$ into toluene by TOAB is thought to occur through reaction 1.8, where X represents both Cl^- and Br^- ions.

$$H^+AuCl_4(aq) + (R_8)_4N^+Br^-(org) \rightarrow (R_8)_4N^+AuX_4^-(org) + HX(aq) \qquad (1.8)$$

Upon separation of the organic phase the alkanethiol capping agent (RSH) is added and part of the Au^{3+} cations are reduced to Au^+ facilitating particle synthesis in the bulk of the organic phase, in the presence of alkanethiols or dialkyl disulfide. Then, the addition of an aqueous solution of $NaBH_4$ would be responsible for the reduction of the remainder Au^{3+} and Au^+ present in solution into Au^0 where the nucleation and growth processes will occur an be moderated by the capping agents. A summary of the over all process is presented on Figure 1.12.

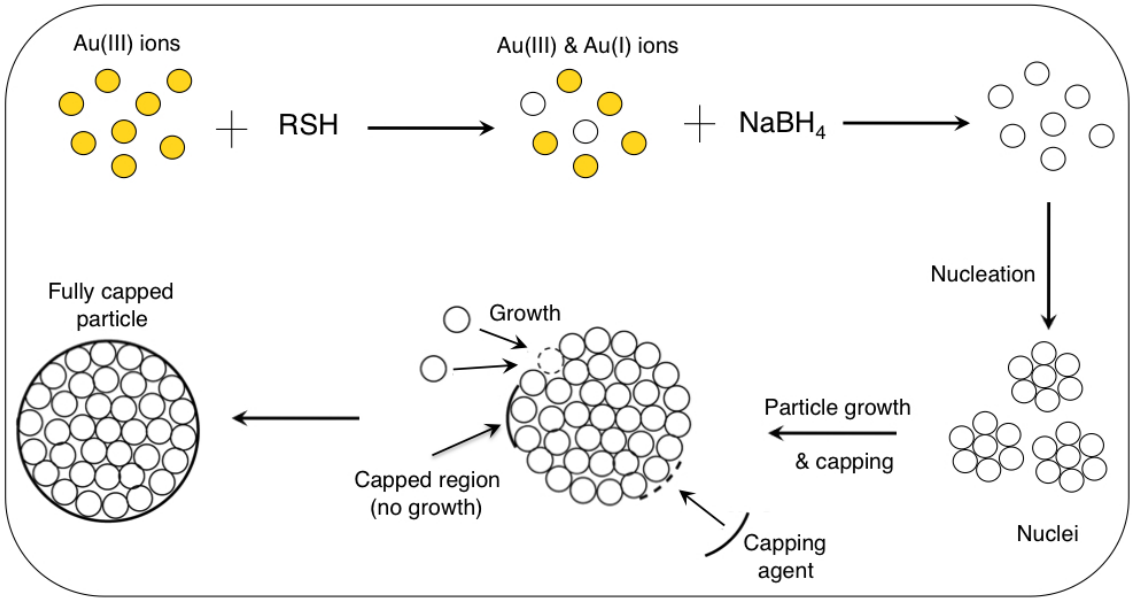

Figure 1.12: Graphical representation of the over all Brust model. Adapted with permission from [21]. Copyright (2017) American Chemical Society.

Photochemical Approach

In spite of the fact that various reliable chemical methods have been developed for the synthesis of metallic nanoparticles [22, 23, 24, 25], using a photochemical approach provides several advantages such as spatial-temporal resolution and a greater synthetic flexibility. By easily tuning the irradiation wavelength, intensity, and time, size and morphology control can be achieved under milder reaction conditions and with significantly less chemical debris left on the surface of the nanoparticles.[26]

One of the most commonly used photochemical methods for the synthesis of gold and silver nanoparticles is based on the use of a Norrish type I reaction as a source of free radical species capable of reducing the metal precursor salt ($HAuCl_4 \cdot 3H_2O$ in the context of this thesis).

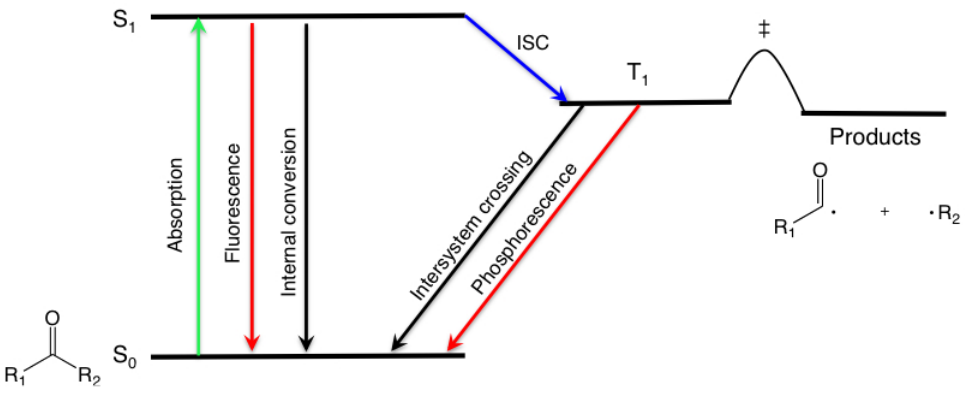

Figure 1.13: Jablonski diagram illustrating the excited states and products of a generic Norrish type I reaction.

In general terms, the Norrish type I reaction (Figure 1.13) involves the α cleavage of ketones and aldehydes upon light irradiation. Initially, the molecule is promoted to its single excited state which then converts into the triplet excited state by intersystem crossing. Since the triplet is longer lived than the singlet excited state -lifetime in the order of μs compared to ns- the molecule will participate in intramolecular reactivity from the triplet excited state generating the corresponding radical products.

Irgacure 2959 (I-2959) is one of the most preferred photochemical nanoparticle precursors. Its absorption coefficient ($\varepsilon_{280\text{nm}} = 1000\ \text{M}^{-1}\text{cm}^{-1}$) and quantum yield of radical formation ($\phi_{\text{Norrish}} = 0.29$) together with the fast generation of reducing radicals[27] makes this molecule very suitable and efficient for the formation of silver and gold nanoparticles *via* Norrish type I reaction. Furthermore, its low toxicity and amphiphilic character provide I-2959 with great versatility in terms of working media.[26] A general depiction of the reactions involved in the formation of AuNPs using I-2959 as a photochemical precursor can be seen on Figure 1.14.

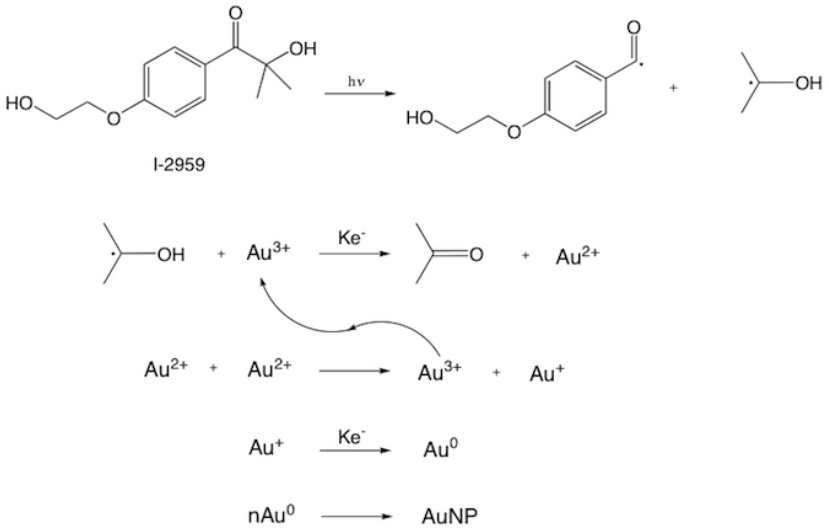

Figure 1.14: General scheme for the photochemical synthesis of AuNPs.[26]

On a first instance, the radical precursor undergoes light promoted unimolecular cleavage through a Norrish type I reaction generating a ketyl radical and 4-hydroxyethoxybenzoyl radical as a precursor for 4-hydroxyethoxybenzoic acid (HEBA). Then, multiple ketyl reductions (Ke^-) of cationic gold species accompanied with the disproportionation of Au^{2+} allow the obtention of metallic gold atoms that will further participate in nucleation and growth to finally form AuNPs. The same method can be used for the successful synthesis of other noble metal nanoparticles such as AgNP.

1.3.2 Synthesis of Gold Nanorods (AuNRs)

The synthesis of gold nanorods can be divided in three main categories, namely, template, electrochemical and seed-mediated methods. These three are presented in chronological order, which implies successive improvement of the obtained rods as well as a decrease in difficulty of the synthetic procedures.

Template Methods

The template approach for synthesizing gold nanorods consists of the electrochemical deposition of gold within the pores of a nanoporous template, followed by the removal of the latter *via* selective dissolution in the presence of stabilizers (see Figure 1.15).[28, 29]

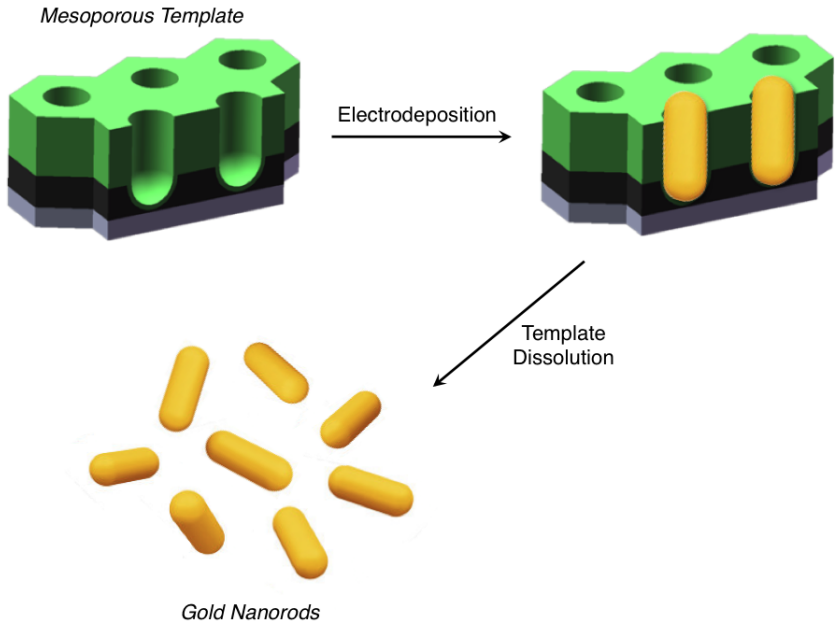

Figure 1.15: General representation of template methods for the synthesis of AuNRs.

The diameter of the synthesized rods coincides with the pore diameter of the template used, meaning that AuNRs diameters can be controlled by either selection or tuning of the template's properties.[30, 31] On the other hand, the length of the AuNRs can be adjusted by regulating the amount of gold deposited within the template's pores.[32]

A fundamental limitation of using this approach is its low yields since only monolayers of rods can be prepared at a time which makes the obtention of higher AuNRs amounts something difficult to achieve and time consuming.

Electrochemical Methods

Higher yields of gold nanorods can be achieved by means of electrochemical methods, in which the synthesis of the AuNRs is performed in a simple electrochemical cell equipped by two electrodes; a platinum metal plate as a cathode and a gold plate as a sacrificial anode (see Figure 1.16). Both electrodes are submerged in an electrolytic solution containing a mixture of a cationic surfactant such as hexadecyltrimethylammonium bromide (C_{16}TAB) and a small amount of a much more hydrophobic cationic co-surfactant, usually tetradodecyltrimethylammonium bromide (C_{12}TAB). The latter acts as a supporting electrolyte and AuNRs stabilizer, while the co-surfactant serves as a rod-shape inducing agent.

Before performing electrolysis, calculated amounts of acetone an cyclohexane are added into the solution. Cyclohexane is used to enhance the formation of elongated rod-like C_{12}TAB micelles while acetone loosens the micellar framework facilitating the incorporation of the shape-inducing co-surfactant.[33]

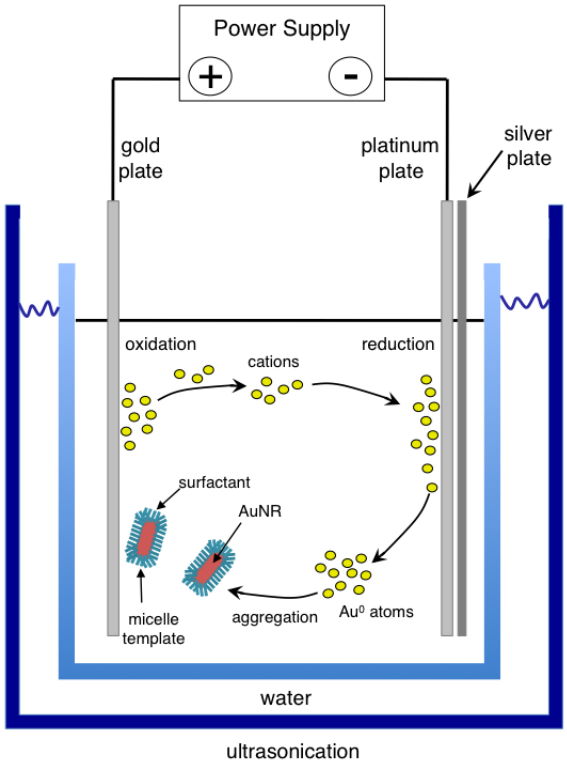

Figure 1.16: General representation of electrochemical method for the synthesis of AuNRs. Adapted with permission from [34]. Copyright 2017, The Electrochemical Society.

During electrolysis, the gold anode is consumed by the formation of $AuBr^-$ anions that will further complex to the cationic surfactants and migrate to the cathode to be reduced. Nanoparticles are most likely to be formed at the interfacial region of the cathodic surface and the electrolytic solution, allowing for further growth of the cylindrical shape.[35]

The presence of a silver plate behind the Pt electrode has shown to be useful to control the aspect ratio of the AuNRs. Furthermore, Wang et al. demonstrated the dependence of the length of the synthesized AuNRs with the concentration and rate of release of silver ions -generated by a redox reaction between the $AuBr^-$ ions and silver metal.[35]

By adjusting electrolysis parameters it is possible to control the aspect ratio of the obtained AuNRs. However, the main drawback of electrochemical methods is the obtention of broad length distributions of gold nanorods limiting their use in size sensitive applications.

Seed-mediated Methods

Even though a large number of methods have been developed for the synthesis of anisotropic nanostructures, the seed-mediated method is the most widely used due to the higher yields and monodispersity that this approach confers.

These methods consist of two steps. The first one is the synthesis of small gold nuclei (typically below 5 nm) -commonly referred as seeds- which serve as the starting point for AuNR growth. The seeds are achieved by the reduction of a gold salt upon the quick addition of a strong reducing agent -usually $NaBH_4$- in excess in order to obtain a quasi-simultaneous production of all the nuclei, homogeneously distributed in the entire solution volume. This will give rise to a monodisperse seed solution, which is key for the obtention of high-quality AuNRs.

The second step of this synthesis is the growth of AuNRs. A growth solution is composed of a surfactant ($C_{16}TAB$) -at a high enough concentrations for it to form rod micelles- which will serve as rod-shaped micellar templates, the gold salt ($HAuCl_4$) a mild reducing agent and small amounts of silver nitrate ($AgNO_3$). See Figure 1.17 for a general representation of this type of methods.

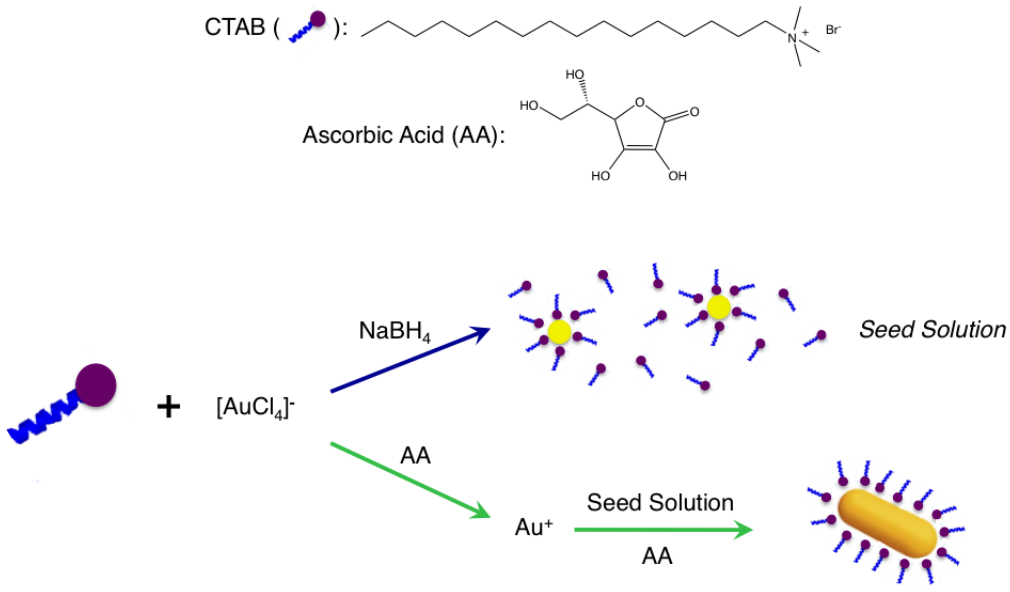

Figure 1.17: General representation of seed-mediated methods for the synthesis of AuNRs. Adapted from [36] with permission of The Royal Society of Chemistry.

Once the growth solution is prepared, the seeds are added as a catalyst for rod formation. The exact mechanism on how the rods are formed has not yet been discovered. However, a general idea of the process has been elucidated.[37]

Tetrachloro auric acid ($HAuCl_4$) is used as a gold precursor, meaning that three different oxidation states are involved in the synthesis of AuNRs: Au^{3+} as a precursor, Au^{+} as an intermediate and Au^{0} in the form of seeds; any Au(II) will disproportionate into Au(III) and Au(I). In the presence of CTAB, the chlorine atoms in $AuCl_4^-$ will be replaced by the bromide ions from the surfactant generating $AuBr_4^-$ ions. In addition, the $AuBr_4^-$ ions will form an ion pair with the surfactant's quaternary ammonium group ($AuBr_4^-$ - CTA). This complexation will produce a shift in the redox potential towards more positive values making the Au^{3+} species easier to be reduced.

The nature of the equilibrium between the three gold species will depend on the relative stability of each of them in the growth solution. Care must be taken under these conditions since Au^{+} (in the form of a complex with CTAB) is the most stable of

the three species, hence, the equilibrium would be conproportionation between Au^{3+} and Au^0 rather than disproportionation meaning that gold seeds could potentially be oxidized by Au^{3+} (See Equation 1.9).[38, 39, 40, 41]

$$Au^{3+} + 2Au^0 \rightleftharpoons 3Au^+ \tag{1.9}$$

Because of this reason, a mild reducing agent is injected after mixing the gold precursor and corresponding surfactant in order to transform Au^{3+} into Au^+ before the seeds are added, avoiding their oxidation as a consequence of comproportionation. Furthermore, the reducing agent used must be weak so as to prevent the direct reduction of Au^{3+} to Au^0 since it will cause secondary undesired nucleation during growth. By these means, the final reduction step ($Au^+ \rightarrow Au^0$) is ensured to happen solely on the surface of the gold seeds, which will act as a catalyst.

Two possible mechanisms have been proposed for the catalysis of the final reduction step by gold seeds. The first one consists of a disproportionation reaction catalysed by the seeds generating Au^{3+} and Au^0, the former being immediately reduced back to Au^+ by remaining reducing agent[42, 43] while the second one consists in the drainage of the electrons of the reducing agent by the Au^0 surface of the seeds and the subsequent in-situ reduction of Au^+.[44, 45] It is worth to remind the reader that any Au(II) will disproportionate into Au(III) and Au(I).

The presence of $AgNO_3$ during synthesis has shown to influence the final aspect ratio of the obtained rods[46], however its role is still unclear. Several hypothesis have arisen, most of them involving the formation of a $Ag[BrCTA]_2$ complex acting as a face specific capping agent on the seeds or by modifying the CTAB micellar structure by silver bromide interactions.[37]

As can be seen, several variables are involved in the seed-mediated synthesis of gold nanorods. However, the three fundamental requirements for their obtention should be noted: (1) a quaternary ammonium surfactant head group capable of forming a complex with the gold salt changing its redox potential, (2) the presence of bromide as a counterion which plays a key role in the symmetry-breaking process [47], and (3) a surfactant -capable of forming cylindrical micelles- with a carbon tail long enough to stabilize the AuNRs but short enough to remain soluble in water close to room temperature.[48]

1.4 Conclusions

The concepts and technical aspects presented in this introductory chapter were widely employed for the nanofabrication of applicable devices focused on drug delivery, catalysis and photo patterning. In this work, the combination between the plasmonic properties of isotropic and anisotropic gold nanostructures -gold nanospheres and gold nanorods- and the remarkable properties of other materials proved to be a powerful strategy for the construction of applicable devices where the photothermal phenomena generated by plasmon excitation through the localized surface plasmon heating effect constituted the mainspring of these systems. This chapter provides the background knowledge that allows a more complete understanding of the mainspring as well as the fundamentals involved in this thesis.

REFERENCES

[1] I Freestone, N Meeks, M Sax, and C Higgitt. The lycurgus cup - A roman nanotechnology. *Gold Bulletin*, 40:270–277, 2007.

[2] M Quinten. *Optical Properties of Nanoparticle Systems: Mie and Beyond*. Wiley-VCH Verlag Co., 2011.

[3] RC Rumpf. Lecture 21 (EM21) – Surface waves, http://emlab.utep.edu, [Accessed: Jan 2017].

[4] JM Pitrake, VM Silkin, EV Chulkov, and PM Echenique. Theory of surface plasmons and surface-plasmon polaritons. *Reports on Progress in Physics*, 70:1–87, 2007.

[5] WL Barnes, A Dereux, and TW Ebbsen. Surface plasmon subwavelength optics. *Nature*, 424:824–830, 2003.

[6] KA Willets and RP Van Duyne. Localized surface plasmon resonance spectroscopy and sensing. *Annual Review of Physical Chemistry*, 58:267–297, 2007.

[7] J Pérez-Juste, B Rodríguez-González, and LM Liz-Marzán. Optical control and patterning of gold nanorod-poly(vinyl alcohol) nanocomposite films. *Advanced Functional Materials*, 15:1065–1071, 2005.

[8] S Link, ZL Wang, and MA El-Sayed. Alloy formation of gold-silver nanoparticles

and the dependence of the plasmon absorption on their composition. *Journal of Physical Chemistry*, 103:3529–3533, 1999.

[9] L Stryer. Fluorescence energy transfer as a spectroscopic ruler. *Annual Review of Biochemistry*, 47(1):819–846, 1978.

[10] JC Scaiano and K Stamplecoskie. Can surface plasmon fields provide a new way to photosensitize organic photoreactions? from designer nanoparticles to custom applications. *Journal of Physical Chemistry Letters*, 4:1177–1187, 2013.

[11] JM Petroski, ZL Wang, TC Green, and MA El-Sayed. Kinetically controlled growth and shape formation mechanism of platinum nanoparticles. *Journal of Physical Chemistry*, 102:3316–3320, 1998.

[12] YY Yu, SS Chang, CL Lee, and CRC Wang. Gold nanorods: Electrochemical synthesis and optical properties. *Journal of Physical Chemistry*, 101:6661–6664, 1997.

[13] R Jin, Y Cao, CA Mirkin, KL Kelly, GC Schatz, and GC Zheng. Gold nanorods: Electrochemical synthesis and optical properties. *Science*, 294:1901–1903, 2001.

[14] KG Stamplecoskie, GL Hallet-Tapley, and JC Scaiano. Photochemical Norrish type I reaction as a tool for metal nanoparticle synthesis: Importance of proton coupled electron transfer. *Chemical Communications*, 48:4798–4808, 2012.

[15] VK LaMer and RH Dinegar. Theory, production and mechanism of formation of monodispersed hydrosols. *Journal of the American Chemical Society*, 72:4847–4854, 1955.

[16] J.A. Moma, T.A. Ntho, and M Scurrell. *Catalytic Application of Nano-Gold Catalysts*. InTech, DOI: 10.5772/64103. Available from:

http://www.intechopen.com/books/catalytic-application-of-nano-gold-catalysts/gold-catalysed-reactions., 2016.

[17] VJ Gandubert and RB Lennox. Assessment of 4-(dimethylamino)pyridine as a capping agent for gold nanoparticles. *Langmuir*, 21:6532–6539, 2005.

[18] F Mirkhalaf, J Paprotny, and DJ Schiffrin. Synthesis of metal nanoparticles stabilized by metal-carbon bonds. *Journal of the American Chemical Society*, 128:7400–7401, 2006.

[19] J Turkevich, PC Stevenson, and J Hillier. A study of the nucleation and growth processes in the synthesis of colloidal gold. *Discussions of the Faraday Society*, 11:55–75, 1951.

[20] M Brust, M Walker, D Bethell, DJ Schiffrin, and R Whyman. Synthesis of thiol-derivatised gold nanoparticles in a two-phase liquid-liquid system. *Journal of the Chemical Society, Chemical Communications*, 0:801–802, 1994.

[21] SRK Perala and S Kumar. On the mechanism of metal nanoparticle synthesis in the Brust-Schiffrin method. *Langmuir*, 29:9863–9873, 2013.

[22] G Schmid and B Corain. Nanoparticulated gold: Syntheses, structures, electronics and reactivities. *European Journal of Inorganic Chemistry*, pages 3081–3098, 2003.

[23] T Yonezawa and T Kunitake. Practical preparation of anionic mercapto ligand-stabilized gold nanoparticles and their immobilization. *Colloids and Surfaces A: Physicochemical and Engineering Aspects*, 149:193–199, 1999.

[24] CA Waters, AJ Mills, KA Johnson, and DJ Schiffrin. Purification of dode-

canethiol derivatized gold nanoparticles. *Chemical Communications*, pages 540–541, 2003.

[25] MC Daniel and D Astruc. Gold nanoparticles: assembly, supramolecular chemistry, quantum-size related properties and applications towards biology, catalysis and nanotechnology. *Chemical Reviews*, 104:293–346, 2004.

[26] JC Scaiano, KG Stamplecoskie, KL McGilvray, and NL Pacioni. *A Paradigm for the Radical-Mediated Photochemical Synthesis of Metal Nanostructures. Encyclopedia of Radicals in Chemistry, Biology and Materials.* John Wiley Sons, Ltd, 2012.

[27] S Jockusch, MS Landis, B Freiermuth, and NJ Turro. Photochemistry and photophysics of α-hydroxyketones. *Macromolecules*, 34:1619–1626, 2001.

[28] BMI Van der Zande, MR Boehmer, LGJ Fokkink, and C Schoenenberger. Aqueous gold sols of rod-shaped particles. *Journal of Physical Chemistry B*, 101:852–854, 1997.

[29] VM Cepak and CR Martin. Preparation and stability of template-synthesized metal nanorods sols in organic solvents. *Journal of Physical Chemistry B*, 102:9985–9990, 1998.

[30] KB Jirage, JC Hulteen, and CR Martin. Nanotube-based molecular filtration membranes. *Science*, 278:655–658, 1997.

[31] JC Hulteen and CR Martin. A general template-based method for the preparation of nanomaterials. *Journal of Materials Chemistry*, 7:1075–1087, 1997.

[32] BMI Van der Zande, MR Boehmer, LGH Fokkink, and C Schoenenberger. Col-

loidal dispersions of gold rods: synthesis and optical properties. *Langmuir*, 16:451–458, 2000.

[33] M Tornblom and U Henriksson. Effect of solubilization of aliphatic hydrocarbons on size and shape of rod-like CTABr micelles studied by ^{2}H NMR relaxation. *Journal of Physical Chemistry B*, 101:6028–6035, 1997.

[34] C Huang, P Chiu, Y Wang, WR Chen, and TH Meen. Synthesis of the gold nanocubes by electrochemical technique. *Journal of the Electrochemical Society*, 153:D129–D133; doi:10.1149/1.2203931, 2006.

[35] SS Chang, CW Shih, CD Chen, WC Lai, and CRC Wang. The shape transition of gold nanorods. *Langmuir*, 15:701–709, 1999.

[36] H Chen, L Shao, Q Lia, and J Wang. Gold nanorods and their plasmonic properties. *Chemical Society Reviews*, 42:2679–2724, 2013.

[37] L Scarabelli and LM Liz-Marzán. A "Tips and tricks" practical guide to the synthesis of gold nanorods. *The Journal of Physical Chemistry Letters*, 6:4270–4279, 2015.

[38] J Rodríguez-Fernández, J Pérez-Juste, P Mulvaney, and LM Liz-Marzán. Spatially-directed oxidation of gold nanoparticles by Au(III)-CTAB complexes. *Journal of Physical Chemistry B*, 109:14257–14261, 2005.

[39] E Carbó-Argibay, B Rodríguez-González, I Pastoriza-Santos, J Pérez-Juste, and LM Liz-Marzán. Growth of pentatwinned gold nanorods into truncated decahedra. *Nanoscale*, 2:2377–2382, 2010.

[40] E Carbó-Argibay, B Rodríguez-González J Pacífico, I Pastoriza-Santos, J Pérez-

Juste, and LM Liz-Marzán. Sharpening of gold nanorods: The rod-to-octahedron transition. *Angewandte Chemie International Edition*, 46:8983–8987, 2007.

[41] L Scarabelli, M Grzelczak, and LM Liz-Marzán. Tuning gold nanorod synthesis through pre-reduction with salicylic acid. *Chemistry of Materials*, 25:4232–4238, 2013.

[42] G Bergamini, P Ceroni, V Balzani, M Gingras, JM Raimundo, V Morandic, and PG Merrlic. Synthesis of small nanoparticles: Au(I) dispropotrionation catalyzed by a persulfurated coronene dendrimer. *Chemical Communications*, pages 4167–4169, 2007.

[43] M Harada and S Kizaki. Formation mechanism of gold nanoparticles synthesized by photoreduction in aqueous ethanol solutions of polymers using in-situ quick scanning, X-ray absorption, fine structure and small-angle X-ray scattering. *Crystal Growth Research*, 16:1210–1212, 2016.

[44] J Pérez-Juste, LM Liz-Marzán, S Carnie, DYC Chan, and P Mulvaney. Electric-field-directed growth of gold nanorods in aqueous surfactant solutions. *Advanced Functional Materials*, 14:571–579, 2004.

[45] J Rodríguez-Fernández, J Pérez-Juste, and FJ García de Abajo. Seeded growth of submicron Au colloids with quadrupole plasmon resonance modes. *Langmuir*, 22:7007–7010, 2006.

[46] JG Hinman, AJ Stork, JA Varnell, AA Gewirth, and CJ Murphy. Seed mediated growth of gold nanorods: towards nanorod matryoshkas. *Faraday Discussions*, 191:9–33, 2016.

[47] S Si, C Leduc, MH Delville, and B Lounis. Short gold nanorod growth revisited:

The critical role of the bromide counterion. *Chem. Phys. Chem.*, 13:193–202, 2012.

[48] N Almora-Barrios, G Novell-Leruth, P Whiting, LM Liz-Marzán, and N López. Theoretical description of the role of halides, silver, and surfactants on the structure of gold nanorods. *Nano Letters*, 14:871–875, 2014.

Chapter 2

Plasmon Excitation of Supported Gold Nanoparticles can Control Molecular Release from Supramolecular Systems

2.1 Silica Based Mesoporous Materials

2.1.1 Some History and a General Description

The history of silica based porous materials goes back to 1756 when zeolites -a broad family of aluminosilicate materials- were first described by the Swedish scientist Axel F. Cronstedt. However, it was not until the nineteenth century that the properties of these materials began to be documented yet their potential applications remained to be undiscovered. In 1931, James W. McBain proposed the term "molecular sieve" to describe a class of materials that exhibited selective adsorption properties that made them capable of separating molecular components of a mixture based on their shape and size differences.[1, 2] The incorporation of the "molecular sieve" concept can be hailed as a milestone in the development of porous materials as we know them today being regarded as the starting connection between the properties of silica based porous materials and their countless applications. Ever since then, there has been a continually growing interest in expanding applications, synthetical routes and pore sizes of silica based porous materials from the micropore to the macropore regions. According to the nomenclature of the International Union of Pure and Applied Chemistry (IUPAC) porous materials can be classifed into three categories based on their corresponding pore diameter. Namely, microporous (< 2 nm) , macroporous (> 50 nm) and mesoporous materials whose pore diameter ranges from 2 nm to 50 nm.

In 1992, scientist from Mobil Company developed the M41S series of mesoporous materials (2 nm - 50 nm) which have an exceptionally large uniform pore structure being MCM-41 the one that has been most extensively studied. The development of the M41S series can be considered the resurgence of the porous materials and the beginning of the mesoporous worldwide research.

Figure 2.1 accounts for the rapid development of mesoporous structures in science since 1992 describing a substanctial increase in number of publications related to mesoporous materials.

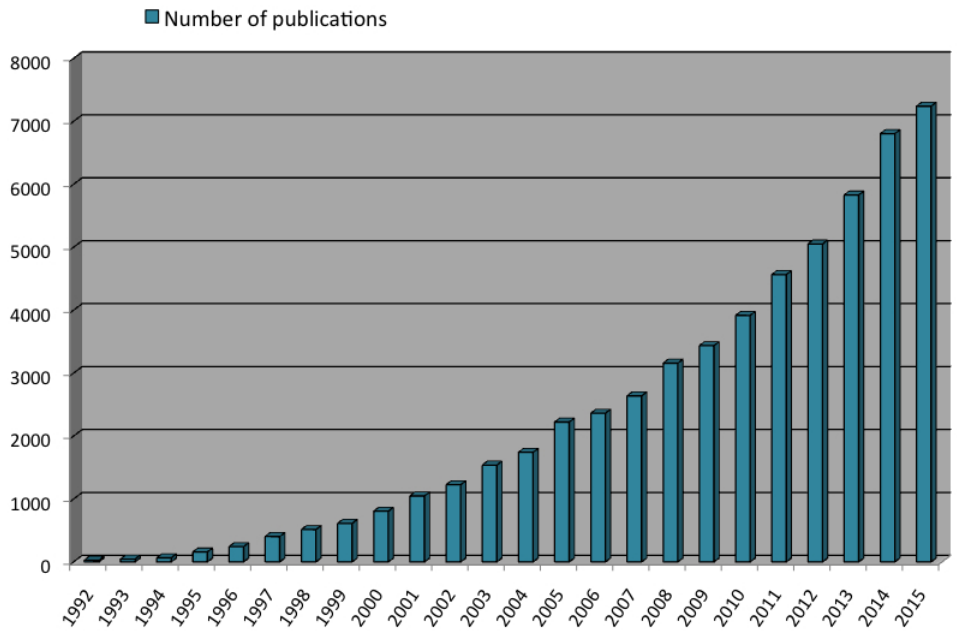

Figure 2.1: Number of published papers originated from the SCI system using "mesoporous" as a subject since 1992.

Silica based mesoporous materials are highly ordered and size-controlled materials with adsorption properties selective to guest size allowing for the encapsulation of small molecules while excluding larger ones. Moreover, they possess extremely high surface areas, large pore volumes and narrow pore distributions conferring the materials with high adsorption capacities. Further, mesoporous materials have high thermal and chemical stability as well as flexibility for further surface functionalization permitting the incorporation of hydrophobic, hydrophilic, polar as well as charged functional moieties.[3, 4, 5, 6] Surface functionalization with organic or inorganic groups confers these materials new physical and chemical properties making them suitable for a broad variety of applications such as adsorption, separation, catalysis, sensing and

drug delivery, among others.[7, 8, 9, 10]

2.1.2 Mechanism of Formation of Silica Mesoporous Materials

Sol-gel chemistry has been extensively investigated and ultimately used to synthesize mesoporous silica materials. This process consists of transforming a colloidal dispersion of small particles suspended in a liquid (sol) into a rigid non-fluid mass composed of a continuous solid network and a continuous liquid phase (gel).[11, 12] In the synthesis of mesoporous silica materials, sol-gel methods will transform silicon alkoxides such as tetraehthyl orthosilicate (TEOS) into an inorganic network by means of hydrolysis followed by condensation aided by either a basic or an acid catalyst.[13]

Reactions Involved

Figure 2.2a shows the base catalysed hydrolysis of silicon alkoxides *via* bimolecular nucleophilic substitution (SN_2) which involves a nucleophilic attack performed by the hydroxide anion to the silicon centre of the tetraalkoxysilane resulting in a penta-coordinate transition state in which the silicon atom is partially bonded to both the hydroxyl group and departing alkoxide group. All three, the attacking molecule (OH^-), silicon centre and departing alkoxide group are positioned on the same axis in a perpendicular fashion to the other three alkoxide groups. The alkoxide leaving group is then pushed off leading to the formation of silanol and an alkoxide ion as products.

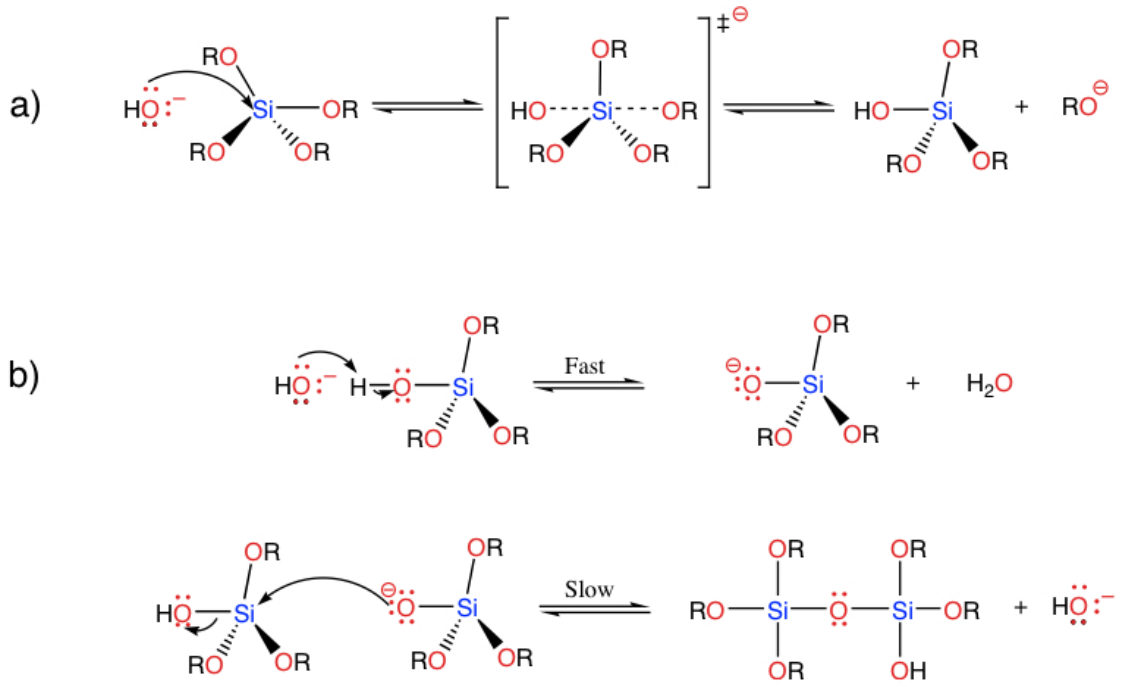

Figure 2.2: Mechanisms of based catalyzed hydrolysis of alkoxides (a) and alcohol condensation (b) during the sol-gel process.

Abstraction of a silanol proton by a hydroxide ion constitutes the first step of the condensation reaction (See Figure 2.2b) yielding a siloxide ion and water. The former will then attack the silicon centre of another silanol molecule through an SN_2 reaction in which the hydroxide catalyst is regenerated and a siloxane bridge is formed.[14]

The acid catalyzed hydrolysis and condensation of silicon alkoxides also involves bimolecular nucleophilic substitution reactions. As shown in Figure 2.3a, the first step of hydrolysis consists in the protonation of one of the alkoxide groups of the tetraalkoxysilane generating a positively charged alkoxide which is also a good leaving group. Then, a water molecule reacts *via* SN_2 reaction by attacking the silicon centre forming a silanol, the corresponding alcohol and an acidic proton. Subsequently, a condensation reaction occurs (Figure 2.3b) in which the hydroxyl group of the silanol becomes protonated followed by the attack of another silanol molecule pushing the water off as a leaving group while forming the corresponding siloxane bridge.

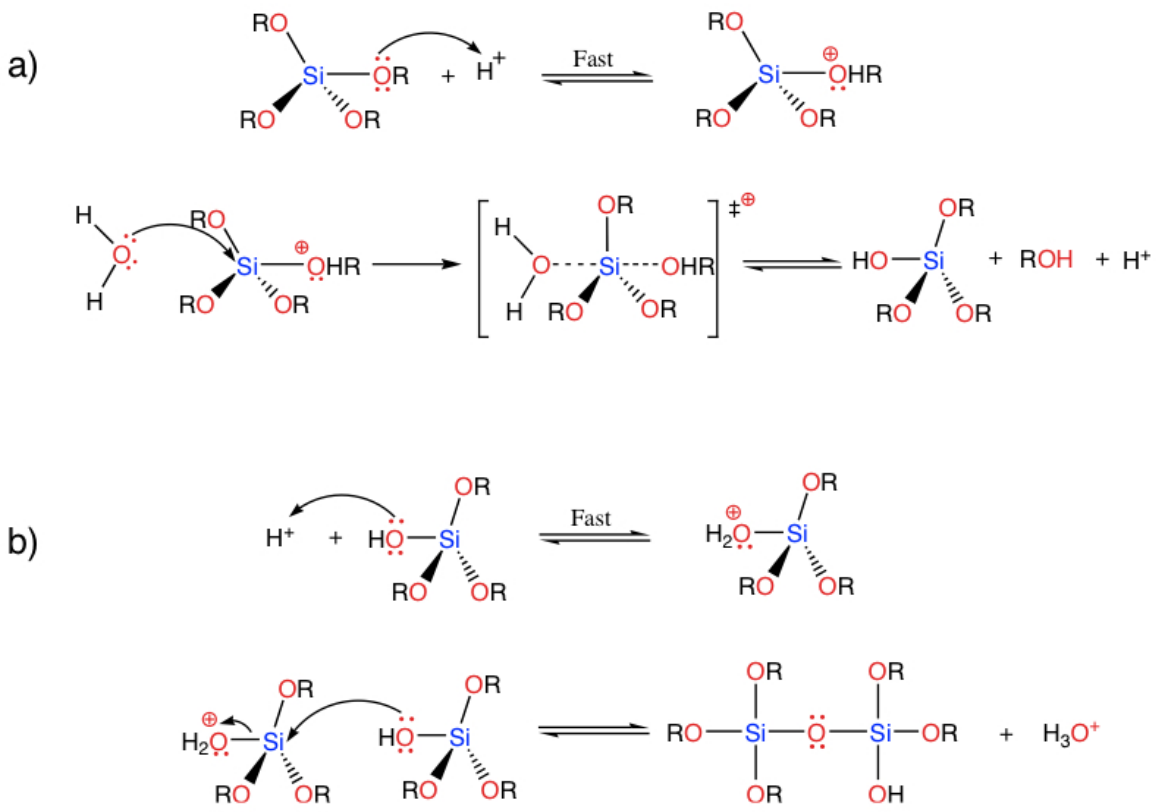

Figure 2.3: Mechanisms of acid catalyzed hydrolysis of alkoxides (a) and alcohol condensation (b) during the sol-gel process.

Sol-Gel Dynamics

The properties of mesoporous silicate materials are achieved by the formation of organized pore systems directed by assemblies of molecules and solution energetics rather than involving individual directing agents during synthesis. The synthetical strategy is based on the use of ionic surfactants as supramolecular aggregate directing agents (SDAs) which are fundamental in the formation of mesoporous silica based materials since it is the self assembly of surfactant micelles that allows for the specific control of the final structure and pore sizes by varying synthesis conditions.[15, 16]

Two mechanisms for the formation of mesoporous materials were proposed by Mobil Company.[17, 18] The first mechanism was based on a "liquid crystal templating" model and proposed that the surfactant molecules form a lyotropic liquid-crystalline phase in the absence of silica precursors. On a first instance, the surfactant molecules associate to form individual micelles and then these aggregate into more complex rod-like micelles. The rods would then assemble into hexagonal liquid crystals that will serve as templates for the growth of the silicate species *via* hydrolysis and condensation around the surfactant rods (as shown in Figure 2.4a).

The liquid crystal templating mechanism initially proposed caused great controversy due to the fact that for hydrothermal type syntheses the concentration of surfactants required is too low for the formation of such a liquid crystalline phase to be feasible. Hence, a second mechanism was proposed by scientists from Mobil Company which maintained the premise of a liquid crystal phase formation. However, the above mentioned lyotropic phase would be formed at lower surfactant concentrations by the cooperative self-assembly of the directing agents promoted by the early presence of the silica precursor molecules (Figure 2.4b) meaning that both components would play a crucial role in the assembly.

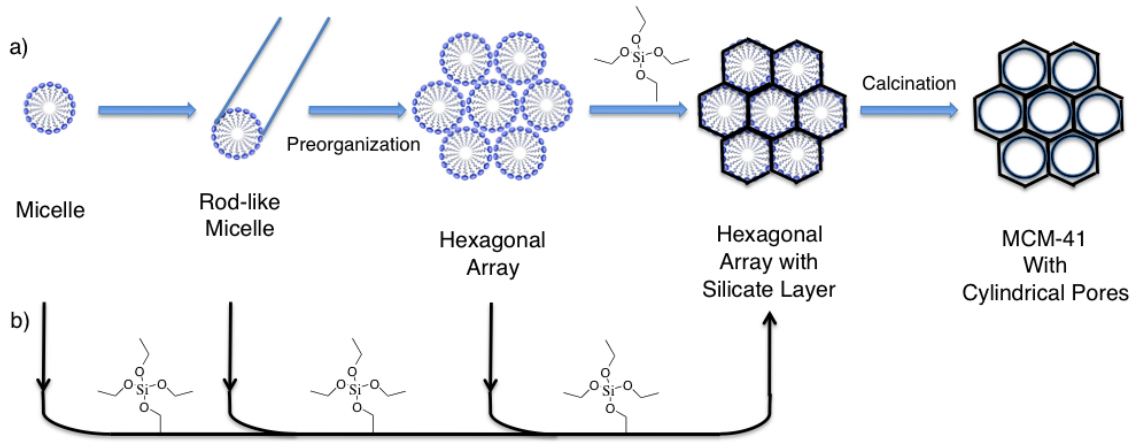

Figure 2.4: Liquid crystal templating mechanism of formation of mesoporous materials involving late addition of the silicate source (a) and Modified liquid templating mechanism of formation of mesoporous materials involving early addition of the silicate source (b).

Initially, the surfactant molecules would interact with the silicate source species forming organic-inorganic micelles which further aggregate to form more complex rod-like micelles. Then, the silicate-surfactant rods would associate into hexagonal liquid crystals and subsequently hexagonal mesostructures (mesophase) while the silicates continue to condense. The nature of the surfactant-silicate source interactions that will finally drive the formation of the mesophases depends on their corresponding charges. In the case of MCM-41, the positive triethylammonium group of the surfactant used (C_{16}TAB) will interact with the negative silanoxide species by Coulombic attractions.[14]

The final step for obtaining the ordered mesoporous material -once the gel has been formed- is the removal of the surfactant by calcination which will remove the surfactant leaving the silica network with its corresponding unoccupied ordered pores.

2.1.3 Mesoporous Functionalization

Functionalization of silica mesoporous materials in order to tune physical and chemical properties is possible by incorporating organic or inorganic components either on the surface of the pores or directly in the walls of the material. Two main functionalization approaches have been developed, namely co-condensation and grafting.[19, 20] The former consists in including organoalkoxysilane precursors during synthesis so the framework will be formed by the condensation of both the original silica source and the organoalkoxysilane species. On the other hand, the grafting process consists of the post-synthesis addition of the organoalkoxysilanes on the pore surface of the pre-fabricated framework. By modifying the pore surface it is possible to confer the materials with tethers containing the exposed desired functional groups that will help tuning properties such as hydrophobicity, hydrophilicity and acid/base.

Grafting processes are widely used to functionalize silica solids because they preserve the porosity order in the material structure which leads to an enhancement of diffusion properties.[21] Figure 2.5a shows an example of a mesoporous network before grafting in which free hydroxyl groups are present while Figure 2.5b shows the amino functionalized mesopores obtained upon a condensation reaction between the hydroxyl group of the pre-fabricated material and amine containing organoalkoxysilane molecules. This represents the approach used in this chapter in order to modify the pores of MCM-41 with aminopropyl moieties through a condensation reaction (Figure 2.6).

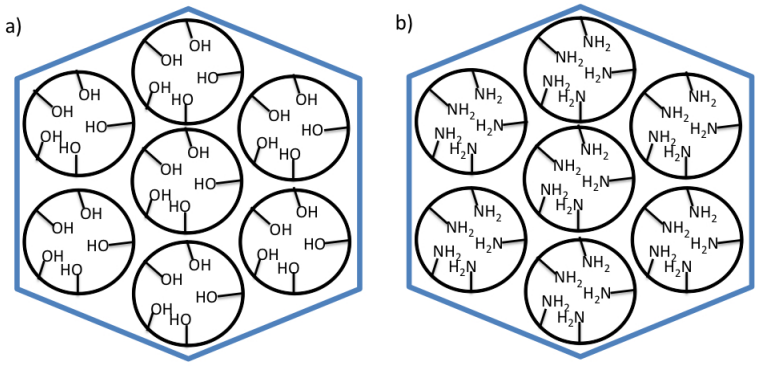

Figure 2.5: Mesoporous network cross-section before (a) and after (b) grafting of aminoalkylsilane moieties.

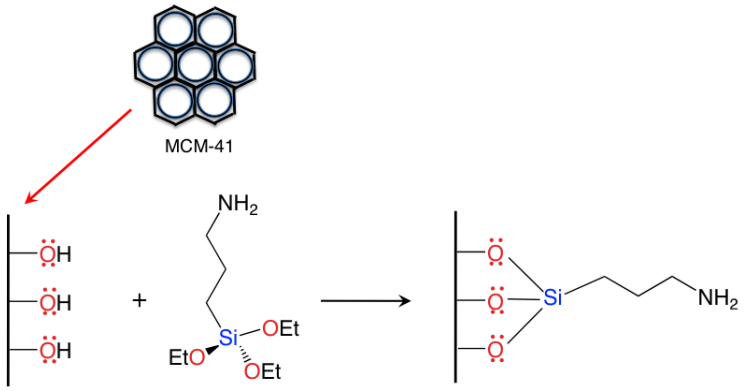

Figure 2.6: General condensation reaction of APTES on the surface of MCM-41.

2.1.4 Mesoporous Materials in Drug Delivery

The rapid development of technology, biomedical materials and new active molecules oriented towards human health is astonishing. Recent progress in the design of surface-functionalized mesoporous silica materials have revealed the potential of these solids as molecular delivery systems,[22, 23, 24, 25, 26] also referred to as cargo-controlled release systems.[27]

The drug delivery system used to administer a cargo molecule plays a vital role in the pharmacological effect of the drug being delivered influencing the rate of release, the site and duration of the drug action concomitantly ensuring the availability of the

active drug at the site for the appropriate length of time.[28]

In 2001 Vallet-Regi et al. proposed the use of MCM-41 as implantable systems.[26] Since then, researchers have focused on the design of more efficient mesoporous materials to be used in drug delivery processes. MCM-41 is one of the most extensively studied mesoporous materials due to its unique hexagonal, uniform, and highly ordered pore structure.[29] The facile synthesis of MCM-41 makes it a reproducible and readily accessible material. Besides its biocompatibility and highly ordered pore distribution, this material has free hydroxyl groups, enabling ready functionalization with dyes, drugs, and other molecules.[30]

In conjunction with the efforts for improving mesoporous silica based drug-delivery systems, special interest has been put into controlling either the release of cargo molecules or the start of the release process. However, most of the drug delivery systems using mesoporous materials focus solely on one of those two objectives generating a lack of systems in which both features are controlled at the same time.

Rate Control

The basic mechanism of release from mesoporous materials is mainly governed by the diffusion of the adsorbed molecules through the mesopores in the silica matrix. The main strategy for achieving rate control is varying the pore size and morphology of the materials with the aim of altering the diffusion of the drug to the exterior[31]; smaller and/or less organized pores give rise to smaller rates of release. A classic example is the one presented by Lin *et al.* where silica-based mesoporous materials of different morphology -hexagonal, helical and worm-like porosity- where used to tune the rate of delivery of antibacterial room-temperature ionic liquids.[22]

Another approach involves the functionalization of the pore walls with agents that will decrease the diffusion of the drug to the exterior, i.e. by decorating the

pore outlets with alkylsilanes chains of different length and using them as diffusion controllers; longer alkyl chains lead to a slower releasing rate allowing mass transport to be regulated artificially.[32]

In spite of these strategies being simple and straight forward, they carry certain drawbacks such as the fact of needing a different material for each rate of release and the associated impossibility of obtaining several rates during the same delivery process, which limits the usefulness of this devices in systems that would benefit of more complex release profiles.

Start Control

More sophisticated systems have been developed in order to control the start of the cargo release and modulate the delivery with the use of external stimuli. Several gated systems have been proposed in which external stimuli such as pH or light can be used to open the gates and induce cargo release.

Most of the gate systems involve the use of agents that block the pore openings. Common examples of the use of pore blocking agents are the use of CdS nanoparticles attached to the mesoporous material through chemically cleavable disulfide bonds that will then be broken through chemical stimulation by using dithiothreitol, removing the nanoparticle caps and letting the host to diffuse out in solution.[33] Another example is based on the use of 4-mercaptophenylboronic acid capped AuNPs as pore blocking agents. The hydrolysis of the boroester bonds at an acidic pH detaches the AuNPs from the surface letting the cargo to diffuse out.[34]

The advantage of materials that can be remotely activated by light relies in the possibility of replacing conventional photocages where release is based on chemical transformations, such as bond cleavage.[35, 36] Such is the case of the work presented by Vivero *et al.* where AuNPs functionalized with a photoliable sulfur linker blocked

the pore openings of MCM-41. Upon UV irradiation, the photoliable linker is cleaved changing the zeta potential of the surface of AuNPs from negative to positive. The change in zeta potential produces the charge repulsion between the AuNPs and MCM-41 uncapping the mesopores and allowing the release of guest molecules.[25]

Some systems in which visible light and the activation of the localized surface plasmon have been used for gate opening also described in Chapter 3. However -as mentioned in the previous section- the state of the art in drug delivery lacks the development of systems in which both the start and rates of release are controlled at the same time and, furthermore, with the same stimuli.

It is worth reminding the reader that the ultimate purpose of controlling the drug delivery is to achieve more effective therapies while eliminating the potential of both under and overdosing. Nevertheless, controlling the delivery of a drug implies several other advantages that mesoporous materials can also confer[37]:

- minimization of drug degradation and loss
- prevention of harmful side-effects
- modulation of drug bioavailability
- improved efficacy
- reduced toxicity
- delivery of the drug at a specific site

2.1.5 Toxicity of Gold Nanostructures: State of the Art

Great controversy exists in terms of the toxicity of gold nanostructures. While a vast variety of *in vitro* and *in vivo* methods have been implemented to assess their toxicity[38, 39] -such as proliferation, necrosis, apoptosis and DNA damage assays- the conclusions achieved have been extremely varying and contradictory, in many cases, possibly due to the lack of particle characterization after incorporation, forgetting to account for post-incorporation modifications like changes in aggregation or surface changes which would influence the final toxicity of these nanostructures. Moreover, many studies focus on determining the lethal dosage of gold nanoparticles but none of them evaluate an effective therapeutic dosage in order to obtain the minimum concentration of these nanostructures at which the therapeutic response is produced.

On the other hand, most of the studies are conducted on either citrate or CTAB capped AuNPs suggesting the necessity for studying pharmacokinetics and toxicity of the selectively functionalized gold nanostructures to obtain a real depiction of the effect of the nanoparticles that are actually being used. Finally, comprehensive studies on the effect of various administration techniques would be of extreme usefulness.

In spite of the contradictory results and missing aspects in this matter, the great amount of information regarding uptake and cytotoxicity is extremely useful proving that it is in fact possible to control these parameters contributing -at the same time- with a staggering number of techniques developed which are capable of decreasing negative side effects, *i.e.*. coating of gold nanostructures with bio-compatible materials. A comprehensive review related to this findings was reported by Murphy *et al.*[40]

2.1.6 About This Chapter

In this chapter, a set of simple hybrid mesoporous materials were designed based on the combination of the properties of gold nanoparticles (AuNPs) -described in Chapter 1- and those of mesoporous materials. By using the surface plasmon band transition of AuNPs a controlled release and the applicability of these hybrid materials in drug or molecular delivery systems were tested using naproxen as guest molecule. In our systems, light-induced cargo release is the result of changes in the dynamics of diffusion resulting from plasmonic heating within mesoporous channels shared by AuNPs and naproxen. Naproxen is a nonsteroidal anti-inflammatory drug used to treat symptoms related to different conditions such as migraine, kidney stones and gouty arthritis.[41]

Two different approaches were used to synthesize the hybrid materials. The first one consists of the anchoring of AuNPs to the mesoporous material by the use of 3-aminopropyltriethoxisilane (APTES) as a linker that has been previously grafted within MCM-41. In simple words, MCM-41 was synthesized and further functionalized with APTES followed by a one pot photochemical incorporation of AuNPs into the solids based on a synthesis developed by McGilvray *et.al*, previously described in Chapter 1. The second approach differs from the first one due to the absence of a linker that anchors the AuNPs to the walls of MCM-41. AuNPs were incorporated into the same silica materials by direct adsorption-deposition during their photochemical synthesis.

A key advantage of the systems reported in this chapter is the possibility to exploit the surface plasmon resonance band of AuNPs to control the rate of the release of a drug by altering the diffusion of the cargo while avoiding the need of elaborated complex synthetic procedures and the use of UV light. This last feature expands the applicability to biological samples in which damage would be incurred by the use of

UV light.

2.2 Experimental

2.2.1 Reagents

Tetraethylorthosilicate (TEOS, 98%), cetyltrimethylammonium bromide (C_{16}TAB, 96%), aqueous ammonia solution (NH_4OH, 30%), tetrachloroauric acid trihydrate ($HAuCl_4 \cdot 3H_2O$), 3-aminopropyltriethoxysilane (APTES) and naproxen were purchased from Sigma-Aldrich and used as received. Irgacure-2959 was obtained from Basf Chemicals Company.

2.2.2 Instrumentation

X-ray Diffraction Studies (XRD)

Small-angle powder X-ray diffraction (XRD) analysis was carried out using a Rigaku Ultima IV difractometer Cu Kα radiation (k = 1.541836), operating at 40 kV and 30 mA, at a scanning velocity of 0.03° min^{-1} in the $0.7° < 2\theta < 10°$ range.

Transmission Electron Microscopy (TEM)

The morphology of the mesoporous materials was characterized by transmission electron microscopy (TEM). TEM analyses were carried out on a JEM-2010F microscope (JEOL, 200 kV, 0.14 nm resolution). For this purpose, samples were prepared by dipping a sonicated suspension of the material in ethanol on a carbon-coated copper grid. The digital analysis of the TEM micrographs was done using DigitalMicrographTM 3.6.1 by Gatan.

Adsorption Isotherms

Textural properties of the solids were determined by N_2 adsorption at 77 K in an AUTOSORB-6 apparatus. Samples were previously degassed for at 373 K at 5 x 10^{-5} bar. The adsorption branch of the obtained isotherms was used to determine the pore size distribution using the Barret-Joyner-Halenda (BJH) method. The surface area was calculated using the multipoint BET method at a 0.05-0.3 relative pressure range. Mesopore volume was measured at the plateau of the adsorption branch of the nitrogen isotherm, P/P_0 is mainly due to interparticle condensation.

Inductively Coupled Plasma Optical Emission Spectroscopy (ICP-AES)

Metal loading in the materials was determined by ICP-AES on a Perkin Elmer Analyst 300 absorption apparatus and plasma ICP Perkin-Elmer 40. An amount of 25 mg of every sample was digested in 1 mL HF during 12 h prior to analysis.

UV-visible Spectroscopy

Diffuse reflectance UV-Visible data of pressed powders were recorded on a Cary 100 UV-visible spectrophotometer equipped with a Har-153 rick praying mantis accessory, in a wavelength range from 200 to 600 nm, and recalculated following the Kubelka-Munk function.[42]

Nuclear Magnetic Resonance Spectroscopy (NMR)

NMR analyses were carried on a Bruker AVANCE II 400 MHz NMR spectrometer.

Thermogravimetric Analysis (TGA)

APTES and Naproxen loadings were determined by thermogravimetric analysis using a Q5000 TA instrument equipped with QSeries operating software.

2.2.3 Synthesis of Hybrid Materials by Grafting Approach

A reported synthesis of MCM-41 type silica [21] was followed to pre-fabricate the mesoporous silica materials for the grafting incorporation of APTES on their structure. In a typical synthesis, 4.4 g of C_{16}TAB was dissolved in a solution of 19.2 mL of ammonium hydroxide in 400 mL of distilled water. Then, 23.3 mL of TEOS was added and the mixture was stirred until hydrolysis was complete. The molar composition of the synthesized gel was 1 SiO_2/0.2 C_{16}TAB/1.41 NH_4OH/280 H_2O.

After hydrolysis was concluded, the solution was transferred to a 100 mL Teflon lined stainless steel autoclave and heated at 80°C for 24h. Upon cooling to room temperature, the solid product was washed with water and ethanol, filtered out, and air-dried overnight at 60°C. Finally, the surfactant was removed by calcination at 550°C for 8h (2°C min^{-1}) under static air atmosphere.

The grafting of 3-aminopropyltriethoxysilane onto MCM-41 was carried out as follows: 1 g of MCM-41 was kept at 200°C for 2h in order to regenerate an adequate amount of hydroxyl groups on its surface. Then, a solution of 50 mL of toluene and 466 μL APTES was added to the activated material and refluxed for 12h. Finally, the hot solution was filtered out and the solid sample was washed with fresh toluene and air-dried at 60°C, leading to the MCM-APTES (Map) solid.

Incorporation of AuNPs into the silica network was carried out by using a new *in situ* synthesis method based on that proposed by McGilvray and co-workers.[43, 44] A desired amount of $HAuCl_4 \cdot 3H_2O$ was added to an aqueous mixture (160 mL) of the MAp solid (3.5 g). Then, the corresponding amount of I-2959 was added and the yellow solution was placed into a photoreactor and irradiated with 14 UVA lamps for 30 minutes. The final pink solution was then filtered off and the solid was washed several times with water to remove the unreacted salt.

2.2.4 Synthesis of Hybrid Materials by Absorption Approach

These materials were synthesized in a two-step process. First, MCM-41 type silica was prepared by using the reported synthesis that has been described above. Then, AuNPs were generated within the mesoporous silica solids following the same method already described.

2.2.5 Naproxen Loading

Naproxen was chosen as test molecule to study drug incorporation and delivery processes by using the new hybrid materials. The loading procedure of naproxen on the silica was based on that proposed by Vallet-Regí et al.[45] Briefly, 0.4 g of Naproxen was added to 15 mL hexane solution containing 0.4 g of the corresponding hybrid material in suspension. This solution was stirred for 12 hours while preventing the evaporation of hexane. Then, the mixture was filtered off, washed several times with hexane in order to eliminate the not absorbed drug, and air-dried. The amount of drug absorbed into the solids was determined by thermogravimetric analysis.

2.2.6 Drug Delivery

Drug release studies were performed by soaking 25 mg of the material in 7 mL of simulated body fluid (SBF) either in the dark or by exciting the localized surface plasmon resonance of the incorporated gold nanoparticles *via* 532 nm LED irradiation. The concentration of drug was monitored by UV spectroscopy. Detailed SBF preparation can be found on the Appendix of this thesis.

2.3 Results and Discussion

2.3.1 Sample Nomenclature

Due to the large number of materials synthesized, a nomenclature system was developed in order to simplify the identification of each hybrid material. Figure 2.7 shows a description of this system where M points out to the use of MCM-41 as solid support, Ap refers to APTES incorporation *via* grafting, Au stands for AuNPs and # stands for the amount of AuNPs incorporated into the material expressed in nominal %wt.

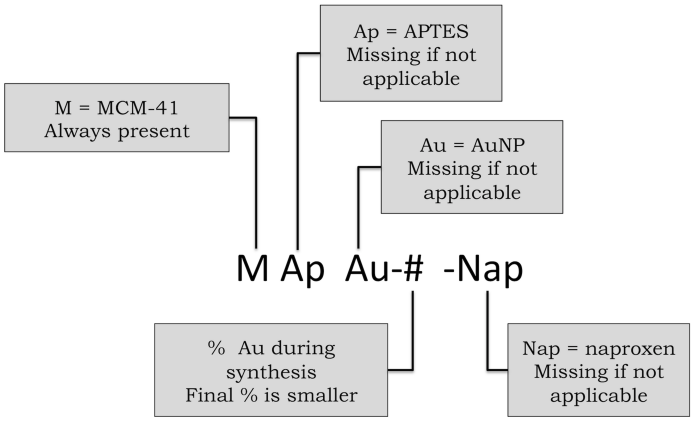

Figure 2.7: Key to sample nomenclature.

As a general rule, hybrid materials fabricated by using the grafting approach are referred to as MAp and materials synthesized by direct AuNPs absorption (no APTES present) are denoted as MAu-#.

2.3.2 Material Characterization

Transmission Electron Microscopy and Powder X-ray Diffraction

The prepared hybrid mesoporous materials were characterized by XRD and TEM in order to confirm that the mesoporous structure was maintained upon AuNPs incorporation. Figure 2.8 shows the small-angle powder X-ray diffraction spectra of the materials before and after incorporation of AuNPs.

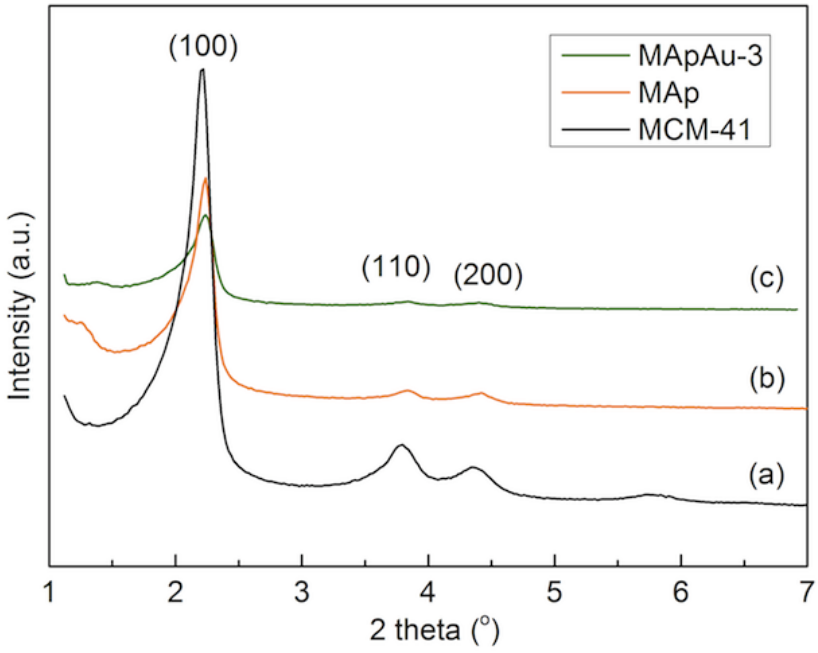

Figure 2.8: Low angle XRD patterns of pure silica MCM-41 (a) grafted MCM-41 type silica with 3-aminopropyltriethoxisilane (MAp) (b) and MCM-APTES silica after photochemical incorporation of AuNPs (MApAu-3) (c).

Figure 2.8 shows three distinctive (100), (110) and (200) XRD peaks which confirm that the 2D hexagonal mesoporous arrangement, characteristic of MCM-41, is maintained in the hybrid materials after subsequent incorporation of APTES and AuNPs. A decrease in peak intensity accompanied by a shift to higher angles are signs of in-

terplanar spacing reduction consistent with the loading of organic molecules into the mesoporous structure of MCM-41 materials caused, in this case, by the grafting of APTES pendant groups.[46, 47] Typical d-spacing values for MCM-41 can be found on Appendix A of this thesis.

TEM images of the samples also confirm that the structure of the mesoporous materials upon functionalization/incorporation of AuNPs is preserved. As expected, hybrid materials synthesized by means of the absorption approach led to larger nanoparticles even when the overall amount of gold incorporated was low, as shown in Figure 2.9b. Moreover, smaller and highly dispersed particles were achieved when following the grafting approach which involves the use of APTES as an anchoring agent between AuNPs and MCM-41 as well as low amounts of gold (Figure 2.9c). Higher gold loadings, 5 % and 10 %wt, were deemed impractical due to agglomeration.

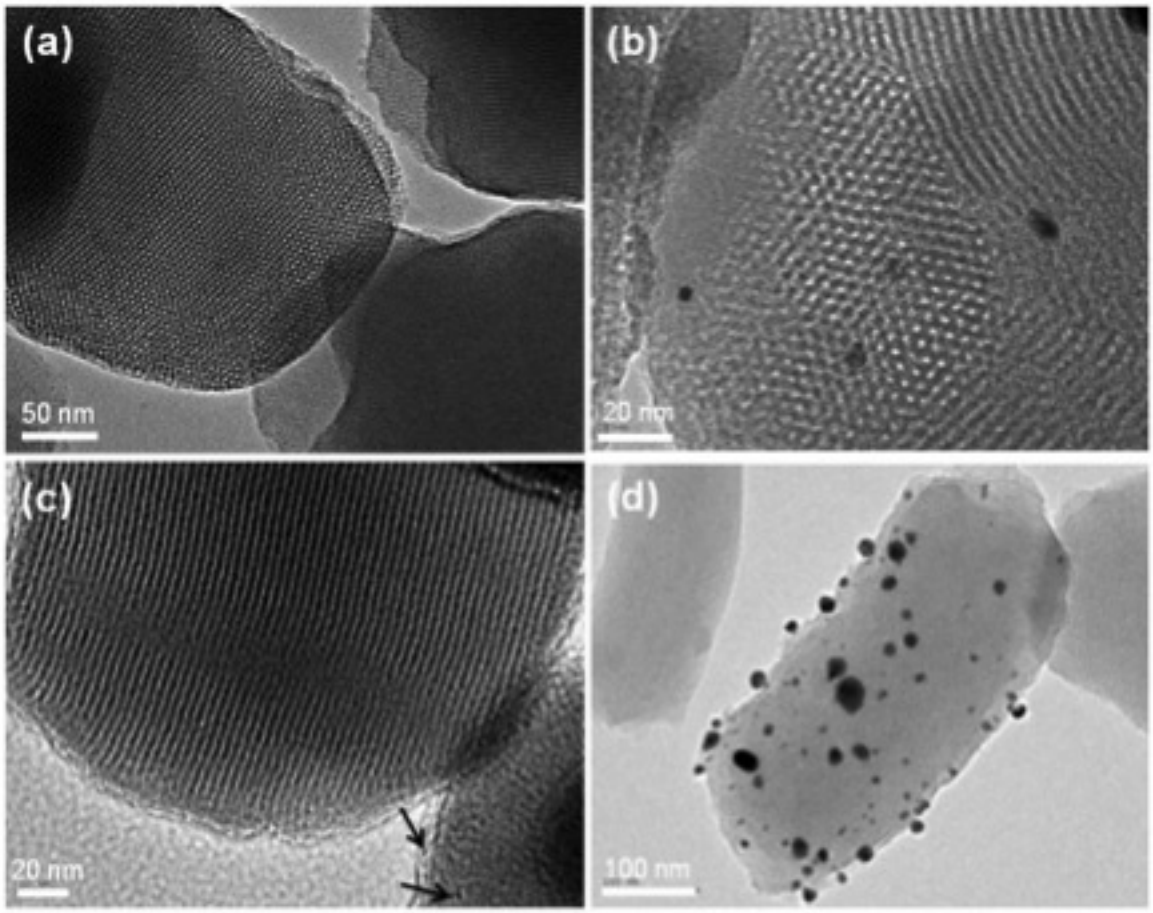

Figure 2.9: TEM micrographs of (a) pure MCM-41, hybrid materials synthesized by using the absorption route (b) MAu-3, and materials prepared following the grafting approach (c) MApAu-1, (d) MApAu-3.

Diffuse Reflectance

Diffuse reflectance measurements of the solids were performed in order to confirm the transference of the plasmonic properties of AuNPs to the hybrid mesoporous materials. It was necessary to corroborate the presence of a surface plasmon band active to the irradiation wavelength intended to use for drug delivery control. As shown in Figure 2.10 diffuse reflectance (DR) spectra of the solids have an intense surface plasmon band (SPB) at 540 nm characteristic to AuNPs [43, 44, 48] reassuring the feasibility of exciting the SPR band of these materials. The band centered at 300 nm can be attributed to the organic stabilizer (hydroxyethyl benzoic acid precursor) generated during the Norrish type I reaction involved in the synthesis of AuNPs.

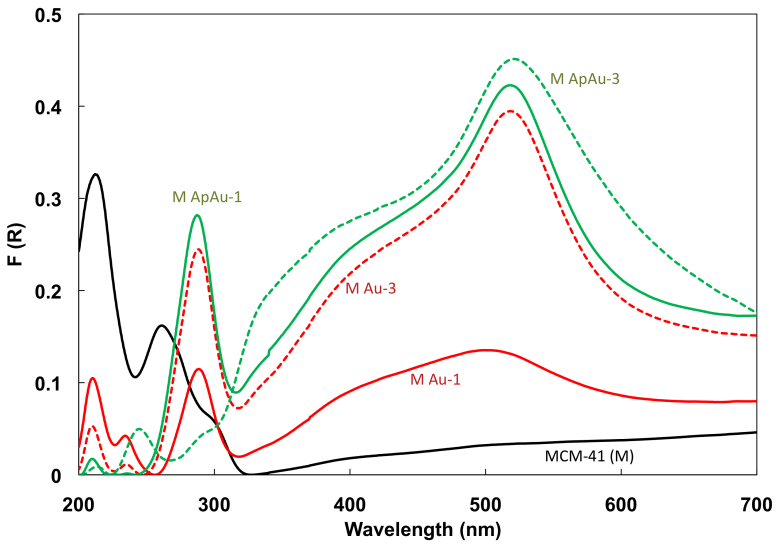

Figure 2.10: Diffuse reflectance spectra of hybrid materials as compared with the spectrum for pure MCM-41 mesoporous silica.

Nitrogen Absorption/Desorption Isotherms

All hybrid materials exhibit a type IV isotherm with a sharp nitrogen uptake at 0.35-0.45P/P_0 due to capillary condensation of nitrogen inside the mesopores and an average pore diameter of 2.7 nm, typical value for C_{16}TAB templated materials.[49] Figure 2.11a and b show a major decrease in surface area and pore volume for isotherms corresponding to grafted materials upon naproxen loading compared to materials synthesized by the absorption method indicating a higher drug loading capacity for the grafted materials.

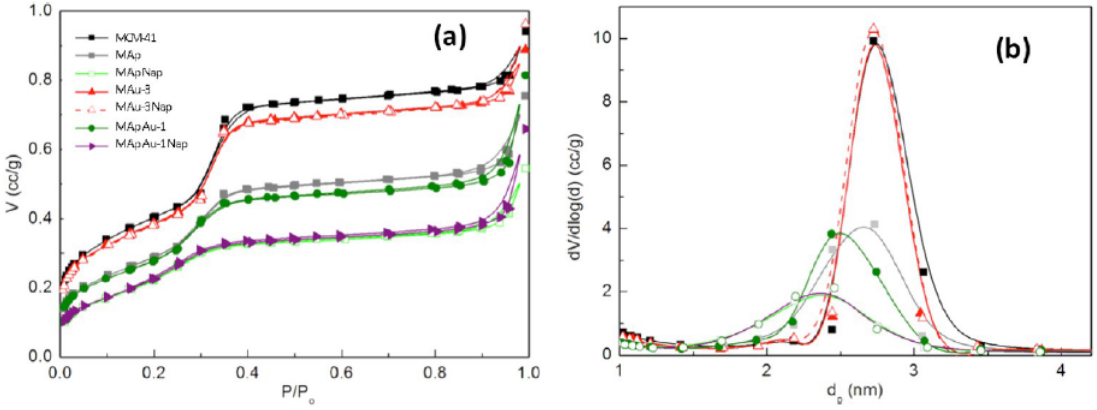

Figure 2.11: Representative nitrogen adsorption/desorption isotherms at 77 K (a) and their corresponding pore size distribution (b) of selected hybrid materials.

Textural Parameters and Thermogravimetric Analysis

A decrease in textural parameters of the solids, listed in Table 2.1, is observed. However, this decrease is more evident for the hybrid materials synthesized by the grafting approach. A reduction in surface area and pore volume is expected upon APTES and AuNPs incorporation into the porous structures suggesting a partial blocking of the porosity of the materials confirming at the same time successful functionalization.[50] Thus, the organic species responsible for this decrease are anchored to the pore surface in the mesoporous channels of the solids.

In the case of MAu-3 and MAu-3 Nap the surface area and pore volume turned out to be lower to that of the parent MCM-41 due to the inclusion of AuNPs and Naproxen. Nevertheless, the change in textural parameters was not as drastic as the one observed for the rest of the materials because of the lower naproxen loading which would compensate the decrease in textural parameters.

Table 2.1: Metal Incorporation and Textural Parameters of Representative Hybrid Mesoporous Materials

entry	sample	d_p (nm)	S_{BET} (m^2 g^{-1})	V_p(cm^3 g^{-1})	Au loading (wt%)[a]	Naproxen loading (wt%)	$HAuCl_4$ equiv[b]
1	MCM-41	2.7	945	0.95		30	
2	MAp	2.7	700	0.7			
3	MAp-Nap	2.4	620	0.5		10	
4	MApAu-1	2.4	675	0.65	0.81		1
5	MApAu-1 Nap	2.4	550	0.5	(0.81)	10	1
6	MApAu-3	2,4	615	0.6	2.5		3
7	MAu-1				unsuccessful synthesis		1
8	MAu-3	2.7	900	0.9	0.77		3
9	MAu-3 Nap	2.7	900	0.9	(0.77)	7.5	3

[a]Values in parentheses are based on the line above, as it refers to the same host material.
[b]Equivalents of $HAuCl_4$ used in the synthesis of the materials (1 equiv = 1% weight).
Note: S_{BET}, d_p and V_p correspond to surface area, pore diameter and pore volume, respectively.

Different outcomes were obtained in terms of metal content related to the number of equivalents of gold precursor used during synthesis. Materials synthesized by the grafting approach lead to two different solids with a metal loading of 0.81 and 2.5% when 1 and 3 equivalents of gold were used, respectively. Yet, for materials in which the adsorption-deposition method was used only 1% metal loading was achieved when using 3 equivalents of gold precursor (see Table 2.1).

Although it is possible to obtain two materials with similar metal loading using two different approaches (MApAu-1 and MAu-3) the adsorption-deposition method proves to be less efficient than grafting since three times more gold precursor is needed during the synthesis. These results highlight the role of APTES in overcoming the agglomeration tendency of AuNPs during the synthesis.

By minimizing agglomeration, using APTES, it is possible to obtain materials with a higher metal loading as well as optimize the use of gold precursor.

Regarding naproxen loading, a decrease was observed upon APTES functionalization compared to the parent MCM-41; this is likely due to a reduction in pore volume available for the drug to be loaded because of the presence of APTES. Moreover, a slight decrease in naproxen loading is shown after incorporation of AuNPs in the MAp material. This may reflect blockage of some pores by the AuNPs.

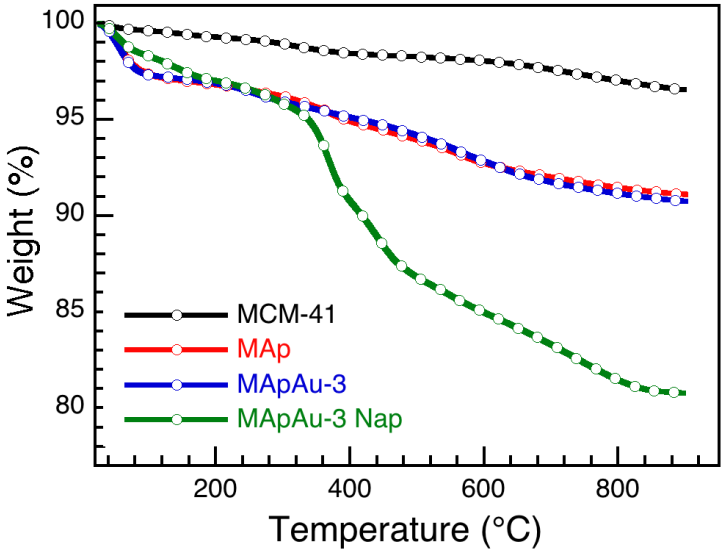

Figure 2.12: Thermogravimetric analysis for several samples. Notice the marked weight loss at around 400°C for the naproxen-containing sample.

The uptake of naproxen by the mesoporous materials was performed by 12 h exposure of the mesoporous host to a hexane solution of the drug. The sample was cleaned by extensive washing, and finally the amount of naproxen determined by TGA studies of dry samples shown in Figure 2.12.

2.3.3 Drug Release Studies

As presented in the Material Characterization section of this chapter, the hybrid mesoporous solids containing AuNPs possess an SPR band centred at approximately 540 nm making plasmon excitation of these materials possible under 532 nm LED irradiation. Experiments utilizing colloidal AuNPs suggest that temperatures around 500°C for submicrosecond times are obtained.[51] The temperatures reached upon excitation of the surface plasmon band of AuNPs incorporated in mesoporous materials have never been reported. However, the absence of naproxen decomposition in our experiments upon continuous wave irradiation at 532 nm suggests that smaller temperature changes occur in this case.

By monitoring the percentage of naproxen released as a function of time for the new materials immersed into simulated body fluid (SBF) using UV-visible spectroscopy it was possible to determine the effect of the presence of AuNPs on the release process. All of the experiments were conducted in the dark and under 532 nm light irradiation in order to excite the plasmon of AuNPs. Each point on the release plots shown in this chapter correspond to a separate release. Furthermore, the "same-batch" and batch to batch reproducibility proved to be high maintaining the trends and % naproxen released at each corresponding time. Figure 2.13 shows the control experiments for samples without AuNPs. As expected, the similarities between the curves in the dark and light irradiation showed that the latter has little or no effect on the release. Moreover, a relatively low level of naproxen is delivered.

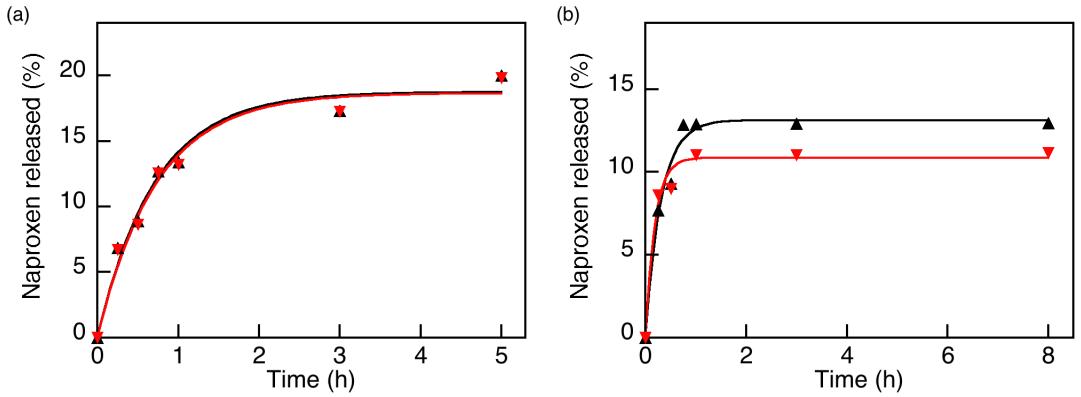

Figure 2.13: Percent naproxen release curves in time for the control samples (a) M-Nap and (b) MAp-Nap. Black curves represent a release under dark conditions and red curves represent the release performed under continuous 532 nm LED irradiation. Note: The curves shown are simply a guide to the eye and do not represent a mathematical fit.

The release profiles of the hybrid materials synthesized by using the grafting method and loaded with different amounts of AuNPs can be seen on Figure 2.14. During the first hours of the assays a faster release is observed which tends to decrease in time until reaching a plateau. These results can be interpreted as two different molecular populations, one corresponding to naproxen adsorbed on the outside surface of the material and a second population located in the pores. On the other hand, when redispersing the material used in a previous release in fresh SBF and continue the release for 48 more hours an additional 9% of naproxen was obtained suggesting the equilibrium nature of the release once the plateau has been reached.

IR spectroscopy was performed with the aim to identify and describe possible interactions between the second naproxen population and AuNPs. Unfortunately, no significant shifts or changes were observed when monitoring the carbonyl stretching band of naproxen preventing us from reaching any significant conclusion.

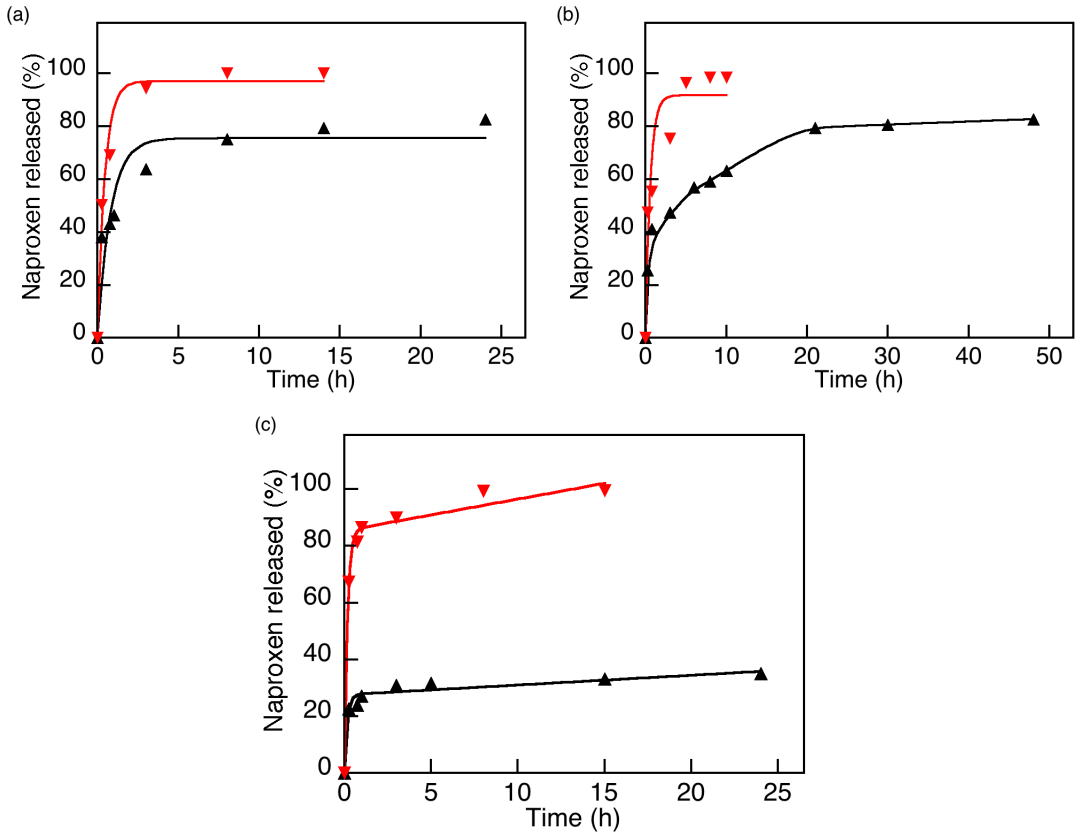

Figure 2.14: Percent naproxen release curves for MApAu-1-Nap (a), MApAu-3-Nap (b) and (c) for MAu-3-Nap. Black curves represent a release in dark conditions and red curves represent the release performed under continuous 532 nm LED irradiation. Note that even in the dark there is about 20% very fast release. Note: The curves shown are simply a guide to the eye and do not represent a mathematical fit.

When comparing the systems MApAu-3-Nap and MApAu-1-Nap under dark conditions, it was found that the former reached a plateau after 20 hours. Nonetheless, for the system MApAu-1-Nap the plateau was reached in half of the time (10 hours). These results could be related to a possible partial pore blockage due to the larger AuNPs obtained when using 3 equivalents of gold precursor. On the other hand, the much lower final % Naproxen released observed for the material in which APTES was not incorporated (MAu-3 Nap, Figure 2.14c) compared to the materials containing APTES (MApAu-1 Nap and MApAu-3, Figure 2.14a and 2.14b) indicates a higher

extent of the partial pore blockage -in the absence of APTES- suggesting a possible tendency of the AuNPs to be formed close to the pore openings when an amine anchor is not used. These results were somewhat seen on the TEM images where several more particles were found close to the pore openings when APTES was not used.

Under 532 nm irradiation, it was possible to observe a considerable increase in the speed of release as well as the final percentage of naproxen suggesting that the plasmon heating effect due to excitation of the AuNPs' plasmon band can in fact modify the dynamics of drug release. Upon excitation of the surface plasmon, most of the energy absorbed is dissipated in the form of heat that diffuses away from the surface of the nanoparticles to the surrounding medium.[52] Concomitantly, an increase in local temperature and a decrease of the local viscosity facilitates naproxen diffusion.

With the aim to further establish the possibility of controlling the molecular release process in the hybrid systems prepared, one additional assay was carried out. The test drug was delivered into SBF under dark conditions for a period of several hours. Then, light was turned on and the system was maintained under these conditions for several more hours. See Figure 2.15.

As expected, the release curves reach a plateau under dark condition followed by and increase in the rate of naproxen release as soon as the sample was irradiated at 532 nm. Beyond demonstrating light-induced release, these data provide a method to clean the material in case that one wants exclusively or predominantly photochemical cargo release.

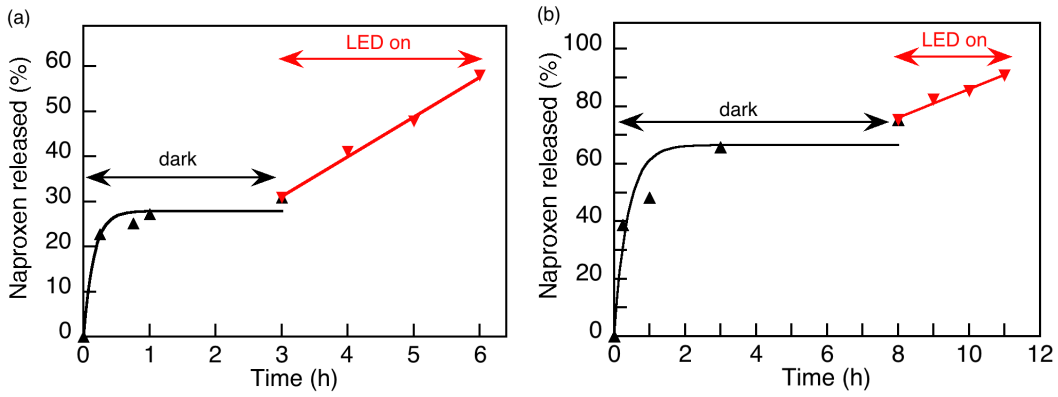

Figure 2.15: Percent naproxen release curves for MAu-3-Nap (a) and MApAu-1-Nap (b) in dark conditions (***Black***) followed by 532 nm LED irradiation (*Red*). During the limited LED exposure, the release follows reasonably well a linear dependence. Under prolonged exposure the release reaches a plateau, as expected and at close to 99 % release efficiency. Note: The curves shown are simply a guide to the eye and do not represent a mathematical fit.

In order to rule out product decomposition or APTES release and ensure that only naproxen is being released from these systems, NMR spectra were taken after the release under dark and 532 nm irradiation conditions, respectively. A comparison of these with a pure naproxen NMR confirmed that the only species released is naproxen and that no decomposition products are formed. Furthermore, the absence of a localized surface plasmon band in the UV-visible spectra of the supernatant after release -under dark and irradiation conditions- permitted to rule out the possibility of AuNP leaching.

2.3.4 Conclusions

In this chapter, the design of a new hybrid system based on the combination of the well known mesoporous MCM-41 material and gold nanoparticles prove that in fact, plasmon excitation can be used to control molecular release from these supramolecular systems. Drug delivery processes studied by using naproxen as guest molecule were tested proving that the excitation of the gold plasmon increases the rate of release of the drug out the mesoporous of the studied materials as well as the final percentage of drug delivered.

Two types of hybrid mesoporous silicas with AuNPs in their structures were synthesized. The grafting synthetic approach proved to be more efficient than adsorption-deposition in terms of AuNPs loading versus equivalents of gold precursor needed. Moreover, the adsorption-deposition approach led to agglomeration and leaching of nanoparticles when higher concentration of reagents were used, situation that was not observed for grafting materials which showed evenly dispersed AuNPs.

It is worth highlighting that the versatility and simplicity of the proposed system makes it a very good candidate for the delivery of other substances in other type of applications besides biological systems.

REFERENCES

[1] JW McBain. Persorption and monomolecular sieves. *Transactions of the Faraday Society*, 28:408–409.

[2] R Szostak. *Molecular Sieves: Principles of Synthesis and Identification*. Blackie Academic Professional, 1998.

[3] T Jiang, W Shen, Y Tang, Q Zhao, M Li, and H Yin. Stability and characterization of mesoporous molecular sieve using natural clay as a raw material obtained by microwave irradiation. *Applied Surface Science*, 254:4797–4805, 2008.

[4] ZA AlOthman and AW Apblett. Synthesis and characterization of a hexagonal mesoporous silica with enhanced thermal and hydrothermal stabilities. *Applied Surface Science*, 256:3573–3580, 2010.

[5] XY Yang, SB Zhang, ZM Qiu, G Tian, YF Feng, and FS Xiao. Stable ordered mesoporous silica materials templated by high-temperature stable surfactant micelle in alkaline media. *Journal of Physical Chemistry B*, 108:4696–4700, 2004.

[6] JS Beck, JC Vartuli, WJ Roth, ME Leonowicz, CT Kresge, KD Schmitt, CTW Chu, DH Olson, EW Sheppard, SB McCullen, JB Higgins, and JL Schlenkert. A new family of mesoporous molecular sieves prepared with liquid crystal templates. *Journal of the American Chemical Society*, 114:10834–10843, 1992.

[7] L Zhang, S Qiao, Y Jin, L Cheng, Z Yan, and GQ Lu. Hydrophobic functional

group initiated helical mesostructured silica for controlled drug release. *Advanced Functional Materials*, 18(23):3834–3842, 2008.

[8] Y Wan and D Zhao. On the controllable soft-templating approach to mesoporous silicates. *Chemical Reviews*, 107(7):2821–2860, 2007.

[9] J Zhang, ZF Yuand, WH Chen, GF Luo, SX Cheng, RX Zhuo, and XZ Zhang. Multifunctional envelope-type mesoporous silica nanoparticles for tumor-triggered targeting drug delivery. *Journal of the American Chemical Society*, 135(13):5068–5073, 2013.

[10] AC Pradhan, B Nanda, KM Parida, and GR Rao. Fabrication of the mesoporous Fe@MnO_2NPs-MCM-41 nanocomposite: An efficient photocatalyst for rapid degradation of phenolic compounds. *Journal of Physical Chemistry C*, 119(25):14145–14159, 2015.

[11] LV Ng, P Thompson, J Sánchez, CW Macosko, and AV McCormick. Formation of cage-like intermediates from nonrandom cyclization during acid-catalyzed sol-gel polymerization of tetraethyl orthosilicate. *Macromolecules*, 28:6471–6476, 1995.

[12] J Wen and GL Wilkes. Organic/inorganic hybrid network materials by the sol-gel approach. *Chemistry of Materials*, 8:1667–1681, 1996.

[13] M Nogami and Y Moriya. Glass formation through hydrolysis of silicon acetate with ammonium hydroxide and hydrochloric acid solution. *Journal of Non-Crystalline Solids*, 37:191–201, 1980.

[14] ZA AlOthman. A review: Fundamental aspects of silicate mesoporous materials. *Materials*, 5:2874–2902, 2012.

[15] BM Lok, TR Cannon, and CA Messina. The role of organic molecules in molecular sieve synthesis. *Zeolites*, 3:282–291, 1983.

[16] EM Flaigen, RL Patton, and ST Wison. Structural, synthetic and physicochemical concepts in aluminophosphate-based molecular sieves. *Studies in Surface Science and Catalysis*, 37:13–27, 1988.

[17] CT Kresge, ME Leonowicz, WJ Roth, JC Vartuli, and JS Beck. Ordered mesoporous molecular sieves synthesized by a liquid-crystal template mechanism. *Nature*, 359:710–722, 1992.

[18] JS Beck, JC Vartuli, WJ Roth, ME Leonowicz, CT Kresge, KD Schmitt, CTW Chu, DH Olson, EW Sheppard, SB McCullen, JB Higgins, and JL Schlenkert. A new family of mesoporous molecular sieves prepared with liquid crystal templates. *Journal of the American Chemical Society*, 114:10834–10843, 1992.

[19] L Mercier and TJ Pinnavaia. Direct synthesis of hybrid organic-inorganic nanoporous silica by a neutral stoichiometric incorporation of organosiloxane molecules. *Chemistry of Materials*, 12:188–196, 2000.

[20] MH Lim and A Stein. Comparative studies of grafting and direct syntheses of inorganic-organic hybrid mesoporous materials. *Chemistry of Materials*, 11:3285–3295, 1999.

[21] AI Carrillo, J García-Martínez, R Llusar, E Serrano, I Sorribes, C Vincent, and JA Vidal-Moya. Incorporation of cubane-type Mo_3S_4 molybdenum cluster sulfides in the framework of mesoporous silica. *Microporous and Mesoporous Materials*, 151:380–389, 2012.

[22] BG Trewyn, CM Whitman, and VSY Lin. Control of room-temperature ionic

liquid templated mesoporous silica nanoparticles for controlled release of antibacterial agents. *Nano Letters*, 4(11):2139–2143, 2004.

[23] J Lu, M Liong, Z Li, JI Zink, and F Tamanoi. Biocompatibility, biodistribution, and drug-delivery efficiency of mesoporous silica nanoparticles for cancer therapy in animals. *Small*, 6(16):1794–1805, 2010.

[24] II Slowing, BG Trewyn, S Giri, and VSY Lin. Mesoporous silica nanoparticles for drug delivery and biosensing applications. *Advanced Functional Materials*, 17(8):1225–1236, 2007.

[25] JL Vivero-Escoto, II Slowing, CW Wu, and VSY Lin. Photoinduced intracellular controlled release drug delivery in human cells by gold-capped mesoporous silica nanospheres. *Journal of the American Chemical Society*, 131(10):3462–3466, 2009.

[26] M Vallet-Regí, A Ramila, RP del Real, and J Pérez-Pariente. A new property of MCM-41: Drug delivery system. *Chemistry of Materials*, 13(2):308–311, 2001.

[27] C Coll, A Bernardos, R Martínez-Mánez, and F Sancenón. Silica mesoporous supports for controlled release and signaling applications. *Accounts of Chemical Research*, 46(2):339–349, 2013.

[28] Y Perrie and T Rades. *Pharmaceutics: Drug Delivery and Targeting*. FASTtrack. Pharmaceutical Press, 2009.

[29] D Arcos and M Vallet-Regí. Bioceramics for drug delivery. *Acta Materialia*, 61(3):890–911, 2013.

[30] NK Mal, M Fujiwara, Y Tanaka, T Taguchi, and M Matsukata. Photo-switched

storage and release of guest molecules in the pore void of coumarin-modified MCM-41. *Chemistry of Materials*, 15(17):3385–3394, 2003.

[31] Y Gao, Y Chen, X Ji, X He, Q Yin, Z Zhang, J Shi, and Y Li. Controlled intracellular release of doxorubicin in multidrug-resistant cancer cells by tuning the shell-pore sizes of mesoporous silica nanoparticles. *ACS Nano*, 5(12):9788–9798, 2011.

[32] E Aznar, F Sancenon, MD Marcos, R Martínez-Mánez, P Stroeve, J Cano, and P Amorós. Delivery modulation in silica mesoporous supports via alkyl chain pore outlet decoration. *Langmuir*, 28(5):2986–2996, 2012.

[33] CY Lai, BG Trewyn, DM Jeftinija, K Jeftinija, S Xu, S Jeftinija, and VSY Lin. A mesoporous silica nanosphere-based carrier system with chemically removable cds nanoparticle caps for stimuli-responsive controlled release of neurotransmitters and drug molecules. *Journal of the American Chemical Society*, 125(15):4451–4459, 2003.

[34] E Aznar, MD Marcos, R Martínez-Mánez, F Sancenón, J Soto, P Amorós, and C Guillem. ph and photo-switched release of guest molecules from mesoporous silica supports. *Journal of the American Chemical Society*, 131:6833–6843, 2009.

[35] G Cosa, M Lukeman, and JC Scaiano. How drug photodegradation studies led to the promise of new therapies and some fundamental carbanion reaction dynamics along the way. *Accounts of Chemical Research*, 42(5):599–607, 2009.

[36] E Ruiz-Hernández, A Baeza, and M Vallet-Regí. Smart drug delivery through DNA/magnetic nanoparticle gates. *ACS Nano*, 5(2):1259–1266, 2011.

[37] KMN Ravi. Nano and microparticles as controlled drug delivery devices. *The Journal of Pharmacy and Pharmaceutical Sciences*, 3(2):234–258, 2000.

[38] YH Jin, S Kannan, M Wu, and JXJ Zhao. Toxicity of luminescent silica nanoparticles to living cells. *Chemical Research in Toxicology*, 20:1126–1133, 2007.

[39] K Kostraelos, L Lacerda, GPastorin, W Wu, S Wieckowski, J Luangsivilay, S Godefroy, DPantarotto, JP Briand, S Muller, M Prato, and A Bianco. Cellular uptake of functionalized carbon nanotubes is independent of functional group and cell type. *Nature Nanotechnology*, 2:108–113, 2007.

[40] AM Alkilany and CJ Murphy. Toxicity and cellular uptake of gold nanoparticles: What have learned so far? *Journal of Nanoparticle Research*, 12:2313–2333, 2010.

[41] L French. Dysmenorrhea. *American Family Physician*, 71(22):285–291, 2005.

[42] P Kubelka. New contributions to the optics of intensely light-scattering materials. *The Journal of the Optical Society of America*, 38(5):448–457, 1948.

[43] KL McGilvray, MR Decan, D Wang, and JC Scaiano. Facile photochemical synthesis of unprotected aqueous gold nanoparticles. *Journal of the American Chemical Society*, 128(50):15980–15981, 2006.

[44] KL McGilvray, C Fasciani, CJ Bueno-Alejo, R Schwartz-Narbonne, and JC Scaiano. Photochemical strategies for the seed-mediated growth of gold and gold-silver nanoparticles. *Langmuir*, 28(46):16148–16155, 2012.

[45] M Vallet-Regí, A Ramila, RP del Real, and JA Pérez-Pariente. New property of MCM-41: Drug delivery system. *Chemistry of Materials*, 13(2):308–311, 2001.

[46] M Kruk, T Asefa, M Jaroniec, and GA Ozin. Metamorphosis of ordered mesopores to micropores: Periodic silica with unprecedented loading of pendant reactive organic groups transforms to periodic microporous silica with tailorable pore size. *Journal of the American Chemical Society*, 124(22):6383–6392, 2002.

[47] EW Nuffield. *X Ray Diffraction Methods*. Wiley, 1966.

[48] S Eustis and MA El-Sayed. Why gold nanoparticles are more precious than pretty gold: Noble metal surface plasmon resonance and its enhancement of the radiative and nonradiative properties of nanocrystals of different shapes. *Chemical Society Reviews*, 35(3):209–217, 2006.

[49] AI Carrillo, N Linares, E Serrano, and J García-Martínez. Well ordered mesoporous interconnected silica spheres prepared using extremely low surfactant concentrations. *Materials Chemistry and Physics*, 129(2):261–269, 2011.

[50] AI Carrillo, E Serrano, R Luque, and J García-Martínez. Microwave-assisted catalysis by iron oxide nanoparticles on MCM-41: Effect of the support morphology. *Applied Catalysis A: General*, 453(0):383–390, 2013.

[51] C Fasciani, C Bueno-Alejo, M Grenier, JC Netto-Ferreira, and JC Scaiano. High-temperature organic reactions at room temperature using plasmon excitation: Decomposition of dicumyl peroxide. *Organic Letters*, 2(13):204–207, 2011.

[52] AO Govorov and HH Richardson. Generating heat with metal nanoparticles. *Nano Today*, 2(1):30–38, 2007.

Chapter 3

Visible and NIR Plasmon Mediated Molecular Release from Cucurbit[6]uril Mesoporous Gated Systems

3.1 Gated Systems

Controlled drug delivery offers a series of advantages. As mentioned in Chapter 2, by being able to control and modify rates of release it is possible to minimize drug degradation and loss, prevent side effects, reduce the toxicity as well as to improve the efficacy of the release. Nevertheless, besides controlling the delivery process itself it is as important to be able to control the start point of the delivery in order to maximize the advantages presented above.

Considerable efforts have been put into regulating the beginning of the delivery process in order to efficiently open the system at the right time and in the proper location. Several gate mechanisms have been implemented in order to fulfill these expectations. The gates of the various systems have been designed to be activated either by changes in the surrounding media such as pH and temperature [1, 2, 3, 4, 5] or activated by external stimuli such as the application of a magnetic field or light irradiation, among others.[6, 7, 8, 9, 10] For drug delivery systems, "zero" premature release and stimuli-responsive controlled delivery of cargo molecules are the two main conditions that will confer the system with high therapeutic efficacy and low cytotoxicity. Traditional drug delivery systems depend mainly on simple diffusion and/or degradation of the carrier. However, the broad possibility of functionalizing silica based mesoporous materials with capping agents also make these materials good candidates for being functionalized with gates in order to achieve "zero" premature release.[11, 12, 13] Several methods have been used to put gates into mesoporous silica materials ranging from functionalization of the pore openings of the mesoporous material with photo-reversible dimers [14] to pore blocking by means of metallic nanoparticles or polymers, among other agents.[15, 16]

A set of very interesting gated systems were designed by Zink and Stoddart consisting of MCM-41 as a drug container and cucurbit[n]urils as stimuli responsive lids capable of controlling the starting point of the cargo release. By making use of the chemical versatility of MCM-41 it was possible to further functionalize its surface with side-chains bearing a CBn binding site. Various CBn/tether complexes were implemented according to the stimuli that wanted to be tested. Some of the stimuli included the addition of a competitive guest[17, 18], pH increase [19, 20, 21], reductive cleavage of a stopper[22] or magnetically induced heating of Zn-doped Fe_3O_4 nanoparticles.[23] Upon the application of the proper stimulus, the CBn lids are ejected from the system allowing the drug to diffuse in solution.

This research demonstrates the great advantage of combining the properties of mesoporous materials and the cucurbit[n]uril family to achieve the so desired "zero" premature release.

3.1.1 The Cucurbit[n]uril Family

The Cucurbit[n]uril (CBn) family is composed of several macrocyclic molecules self-assembled from an acid catalyzed condensation reaction between glycouril and formaldehyde. These peculiar macrocycles form a cavity with exceptional recognition properties -such as fluorescence and absorption enhancement allowing to remarkably improve the limit of detection of certain molecules- determined by the size of such cavity which in turn depends on the number of glycouril monomers that conform the macrocyclic unit. Figure 3.1 and Table 3.1 show the basic cucurbituril structures and their corresponding dimensions.[24]

	CB[5]	CB[6]	CB[7]	CB[8]
Outer Diameter (Å)	13.1	14.4	16	17.5
Portal Cavity (Å)	2.4	3.9	5.4	6.9
Interior Cavity (Å)	4.4	5.8	7.3	8.8

Table 3.1: Dimensions of the basic members of the cucurbituril family.

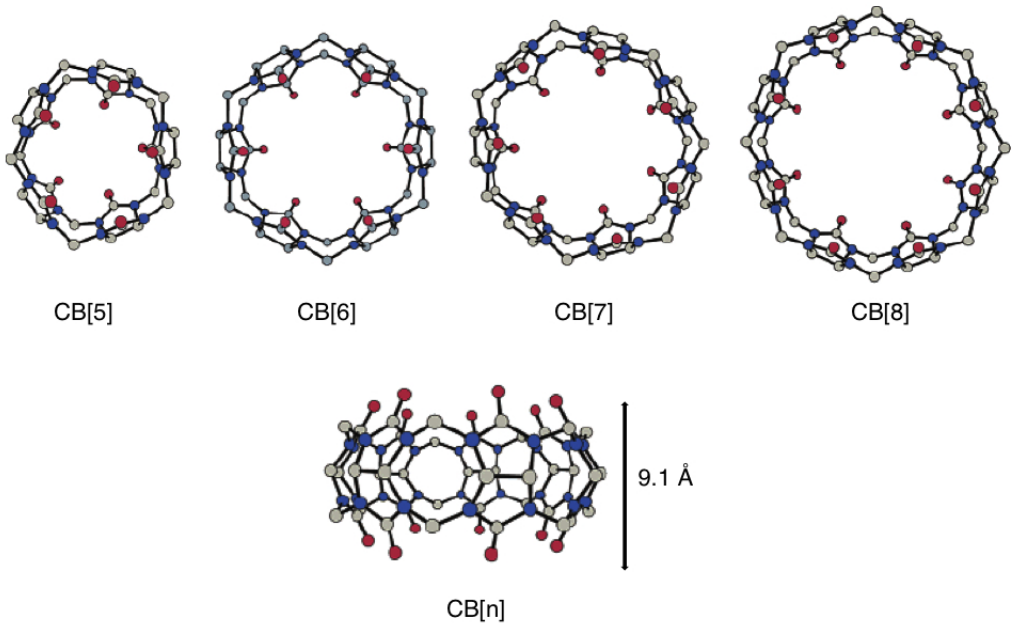

Figure 3.1: Molecular structures of the basic members of the cucurbituril family. Reproduced from [25] with permission of The Royal Society of Chemistry.

It wasn't until 1981 when Mock *et.al* fully characterized and described the nature of the Cucurbit[6]uril (CB6) structure.[26] Ever since then, the interest in the cucurbituril family has increased dramatically following the preparation of new CB[n] homologues [27] and a vast variety of CB[n] derivatives.[28, 29]

The main feature of this family of macrocycles is their capability to serve as hosts for small molecules. This is possible due to their highly symmetric structure composed by a hydrophobic cavity with carbonyl rims.

The electrostatic potential map shown in Figure 3.2 accounts for the high electron density located on the oxygen atoms of the carbonyl groups at both cavity openings reflecting affinity of the entrance for positively charged species. Besides the non dipolar nature of the cucurbituril macrocycle, the cavity itself has no functional groups or electron pairs facing the inside indicating its highly hydrophobic nature due to the impossibility of forming hydrogen bonds. However, in spite of the cavity being hydrophobic and being overall non polar molecules, the cucurbituril family is characterized by having very high quadrupole moments exhibiting high-order electrostatic interactions.[30]

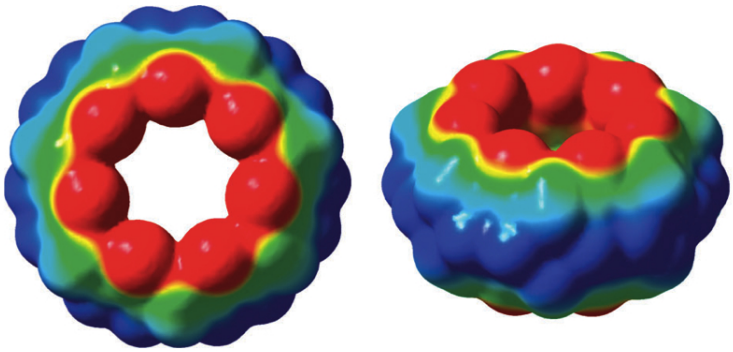

Figure 3.2: Electrostatic potential map of cucurbit[7]uril. The red to blue color range spans -80 to +40 kcal mol^{-1}. Reproduced from [30] with permission of The Royal Society of Chemistry.

The hydrophobic cavity of a cucurbituril host is a microenvironment on its own and will drastically affect the properties of the guest molecule once encapsulated. Changes in fluorescence, absorption and NMR spectra of the guest are common upon complexation with a cucurbituril macrocycle because of the variations in electronic and/or magnetic environment compared to that when the guest is free.

3.1.2 Encapsulation of Alkylammonium Ions

The first evidence regarding the inclusion of alkylammonium ions into cucurbituril type molecules was reported by Freeman *et.al* in 1981 [26] when up-field shifts of approximately 1 ppm were observed in the corresponding ^{1}H-NMR spectra of aliphatic amines in the presence of cucurbit[6]uril in acidic medium. An analogous situation was observed for alkyldiammonium ions where the above mentioned up-field shifts would correspond to the formation of a host-guest complex in which the cationic termini of the alkanediamine interact with the negative part of the carbonyl dipoles located at the openings of CB6 while the alkyl chain would remain encapsulated in the hydrophobic cavity. The interior of CB6 constitutes a proton-shielding region relative to the acidic medium in which the host would be solvated. The alkyl shifts induced are claimed to be a cumulative effect related to the uril residues which present their corresponding faces to the interior of the cavity.[31] Figure 3.3 shows the corresponding ^{1}H-NMR shifts upon inclusion of alkanediammonium ions in the cavity of CB6. As can be seen, the region in which larger shifts are observed extends for approximately 6 Å which roughly corresponds to 4.5 methylene units and coincides with the interatomic distance between the carbonyl oxygens from one rim to the other.

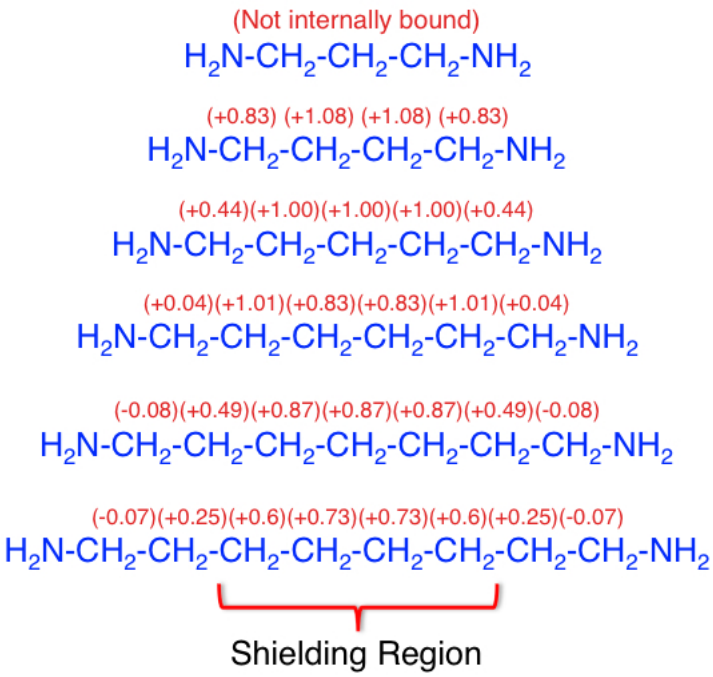

Figure 3.3: Induced ^{1}H-NMR shifts (ppm) corresponding to the methylene groups of alkanediammonium ions upon complexation with CB6. Adapted with permission from [31]. Copyright (2017) American Chemical Society.

In spite of the fact that the three hydrogens of the cationic portion of the guests can form hydrogen-bonds with the oxygen atoms of alternate carbonyl groups lying on the CB6 rim it was proven that the affinity of both primary and secondary ammonium ions is 1000-fold greater than that of the tertiary ammonium. As a result, it was concluded that one of the three protons on the nitrogen projects away of the opening while the other two interact with carbonyl groups.

Mechanisms of Inclusion of Alkaneammonium Ions in CB6

In the early 2000's Nau *et.al* reported the mechanism of complexation of several alkylammonium salts and CB6.[32, 33] Two possible pathways were described that account for the two main variables that influence the mechanism of host-guest complexation, namely the degree of protonation of the amino group and the size of the alkyl chain. Accordingly, when the amine is in a neutral state, meaning that the pH of the medium is above the pK_a of the amine (10.5), and/or the alkyl chain is long a direct penetration of the alkyl chain into the cavity of CB6 occurs followed by immediate protonation of the amine residue.

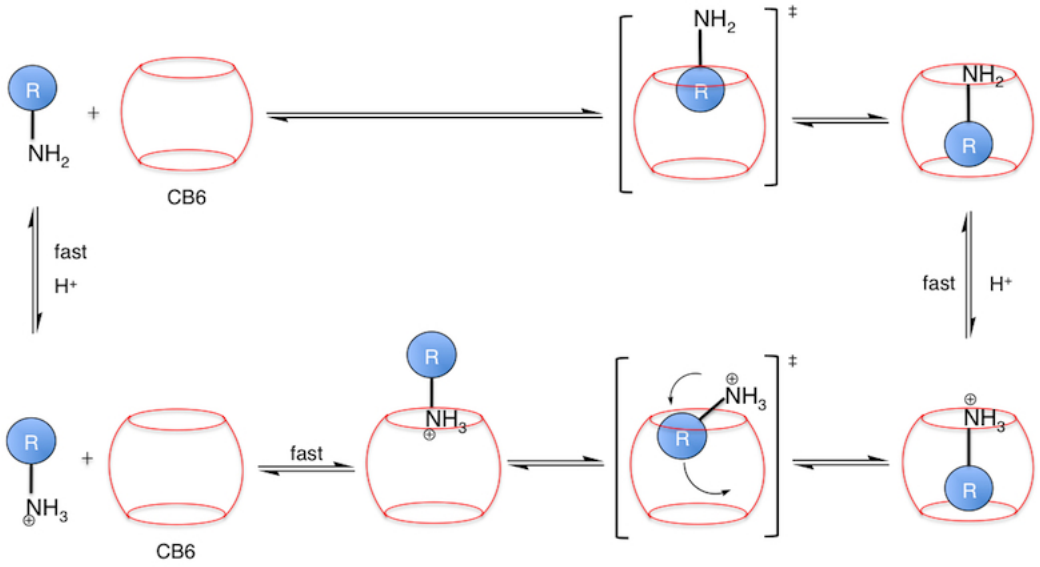

Figure 3.4: Mechanism of inclusion of alkaneammonium ions into CB6. Adapted with permission from [33]. Copyright (2017) American Chemical Society.

In contrast, when the amine group is in its protonated state ($pH < pK_a$) a coordination complex is formed between the ammonium ion and the carbonyl rich opening of CB6 while the alkyl chain remains exposed to the aqueous phase. Then, the entry of the organic residue occurs in what has been described as "flip-flop" manner which

involves a different transition state that requires the distortion of the CB6 opening. This is the determining step of the guest's rate of ingression.

In spite of this pathway being slower than the direct amine inclusion the complete loss of the ion-dipole stabilizing interaction is avoided generating a complex in which the ammonium ion is still partly coordinated.

Mechanism of Inclusion of Alkanediammonium Salts

The mechanism of inclusion of alkaneammonium ions that contain two termini amino groups has never been unveiled. Furthermore, when the alkanediammonium ion is functionalized on the exterior and/or interior surface of a solid material such as MCM-41 or to a molecular structure that is unable to fit in the cucurbituril cavity the "flip-flop" mechanism does not apply. Since one of the ends of the diamino tether is blocked it requires the CB6 host to slip through the N1 amino group.[34] Such is the case of 1,6-hexanediamine grafted on MCM-41 used in the research presented in this chapter.

The cucurbituril slippage can occur *via* threading of either the ammonium group or its corresponding neutral amine through the cavity of cucurbituril. In the case of charged species, the process would involve threading along the ammonium ion without involving any chemical transformation. On the other hand, the pathway that involves the corresponding neutral amine going through the cucurbituril cavity would entail initial deprotonation of the ammonium ion by one of the carbonyl groups on the cucurbituril opening followed by acid-base equilibrium with the aqueous media that would return the carbonyl to its neutral form. The neutral amine would then slip through the cavity to then be reprotonated on the other side of the CBn by a protonated carbonyl group.[34] (see Figure 3.5).

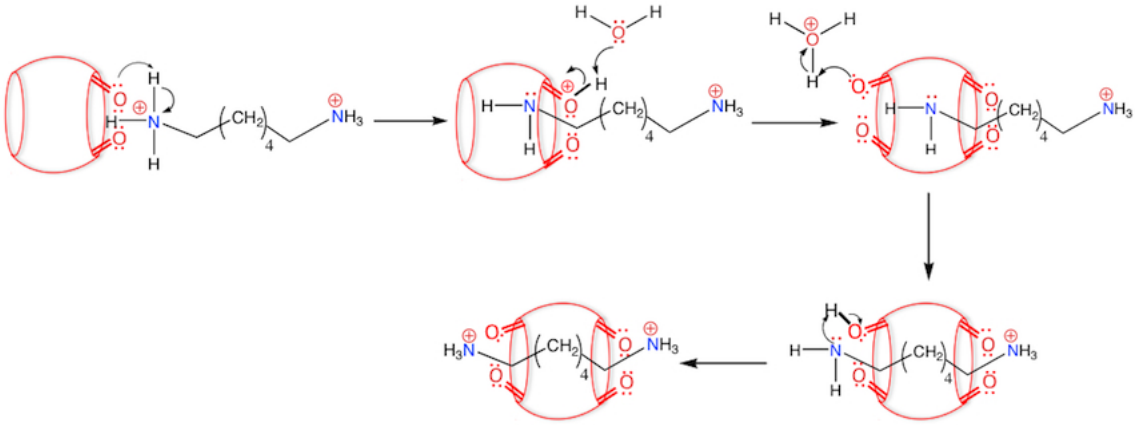

Figure 3.5: Mechanism of inclusion of alkanediammonium ions into CB6 through a neutral amine pathway. Adapted with permission from [34]. Copyright (2017) American Chemical Society.

Even though in silico studies have shown the neutral amine pathway as the most favorable no experimental evidence has been obtained indicating the transition of either charged or neutral amines through the CBn cavity.

3.1.3 Complexation Driving Force and High-Energy Water Molecules

Numerous literature reports have highlighted the importance of guest size and ion-dipole interactions between the positively charged host residues and the carbonyl rim of cucurbit[n]urils.[31, 35, 36] However, an important additional factor that must be considered is the confinement of water molecules in the cucurbituril cavity prior host-guest complexation. The reduced space in which these water molecules are, makes the water-water interactions less favorable compared to those in the bulk solution since the possibility of optimizing hydrogen bonds is impaired.[37] At the same time, they have a less favorable potential energy since the dipole-dipole interactions between water molecules are not sufficiently counterbalanced due to the weak nature of the

interactions between them and the hydrophobic cavity. It is because of this reason that the water molecules located inside the CBn cavity prior host-guest complexation are named "high-energy" water molecules and their displacement upon guest encapsulation is energetically favored. Direct host-guest interactions on their own can not account for the high binding affinities of CBn. The driving force responsible for the encapsulation of hydrophobic guests inside cucurbiturils is determined by the number of water molecules the guests has initially included in its cavity and their subsequent displacement.[30] (See Figure 3.6).

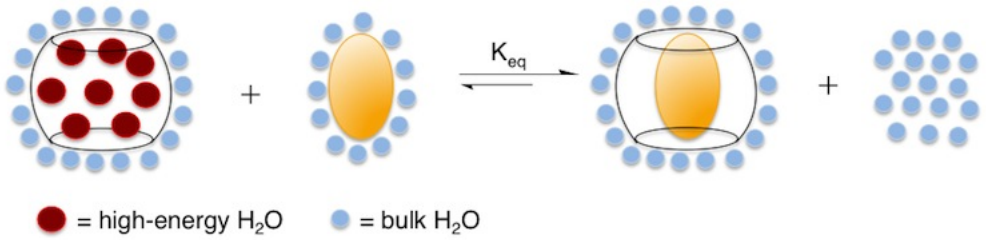

Figure 3.6: Displacement of high-energy water molecules upon host-guest complexation. Reproduced with permission from [37]. Copyright (2017) American Chemical Society.

3.1.4 Dye Encapsulation and Fluorescence Enhancement

A vast variety of studies have been performed using dye probes whose optical properties are highly sensitive to solvent polarity.[38, 39, 40, 41, 42] Fluorescence enhancement is often observed when cucurbit[n]uril hosts are added to aqueous solutions of fluorescent dyes. Upon host-guest complexation the dyes are immersed in a more hydrophobic environment due to the nature of the cucurbituril cavity described in previous sections of this chapter. However, it is worth to consider that changes in the immediate environment is not the only reason for fluorescence enhancement but also any other changes that contribute to the inhibition of non radiative decay pathways

such as changes in rotational freedom upon complexation.[43]

In 2009, Feng *et.al* studied the interaction between various cucurbituril macrocycles and a set of hydrochloride salts of the imidazole derivatives shown in Figure 3.7 in aqueous solution.[44]

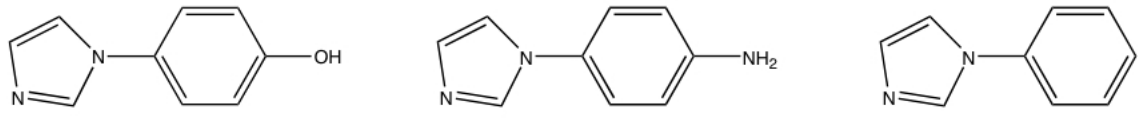

1 **2** **3**

Figure 3.7: Structures of the phenyl imidazole derivatives studied by Feng *et.al*.

By means of ^{1}H-NMR analysis it was concluded that a 1:1 inclusion complex is formed between the imidazole derivatives and cucurbit[6]uril. Moreover, the phenyl portion of the studied guests is located inside the cavity of CB6 (shielding region) while the imidazole portion is located in the deshielding zone at the carbonyl portal of the host. X-ray structures confirmed that the closest contacts occur between the amine cation of the imidazole portion and the oxygen atoms of the carbonyl rim while the phenyl ring sits in line with opposite sets of the opening carbonyl oxygens. Fluorescence studies further confirmed the formation of a 1:1 host-guest complex with CB6 concomitantly exhibiting a fluorescence enhancement effect of the encapsulated guests.

3.1.5 About this Chapter

A more complex set of mesoporous hybrid materials were designed and synthesized based on the fact -demonstrated in Chapter 2- that the surface plasmon band of supported gold nanoparticles can be used to control the rate of cargo release from mesoporous-based supramolecular systems. In this chapter, several systems are presented in which it is possible to control both the start and rate of the cargo release *via* surface plasmon excitation. A series of advantages were conferred by each one of the modification/optimization steps presented below.

Inclusion of Thermoresponsive Gates

As presented earlier in this chapter, the cucurbit[n]uril family has demonstrated to have considerable potential as a stimuli responsive gate. It has been previously demonstrated that if the proper cucubrituril host and guest molecule combination is used it is possible to achieve "zero" premature release when using MCM-41 as a drug carrier.[19, 17] 1,6-Hexanediamine and cucurbit[6]uril were chosen as the host-guest couple to construct the gates of our systems based on the fact that the alkane length of the selected guest is optimum for its inclusion in the cavity of CB6 (See Figure 3.3) and it has been demonstrated that this host-guest couple is in fact thermoresponsive.[23] Hence, by functionalizing the materials with a guest tether capable of forming a thermoresponsive cucurbit[6]uril-hexane diamine (CB6-Hex) host-guest complex it was possible to close the system and achieve "zero" premature release of the model drug Naproxen.

In vitro and *in vivo* cell growth assays -reported in the literature- using both animal and human cells as well as bacteria have shown that cucurbiturils possess practically no citotoxicity. Furthermore, living cell imaging studies have ruled out internal cell damage in the presence of cucurbituril type molecules, highlighting an

initial proof-of-concept towards the use of CB[n] in drug delivery applications.[45, 46]

CB6 was purposely used instead of CB7 or other members of the cucurbituril family due to its smaller portal cavity diameter (3.9 $\mathring{A}$ vs 5.4 $\mathring{A}$) decreasing the probability of undesired secondary host-guest complexes, such as the encapsulation of the drug being delivered upon gate opening. The complete absence of evidence in the literature regarding Naproxen-CB6 complex formation supports the selection of CB6 as a guest for the studied gated systems.

Incorporation of gold nanostructures

Incorporation of gold nanoparticles (AuNP), gold nanorods (AuNR) or both provided the systems of the light activation component needed to open the gates and control the diffusion of the drug by surface plasmon heating effect. Most drug delivery systems, if not all of them, either control the start of the release or the rate at which the drug is being delivered. However, the devices presented here provide the significant advantage of being able to control both start and cargo release by means of the same type of external stimulus making use of the spatial control that photochemistry provides. Furthermore, the fact that these can be remotely activated by using visible or infra red irradiation broadens the spectrum of biological samples where these systems could be used avoiding sample damage incurred when using UV light and increasing tissue penetration by adding an infrared component. Other very interesting examples using a similar approach have been previously developed.[47, 48, 49] Nevertheless, the feature of wavelength-controlled rate of release accompanied by the use of a simpler and cheaper irradiation source -LED vs laser- and much lower irradiation powers make the systems proposed in this work to differentiate.

3.2 Experimental

3.2.1 Reagents

Ammonium hydroxide was purchased from Fisherbrand while hexadecyltrimethylammonium bromide (C_{16}TAB), tetraethyl orthosilicate (TEOS), (3-chloropropyl) triethoxysilane (CPTES), 1,6-Hexanediamine, cucurbit[6]uril hydrate, chloroauric acid trihydrate ($HAuCl_4 \cdot 3H_2O$), 5-bromosalicylic acid, $AgNO_3$, and Naproxen were purchased from Sigma-Aldrich and used as received.
Hydroxy-1-[4-(2-hydroxyethoxy)phenyl]-2-methyl-1-propanone (I-2959) was obtained from Basf Chemicals Company. All solvents used were spectroscopic grade.

3.2.2 Instrumentation

X-ray Diffraction Studies

Small-angle powder X-ray diffraction (XRD) analysis was carried out using a Rigaku Ultima IV difractometer Cu Kα radiation (k = 1.541836), operating at 40kV and 30 mA, at a scanning velocity of 0.03° min^{-1} in the $0.7° < 2\theta < 10°$ range.

Inductively Coupled Plasma Optical Emission Spectroscopy (ICP-AES)

Metal loading in the materials was determined by a Hewlett-Packard 4500 ICP quadrupole mass spectrometer (Hewlett-Packard, Yokogawa Analytical Systems, Tokyo, Japan). Platinum sampler and skimmer were employed, together with a quartz double-pass spray chamber that was cooled at 1°C by a closed circuit refrigerating system. Samples were introduced into the instrument using a micro flow nebulizer (Agilent Technologies, Palo Alto, CA). An amount of 10 mg of every sample was digested in 1 mL HCl/H_2SO_4 during 12 hours prior to analysis.

UV-visible Spectroscopy

Diffuse reflectance UV-Visible data of pressed powders were recorded on a UV-vis spectrophotometer Cary 100 with Har-153 rick praying mantis accessory, in a wavelength range from 200 to 600 nm, and recalculated following the Kubelka-Munk function.[50]

Thermogravimetric Analysis (TGA)

Hexamethylenediamine and Naproxen loadings were determined by thermogravimetric analysis using a Q5000 TA instrument equipped with QSeries operating software.

Transmission Electron Microscopy

The morphology of the mesoporous materials was characterized by transmission electron microscopy (TEM). TEM analyses were carried out on a JEM-2010F microscope (JEOL, 200 kV, 0.14 nm resolution). For this purpose, samples were prepared by dipping a sonicated suspension of the material in ethanol on a carbon-coated copper grid. The digital analysis of the TEM micrographs was done using DigitalMicrographTM 3.6.1 by Gatan.

3.2.3 Synthesis of Chlorine-Functionalized MCM-41 (MCM-Cl)

1 g of MCM-41 was activated by being kept at 200°C for 2 hours in order to generate an adequate amount of hydroxyl groups on its surface. The activated MCM-41 was then suspended in 30 mL of dry toluene and 1.5 mL of chloropropyltriethoxy silane (CPTES) were added. The mixture was refluxed for 12 hours under flowing nitrogen, filtered, washed with fresh toluene and air-dried at 50°C overnight.

3.2.4 Synthesis of Hexamethylenediamine-Functionalized MCM-41 (MCMHex)

1 g of MCM-Cl was suspended in dry toluene and refluxed for 12 hours under nitrogen flow in the presence of excess 1,6-hexanediamine. Then, the material was washed with methanol and air-dried at 50°C.

3.2.5 Incorporation of AuNP into MCMHex (MCMHex AuNP)

3 g of MCMHex and 180 mg of tetrachloroauric acid trihydrate ($HAuCl_4 \cdot 3H_2O$) were added to 137 mL of a 10 mM Irgacure-2959 solution and irradiated with UVA light for 45 minutes using a Luzchem LZC-4 photoreactor equipped with 14 lamps (36-70 W/m^2 for UVA lamp, $\lambda > 300$ nm, centered at 350 nm). Finally, the solid was filtered and thoroughly washed with water to remove any remaining $HAuCl_4$ and air dried overnight at 50°C to obtain the desired modified mesoporous material with Au nanoparticles anchored to the hexamethylenediamine chains.

3.2.6 Synthesis of Gold Nanorods

Au nanorods were synthesized based on a seed-mediated method reported by He *et al.*[51] Briefly, a seed solution was prepared by adding 25 μL of $HAuCl_4$ (0.1 M) to 10 mL of C_{16}TAB (0.1 M). Next, 0.6 mL of an ice-cold $NaBH_4$ aqueous solution (0.01 M) was added. The solution was stirred vigorously for 2 minutes and aged at room temperature for 45 minutes. Then, a growth solution was prepared by consecutively dissolving 3.6 g of C_{16}TAB and 0.44 g of 5-bromosalicylic acid in 100 mL of warm MilliQ water (55°C). Next, 1.92 mL of aqueous $AgNO_3$ was added and the solution was kept undisturbed for 15 minutes at room temperature to further add 100 mL of a

$HAuCl_4 \cdot 3H_2O$. Upon gentle mixing of the solution for 15 minutes, 0.512 mL of 0.1 M ascorbic acid was added with vigorous stirring for 30 seconds until the mixture became colorless. Finally, 0.32 mL seed solution was added and the mixture was stirred for 30 seconds to then incubate it at 27°C for 12 hours. The final gold nanorod solution was centrifuged at 11000 rpm for 10 minutes and re-dispersed in water.

3.2.7 Incorporation of AuNR into MCMHex (MCMHex AuNR)

100 mg of MCMHex material was suspended in 10 mL of centrifuged and re-dispersed AuNR solution and stirred at room temperature for 24 hours. Finally, the material was filtered and thoroughly washed with water and methanol and air-dried at 50°C.

3.2.8 Incorporation of AuNP and AuNR into MCMHex (MCMHex AuNPNR)

100 mg of MCMHex AuNP material was suspended in 10 mL of centrifuged and re-dispersed AuNR solution and stirred at room temperature for 24 hours. Finally, the material was filtered and thoroughly washed with water and methanol and air-dried at 50°C.

3.2.9 Naproxen Loading

0.4 g of the corresponding hybrid material was suspended in a solution containing 0.4 g of Naproxen dissolved in 15 mL of hexane and stirred 12 hours at room temperature while preventing hexane evaporation. Finally, the material was filtered and thoroughly washed with hexane and air-dried at 50°C.

3.2.10 Cucurbit[6]uril (CB6) Hydrate Loading

100 mg of the corresponding hybrid material was added to a solution of cucurbit[6]uril hydrate (100 mg) in NH_4OH buffer solution (0.01 M, pH6). The mixture was stirred 24 hours to reach loading saturation allowing the encapsulation of the grafted hexamethylenediamine tethers in the cavity of the cucurbit[6]uril (CB6) molecules. Finally, the material was filtered and thoroughly washed with NH_4OH buffer solution in order to remove any unbound CB6.

3.2.11 N-(4-aminophenyl)imidazole hydrochloride Synthesis

The guest salt was prepared by dissolving N-(4-aminophenyl)imidazole in 5 M HCl followed by crystallization after ethanol addition. The crystals were collected by filtration and dried under air.

3.2.12 Cucurbit[6]uril hydrate Release Studies

A calibration curve was constructed by preparing a batch of solutions containing a fixed amount of the imidazole hydrochloride guest (3.2 x 10^{-5}M) and increasing concentrations of CB6 in water. Next, the fluorescence spectra of these solutions were recorded on a Photon Technology International (PTI) fluorimeter. The amount of CB6 released was determined by measuring the fluorescence enhancement of N-(4-aminophenyl)imidazole hydrochloride guest upon its inclusion in the cavity of CB6. After soaking 10 mg of the material in 3 mL of SBF the samples were centrifuged and 300 μL aliquot was taken and added into a solution containing the same amount of guest used for the calibration curve. Finally, the samples were analyzed by measuring the corresponding fluorescence enhancement.

3.2.13 Naproxen Release Studies

Drug Release studies were performed by soaking 10 mg of the material in 3 mL of simulated body fluid (SBF) and the suspended mixture was irradiated with the corresponding LED light at different times. Upon centrifugation, the concentration of drug released over time was monitored by analysing the supernatant by UV-visible spectroscopy.

3.3 Results and Discussion

3.3.1 Material Characterization

Figure 3.8 shows the small angle X-ray diffraction pattern of the synthesized materials. The three distinctive x-ray diffraction peaks (100), (110) and (200), characteristic of MCM-41 materials, are preserved upon Hexanediamine (Hex) grafting and further incorporation of gold nanostructures. The presence of these peaks confirms that the 2D hexagonal mesoporous structure has been retained after functionalization.

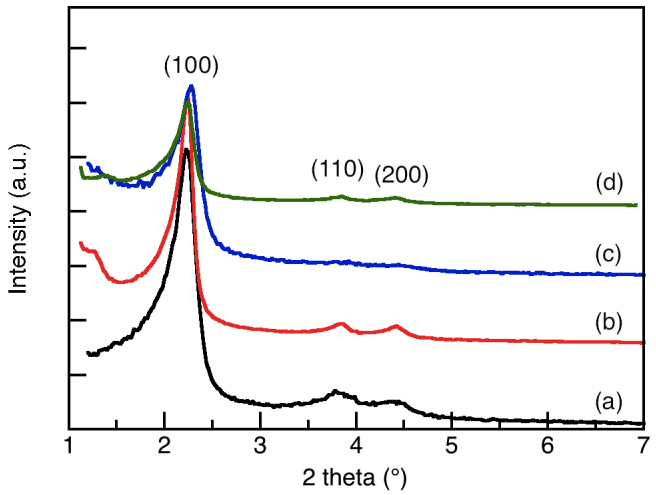

Figure 3.8: XRD patterns of hexanediamine grafted MCM-41 (MCMHex) (*a*), MCMHex after photochemical incorporation of AuNPs (MCMHex AuNP) (*b*), MCMHex upon AuNRs incorporation (MCMHex AuNR) (*c*) and MCMHex upon AuNPs and AuNRs incorporation (MCMHex AuNPNR) (*d*).

Diffuse reflectance (DR) spectra of the hybrid materials corroborate the successful incorporation of gold nanostructures. As can be seen on Figure 3.9a the MCMHex AuNP spectrum presents a single plasmon band centered at ≈ 532 nm distinctive of AuNPs. Moreover, the MCMHex AuNR spectrum shows the two characteristic transverse and longitudinal plasmon bands centered at ≈ 532 nm and ≈ 740 nm,

respectively. As expected, the DR spectrum of the hybrid material containing AuNP and AuNR presents both transverse and longitudinal bands. However, the former is more intense due to the fact that both nanostructures (AuNP and AuNR) possess a band centred at ≈ 532 nm (transverse) while only AuNR have a longitudinal resonance at around 740 nm. As a mode of comparison, Figure 3.9b shows the characteristic absorption spectrum of an aqueous solution of synthesized AuNR and its corresponding TEM micrograph. Both plasmon band maxima were preserved upon nanostructure incorporation into the mesoporous materials. The DR spectra show broader bands, which could be attributed to scattering of both the nanostructures and the silica matrix.

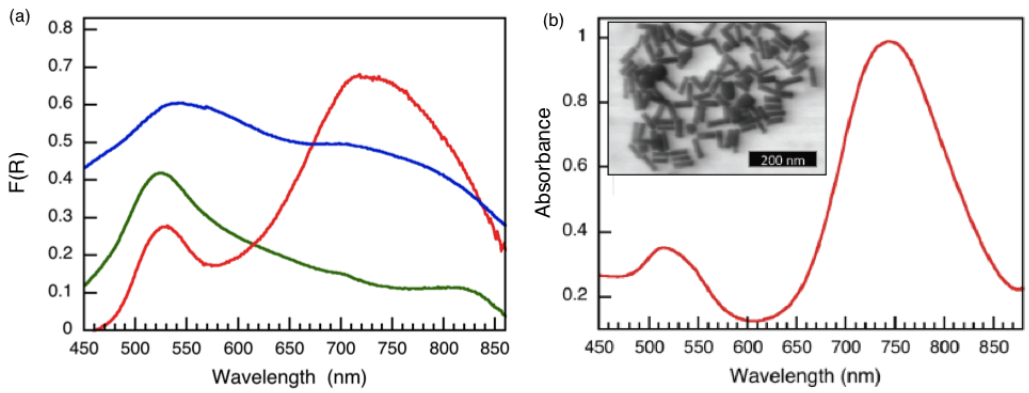

Figure 3.9: Diffuse reflectance spectra (a) of MCMHex AuNP (*Green*), MCMHex AuNR (*Red*) and MCMHex AuNPNR (*Blue*) and absorption spectrum (b) of aqueous AuNR. (inset b) TEM michrograph of synthesized AuNR.

TEM micrographs presented on Figure 3.10 further confirm the preservation of the 2D hexagonal structure of the MCM-41 based supports and the successful incorporation of the corresponding nanostructures. Upon closer inspection it was observed that the incorporation of the AuNP and AuNR in the same material is feasible without altering their original aspect ratio, shape and size (See inset 3d).

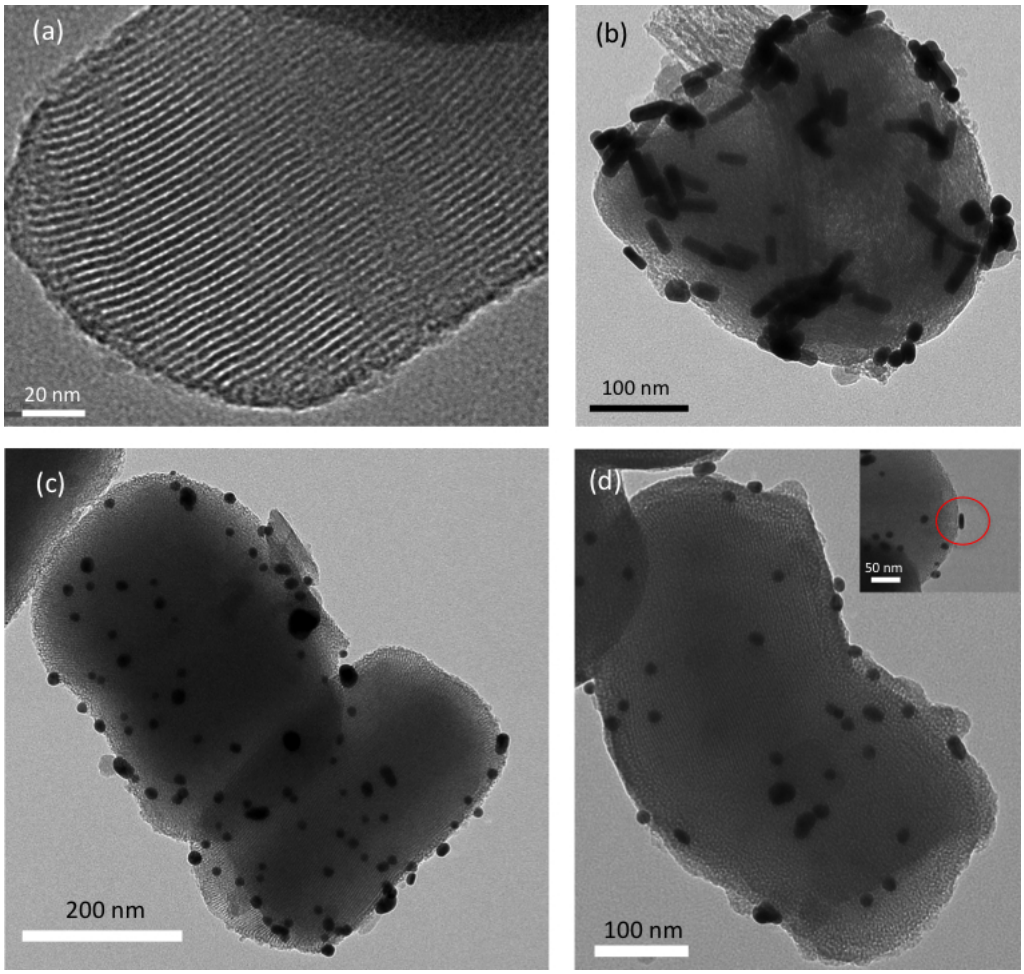

Figure 3.10: TEM micrographs of pure MCM-41 (a), MCMHex AuNR (b), MCMHex AuNP (c) MCMHex AuNPNR (d) and zoom-in showing a single AuNR attached to the surface of MCM-41 (inset d).

Metal Loading

The corresponding gold loadings for the different hybrid mesoporous materials -obtained by ICP measurements- indicated a metal loading of 2.16 %, 6.85 % and 8.03 % for MCMHex AuNP, MCMHex AuNR and MCMHex AuNPNR, respectively. MCMHex AuNP shown the lowest Au loading compared to the other two materials. Nonetheless, this value is consistent with the one obtained for MApAu-3 in Chapter 2. Using hexanediamine as an anchoring amine instead of aminopropyltriethoxy silane -as used in Chapter 2- does not seem to considerably affect the final % metal loading. It is worth noting that the synthesis of MCMHexAuNP with a higher metal loading showed to be impractical due to agglomeration at higher concentrations of gold precursor. However, a higher gold loading can be achieved by the incorporation of both AuNR and AuNP.

3.3.2 Quantification of Cucurbit[6]uril

Quantification of the cucurbit[6]uril gate upon system opening was performed utilizing the previously reported phenomenon of fluorescence enhancement of phenyl imidazole hydrochloride salts in the presence of CB6. Figure 3.11 left shows a consistent increase on the fluorescence intensity of the imidazole host in the presence of increasing concentrations of CB6 host. A calibration curve for cucurbit[6]uril was constructed based on fluorescence enhancement (F/F_o) and its linear fit was further used to determine the concentration of CB6 released in time upon system activation. It is worth clarifying that the purpose of the calibration curve was solely to quantify the amount of CB6 released in the range of concentrations used for this study -for which it demonstrated to be accurate. The CB6 water and metal ion content was considered based on the values reported by the CB6 supplier.

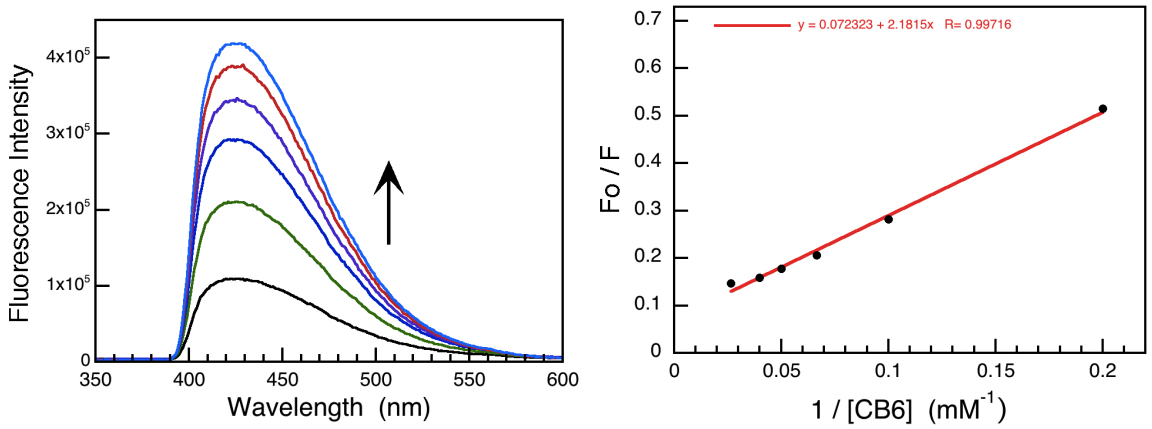

Figure 3.11: Fluorescence spectra of N-(4-aminophenyl)imidazole hydrochloride in the presence of increasing concentrations of CB6 (0.3 to 50 mM) (left) and CB6 calibration curve (right). Calibration curve associated error: ≈5%

3.3.3 Cucurbit[6]uril Release Studies

The gold nanostructure-functionalized materials were initially tested in order to assess the feasibility of using the surface plasmon heating effect to initiate cargo release by thermally disassembling the cucurbit[6]uril-hexane diamine (CB6-Hex) host-guest complex upon SPR excitation. Similar CB6 percentage loadings were obtained for each of the synthesized nanostructure-functionalized materials (See 3.12a). However, as shown in Figure 3.12b, the maximum CB6 released upon thermal disassembly of the Hex-CB6 complex varied from one material to another. A small percentage of CB6 -corresponding to remnant unbound physisorbed CB6 molecules- was released under dark conditions. In contrast, a much higher percentage CB6 was released compared to the corresponding dark condition experiments upon 5 minutes of plasmon excitation indicating the feasibility of using the plasmon heating effect in order to disassemble the CB6-Hex host-guest complex.

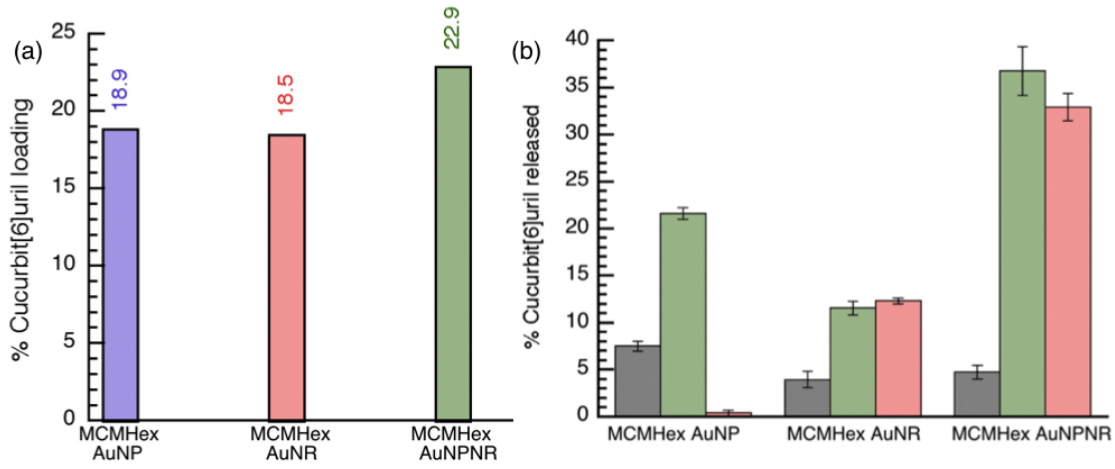

Figure 3.12: Percentage Cucurbit[6]uril loading for the different materials (a) and percentage Cucurbit[6]uril released (b) under dark (*Gray*), 532 nm light irradiation (*Green*) and 740 nm light irradiation (*Pink*). The corresponding irradiances for the 532 nm and 740 nm LEDs are 0.41 W/m^2 and 0.65 W/m^2, respectively.

Approximately 3 times more CB6 was released by SPR excitation (532 nm) when using MCMHex AuNP and MCMHex AuNR materials. A much higher percentage of cucurbituril was delivered when either the transverse or longitudinal plasmon bands of MCMHex AuNR were excited compared to its dark counterpart. Both, green and IR irradiation of the AuNR conducted to similar percentages of CB6 delivered.

The material containing both AuNP and AuNR showed the highest percentage CB6 delivered compared to the other materials. Approximately 40 % of the total CB6 loaded was delivered upon light activation. These results obtained are to be expected since the disassembly of the CB6-Hex complex is a thermally driven process.[23] Thus, the more particles whose SPR band is being excited the more molecules will be affected by an increase in local temperature achieving a higher amount of gate complexes disassembled. This would also offer an explanation to why a slightly higher %CB6 released is obtained upon green light activation of MCMHex AuNPNR compared to using red light. After all, both AuNP and AuNR posses a transverse plasmon band while only nanorods have a longitudinal one making the extent of the plasmon heating

effect greater when green light is applied. Note that there is no release upon 740 nm irradiation of MCMHex AuNP; this of course is the anticipated result, as AuNP have no absorption at this wavelength.

Due to the fact that the CB6-Hex host-guest complex is aimed to be used as gates of a closed drug delivery system that must be dismantled in order to be opened and let the cargo be released, the material that presented the highest percentage CB6 released was selected for future studies based on the premise that the more complexes disassembled the higher the probability to allow the drug to diffuse out of the system. Therefore, MCMHex AuNPNR was selected as the best candidate for further testing as drug delivery system. Figure 3.13 shows schematically the release experiment emphasizing the fact that AuNP only absorb green light, while the AuNR rods absorb both green and NIR light.

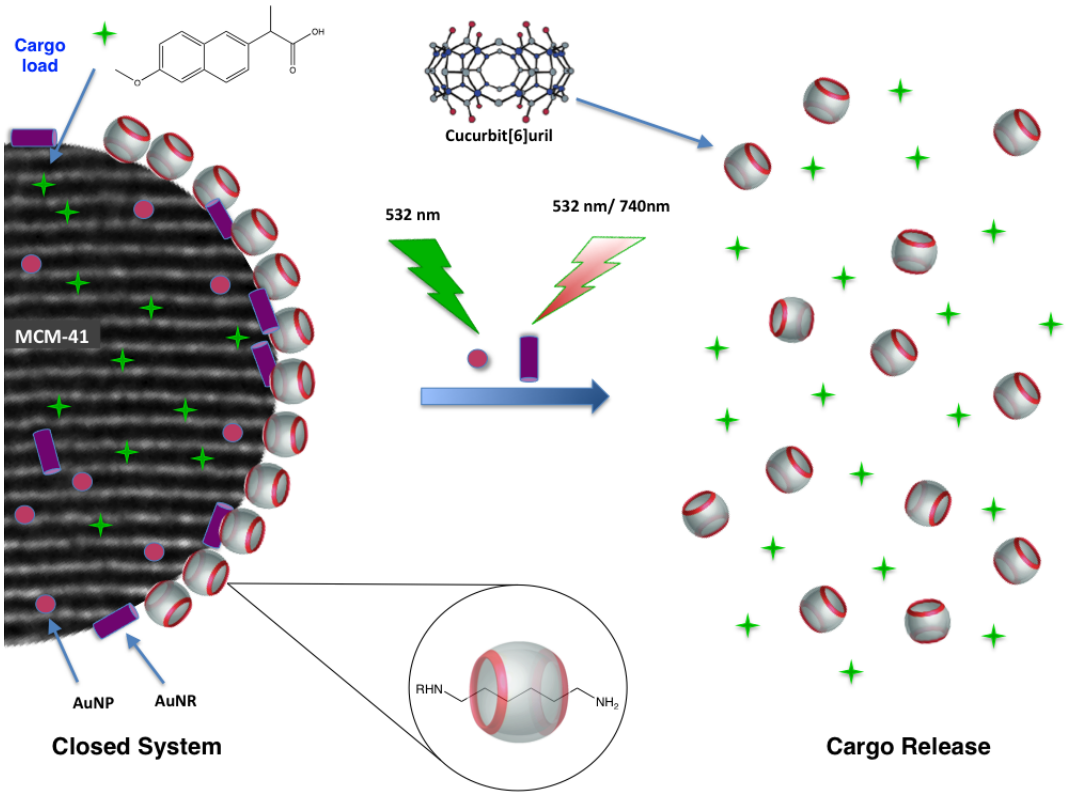

Figure 3.13: Graphical representation of the cargo release process from a closed system.

3.3.4 Naproxen Release Studies

Naproxen release curves for MCMHex AuNPNR performed in the dark as well as under different irradiation conditions can be seen on Figure 3.14. The left panel (a) corresponds to an open system in which only naproxen has been loaded and no CB6 is present while the right panel (b) corresponds to the closed system in which the CB6-Hex inclusion complex has been formed after cargo incorporation. Approximately 44 % of naproxen was released in 10 hours from the open system under dark conditions. Nevertheless, when the CB6-Hex complex has been formed to close the system little to none naproxen was released.

These results highlight the viability of using the CB6-Hex complex as a gate in order to effectively obtain near "zero" premature release by closing the system allowing the cargo drug to be encapsulated inside the material.

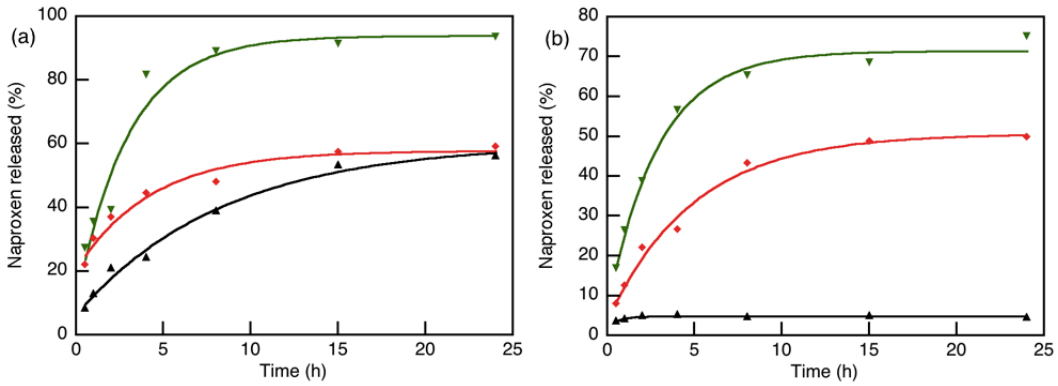

Figure 3.14: Percent naproxen released curves over time for MCMHex AuNPNR without CB6 (a) and with CB6 (b). Black curves represent experiments performed under dark conditions, red curves represent release under continuous 740 nm LED irradiation and green curves represent experiments performed under 532 nm green light LED irradiation. Note: The curves shown are simply a guide to the eye and do not represent a mathematical fit.

A similar % Naproxen delivered was observed when comparing the release curves of the open system activated by IR irradiation and under dark conditions. However, it is possible to see that the initial rate of release is higher when the longitudinal plasmon band of the AuNR is excited using 740 nm light than when performed under dark conditions. In spite of the fact that the irradiance of the 740 nm LED (0.65 W/m^2) is higher than the 532 nm light source (0.41 W/m^2), a more drastic effect is observed when the system is activated using 532 nm light and close to 100 % of the naproxen is released; see Figure 3.15 for the corresponding LED irradiance spectra.

These results could be anticipated since both AuNP and AuNR possess a plasmon band centered around 532 nm. Hence, when irradiating the system at the corresponding wavelength the transverse plasmon band of AuNR as well as the single SPR band of AuNP are being excited, thus increasing the probability of having a greater number

of areas reaching high local temperatures and enhancing drug diffusion.

In addition, only the AuNPs -synthesized *in situ*- can be located in the mesopores making the plasmon heating effect induced by 532 nm irradiation able to reach molecules located in regions inside of the mesoporous matrix; these regions are unreachable by AuNR excitation, as they are located exclusively on the external surface of MCM-41.

In the case of the closed system (Figure 3.14b), an analogous phenomenon was observed. As mentioned before, a higher percentage of the drug was released when the system was activated by green or IR light irradiation. The release performed from a closed system reached a lower final % cargo delivered compared to its open homologous system. This could be explained by the possibility that not all the pores of the material were open since the nanostructures and the CB6-Hex complex must be close enough for the plasmon heating to be effective and dismantle it.

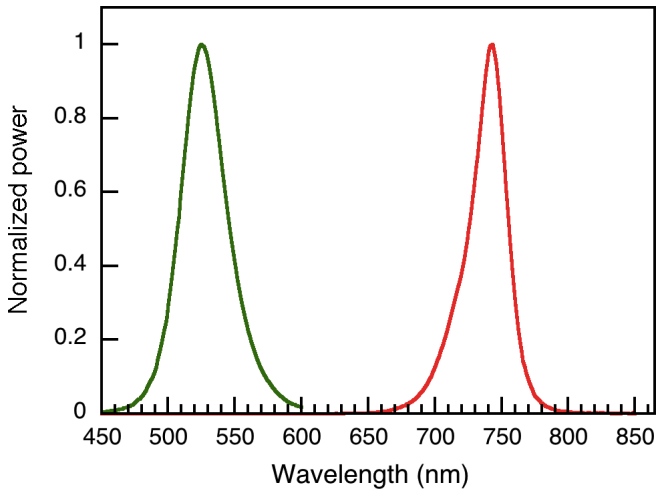

Figure 3.15: Irradiance spectra of 532 nm (*Green*) and 740 nm (*Red*) LED, respectively.

Figure 3.16 shows consecutive naproxen releases from MCMHex AuNPNR under different experimental conditions. Initially the loaded material was kept under dark conditions for the first 4 hours in order to confirm that the system is effectively closed. Then, 740 nm LED irradiation was applied opening the system and letting the cargo to be delivered following a similar trend to that previously observed under these conditions. After 15 hours of red light irradiation, approximately at the time the naproxen release curve usually reaches a plateau, the LED source was changed to 532 nm.

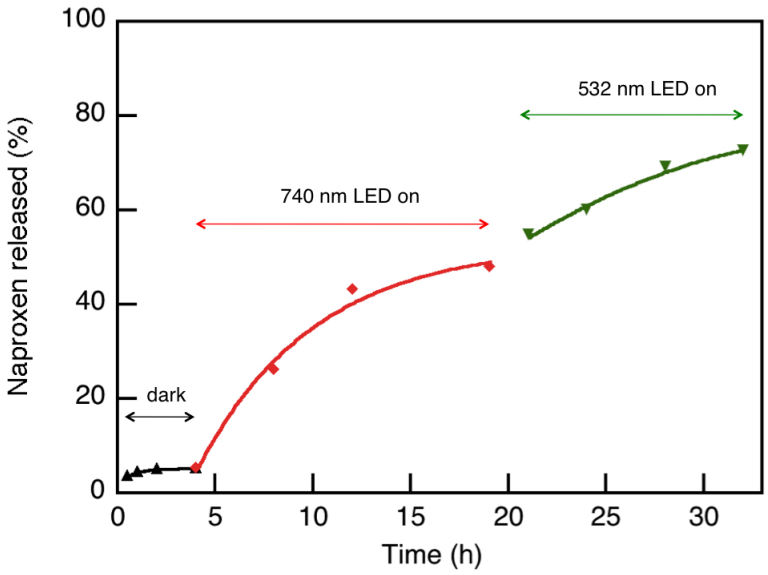

Figure 3.16: Percent naproxen released curves for MCMHex AuNPNR in dark conditions (***Black***) followed by 740 nm (*Red*) and 532 nm (*Green*) LED irradiation, respectively. Under prolonged exposure the release reaches a plateau at 73 %. Note: The curves shown are simply a guide to the eye and do not represent a mathematical fit.

A second release trend was generated under green light irradiation reaching a second and final plateau after 13 hours. As observed, two different rates of release can be obtained by either exciting the longitudinal plasmon band of AuNR or the transverse SPR band of both AuNP and AuNR. The additional rate of release ob-

tained compared to previously designed hybrid mesoporous materials contributes to the versatility of the system by having an extra activation component as well as expanding its applicability due to the fact that the longitudinal plasmon band of AuNR is located at the optimum wavelength range for biological tissue penetration.[52]

3.4 Conclusions

When metal nanoparticles are embedded in supramolecular structures such as MCM-41 the heat released to the medium influences the guests and solvents contained within the channels of the mesoporous material.[53]

In this chapter, several hybrid mesoporous systems were designed. The successful incorporation of a thermoresponsive gate based on the CB6-Hex host-guest complex conferred the system with the so desired "zero" premature release. This feature combined with the incorporation of gold nanorods and gold nanoparticles capable of acting as a heat source when their SPR bands are excited by light allowed to obtain a cargo release system active to green and IR light. These findings show it is feasible to use the surface plasmon heating effect to control both the starting point of the cargo release as well as the rates of delivery.

The results obtained prove it is possible to disassemble the Cucurbit[6]uril-hexane diamine gate complex by using 5 minutes of either green or IR irradiation to activate the system and start the release. By means of gold nanorods the NIR light activation component was incorporated into the systems generating an extra rate of release besides the ones promoted by dark and green light irradiation conditions. The above findings expand the versatility of these types of systems by achieving three different rates of release as well as increasing its applicability by allowing the use of the drug delivery system in biological samples that would require deeper light penetration.

REFERENCES

[1] J Zhou, N Hao, M Yan, and O Ramstrom. Lectin-gated, mesoporous, photofunctionalized glyconanoparticles for glutathione-responsive drug delivery. *Chemical Communications*, 51:9833–9836, 2015.

[2] X Huang, S Wu, and X Du. Gated mesoporous carbon nanoparticles as drug delivery system for stimuli-responsive controlled release. *Carbon 101*, 1:135–142, 2016.

[3] H Huang, G Liu, H Gao, and Y Wang. A pH-responsive drug delivery system with an aggregation-induced emission feature for cell imaging and intracellular drug delivery. *Polymer Chemistry*, 6:4715–4718, 2015.

[4] D Needham and MW Dewhirst. The development and testing of a new temperature-sensitive drug delivery system for the treatment of solid tumors. *Advanced Drug Delivery Reviews*, 53:285–305, 2001.

[5] SD Fitzpatrick, LE Fitzpatrick, A Thakur, MAJ Mazumder, and H Sheardown. Themperature-sensitive polymers for drug delivery. *Expert Review of Medical Devices*, 9(4):339–351, 2012.

[6] P Saint-Cricq, S Deshayes, JI Zink, and AM Kasko. Magnetic field activated drug delivery using thermodegradable azo-functionalized PEG-coated coreshell mesoporous silica nanoparticles. *Nanoscale*, 7(4):13168–13172, 2015.

[7] VV Mody, A Cox, S Shah, A Singh, W Bevins, and H Parihar. Magnetic nanoparticle drug delivery systems for targeting tumor. *Applied Nanoscience*, 4(4):385–392, 2014.

[8] NK Mal, M Fujiwara, and Y Tanaka. Photocontrolled reversible release of guest molecules from coumarin-modified mesoporous silica. *Nature*, 421:350–353, 2003.

[9] S Kumara, R Kumara, A Ratnama, NC Mishrab, and K Ghosha. Novel drug delivery system for photoinduced nitric oxide (NO) delivery. *Inorganic Chemistry Communications*, 53:23–25, 2015.

[10] S Mura, J Nicolas, and P Couvreur. Stimuli responsive nanocarriers for drug delivery. *Nature Materials*, 12:991–1003, 2003.

[11] II Slowing, JL Vivero-Escoto, CW Wu, and VSY Lin. Mesoporous silica nanoparticles as controlled release drug delivery and gene transfection carriers. *Advanced Drug Delivery Reviews*, 60(11):1278–1288, 2008.

[12] C Chen, J Geng, F Pu, X Yang, J Ren, and X Qu. Polyvalent nucleic acid/mesoporous silica nanoparticle conjugates: Dual stimuli-responsive vehicles for intracellular drug delivery. *Angewandte Chemie International Edition*, 50(4):882–886, 2011.

[13] X Du. *Biomacromolecule-Gated Mesoporous Silica Drug Delivery Systems for Stimuli-Responsive Controlled Release in Advanced Theranostic Materials*. Advanced Materials Series. Wiley-Scrivener Publishing, 2015.

[14] NK Mal, M Fujiwara, Y Tanaka, T Taguchi, and M Matsukata. Photo-switched storage and release of guest molecules in the pore void of coumarin-modified MCM-41. *Chemistry of Materials*, 15:3385–3394, 2003.

[15] JL Paris, MV Cabanas, M Manzano, and M Vallet-Regí. Polymer-grafted mesoporous silica nanoparticles as ultrasound-responsive drug carriers. *ACS Nano*, 9(11):11023–11033, 2015.

[16] S Giri, BG Trewyn, MP Stellmaker, and VS Lin. Stimuli-responsive controlled-release delivery system based on mesoporous silica nanorods capped with magnetic nanoparticles. *Angewandte Chemie International Edition*, 44:5038–5044, 2005.

[17] J Liu, X Du, and X Zhang. Enzyme-inspired controlled release of cucurbit[7]uril nanovalves by using magnetic mesoporous silica. *Chemististry European Journal*, 17(3):810–815, 2011.

[18] J Liu and X Du. pH- and competitor-driven nanovalves of cucurbit[7]uril rotaxanes based on mesoporous silica supports for controlled release. *Journal of Materials Chemistry*, 20:3642–3649, 2010.

[19] NM Khashab, A Tranolsi, YA Lau, MW Ambrogio, DC Friedman, HA Khatib, JI Zink, and JF Stoddart. Redox- and pH-controlled mechanized nanoparticles. *European Journal of Organic Chemistry*, (11):1669–1673, 2009.

[20] S Angelos, YW Yang ans K Platel, JF Stoddart, and JI Zink. pH-responsive supramolecular nanovalves based on cucurbit[6]uril pseudorotaxanes. *Angewandte Chemie International Edition*, 47(12):2222–2226, 2008.

[21] S Angelos, YW Yang ans K Platel, JF Stoddart, and JI Zink. pH Clock-operated mechanized nanoparticles. *The Journal of the American Chemical Society*, 131(36):12912–12914, 2009.

[22] MW Ambrogio, TA Pecorelli, K Platel, NM Khashab, A Trabolsi, HA Khatib,

YY Botros, JI Zink, and JF Stoddart. Snap-top nanocarriers. *Organic Letters*, 12(15):3304–3307, 2010.

[23] CR Thomas, DP Ferris, JH Lee, E Choi, MH Cho, ES Kim, JF Stoddart, JS Shin, and JI Zink. Noninvasive remote-control release of drug molecules in vitro using magnetic actuation of mechanized nanoparticles. *The Journal of the American Chemical Society*, 132(31):10623–10625, 2010.

[24] JW Lee, S Samal, N Selvapalam, HJ Kim, and K Kim. Cucurbituril homologues and derivatives: New opportunities in supramolecular chemistry. *Accounts of Chemical Research*, 36(8):621–630, 2003.

[25] M Freitaga and E Galoppini. Molecular host-guest complexes: Shielding of guests on semiconductor surfaces. *Energy Environmental Science*, 4:2482–2494, 2011.

[26] WA Freeman, WL Mock, and NY Shih. Cucurbituril. *Journal of the American Chemical Society*, 103(24):7367–7368, 1981.

[27] J Kim, IS Jung, SY Kim, E Lee, JK Kang, S Sakamoto, K Yamaguchi, and K Kim. New cucurbituril homologues: Syntheses, isolation, characterization, and x-ray crystal structures of cucurbit[n]uril (n = 5, 7, and 8). *Journal of the American Chemical Society*, 122(3):540–541, 2000.

[28] AI Day, AP Arnold, JB Blanch, and B Snushall. Controlling factors in the synthesis of cucurbituril and its homologues. *Journal of Organic Chemistry*, 66(24):8094–8100, 2001.

[29] AI Day, JB Blanch, AP Arnold, GR Lewis, and I Dance. A cucurbituril-based gyroscane: A new supramolecular form. *Angewandte Chemie International Edition*, 41(2):275–277, 2002.

[30] WM Nau, M Florea, and KI Assaf. Deep inside cucurbiturils: Physical properties and volumes of their inner cavity determine the hydrophobic driving force for host-guest complexation. *Israel Journal of Chemistry*, 51:559–577, 2011.

[31] WL Mock and NY Shih. Structure and selectivity in host-guest complexes of cucurbituril. *The Journal of Organic Chemistry*, 51:4440–4446, 2011.

[32] C Marquez and WM Nau. Two mechanisms of slow host-guest complexation between cucurbit[6]uril and cyclohexylamine: pH-Responsive supramolecular kinetics. *Angewandte Chemie International Edition*, 40(17):3155–3160, 2001.

[33] C Marquez and RR Hudgins WM Nau. Mechanism of host-guest complexation by cucurbituril. *Journal of the American Chemical Society*, 126(18):5806–5816, 2004.

[34] X Ling, EL Samuel, DL Patchell, and E Masson. Cucurbituril slippage: Translation is a complex motion. *Organic Letters*, 12(12):2730–2733, 2010.

[35] KN Houk, AG Leach, SP Kim, and X Zhang. Binding affinities of host-guest, protein-ligand and protein-transition-state complexes. *Angewandte Chemie International Edition*, 42:4872–4897, 2003.

[36] J Lagona, P Mukhopadhyay, S Chakrabarti, and L Isaacs. The cucurbit[n]uril family. *Angewandte Chemie International Edition*, 44(31):4844–4870, 2005.

[37] F Biedermann, VD Uzunova, OA Scherman, WM Nau, and A De Simone. Release of high-energy water as an essential driving force for high-affinity binding of cucurbit[n]urils. *The Journal of the American Chemical Society*, 134(18):15318–15323, 2012.

[38] CF Li, LM Du, and HM Zhang. Study on the inclusion interaction of cucurbit[n]urils with sanguinarine by spectrofluorimetry and its analytical application. *Spectrochimica Acta Part A: Molecular and Biomolecular Spectroscopy*, 75:912–917, 2010.

[39] CF Li, LM Du, and WYWu ans AZ Sheng. Supramolecular interaction of cucurbit[n]urils and coptisine by spectrofluorimetry and its analytical application. *Talanta*, 80:1939–1944, 2010.

[40] M Del Pozo, L Hernández, and C Quintana. A selective spectroflurimetric method for carbendazim determination in oranges involving inclusion-complex formation with cucurbit[7]uril. *Talanta*, 81:1542–1546, 2010.

[41] Y Huang, J Wang, SF Sue, Z Tao, QJ Zhu, and Q Tang. Determination of thiabendazole in aqueous solutions using a cucurbituril-enhanced fluorescence method. *The Journal of Inclusion Phenomena and Macrocyclic Chemistry*, 72:397–404, 2012.

[42] F Yao, H Liu, G Wang, L Du, X Yin, and Y Fu. Determination of paraquat in water samples using a sensitive fluorescent probe titration method. *Journal of Environmental Sciences*, 25:1245–1251, 2013.

[43] BD Wagner, JS Fitzpatrick, MA Gill, AI MacRae, and N Stojanovic. A fluorescent host-guest complex of cucurbituril in solution: A molecular Jack O'lantern. *Canadian Journal of Chemistry*, 79:1001–1004, 2001.

[44] Y Feng, SF Xue, ZF Fan, YQ Zhang, QJ Zhu, and Z Tao. Host-guest complexes of some cucurbit[n]urils with hydrochloride salts of some imidazole derivatives. *The Journal of Inclusion Phenomena and Macrocyclic Chemistry*, 64:121–131, 2009.

[45] VD Uzunova, C Cullinane, K Brix, WM Nau, and AI Day. Toxicity of cucurbit[7]uril and cucurbit[8]uril: an exploratory in vitro and in vivo study. *Organic Biomolecular Chemistry*, 9:2037–2042, 2010.

[46] G Hettiarachchi, D Nguyen, J Wu, D Lucas, D Ma, L Isaacs, and V Briken. Toxicology and drug delivery by cucurbit[n]uril type molecular containers. *PLoS ONE*, 5:e10514, 2010.

[47] YT Chang, PY Liao, HS Sheu, YJ Tseng, FY Cheng, and CS Yeh. Near-infrared light-responsive intracellular drug and siRNA release using Au nanoensembles with oligonucleotide-capped silica shell. *Advanced Materials*, 24:3309–3314, 2012.

[48] J Croissant and JI Zink. Nanovalve-controlled cargo release activated by plasmonic heating. *Journal of the American Chemical Society*, 134:7628–7631, 2012.

[49] H Li, LL Tan, P Jia, QL Li, YL Sun, J Zhang, YQ Ning, J Yu, and YW Yang. Near-infrared light-responsive supramolecular nanovalve based on mesoporous silica-coated gold nanorods. *Chemical Science*, 5:2804–2808, 2014.

[50] P Kubelka. New contributions to the optics of intensely light-scattering materials. *The Journal of the Optical Society of America*, 38(5):448–457, 1948.

[51] Z Zheng, T Tachikawa, and T Majima. Single-particle study of Pt-modified Au nanorods for plasmon-enhanced hydrogen generation in visible to near-infrared region. *Journal of the American Chemical Society*, 136(19):6870–6873, 2014.

[52] KC Smith. The photobiological basis of low level laser radiation therapy. *Laser Therapy*, 3(19):19–24, 1991.

[53] DT Marquez, AI Carrillo, and JC Scaiano. Plasmon excitation of supported

gold nanoparticles can control molecular release from supramolecular systems. *Langmuir*, 29:10521–10528, 2013.

Chapter 4

Plasmon Induced Self-Assembly of Gold Nanorods in Polymer Films

4.1 Gold Nanorods

Since the invention of the J Sheet Polarizer in the early 1930's the polarization effects have proven to be a useful method for modulating the optical response of light interacting with materials. Numerous attempts have been made with the aim to obtain large polymer films with polarization properties that can be used as filters and signal modulators for optical devices.

Metallic gold nanorods possess remarkable properties such as high absorption coefficients, optical tunability and resistance to photochemical corrosion which promote them as an interesting alternative to conventional organic polarizers, whose shelf life is greatly affected by the factors mentioned above. The development of surfactant-templated [1, 2, 3] and matrix[4] based synthetic approaches to obtain anisotropic metallic nanostructures has opened the door for new research topics and applications.[5, 6, 7] Nonetheless, the stumbling block between the synthesis of metal nanorods and their implementation into practical devices is their organization within solid matrices.

Considerable efforts have been invested towards the generation of spatially organized structures, plasmon coupling between nanostructures and the development of applications oriented towards information transmission, plasmonic sensing and patterning.[8] Polymers are suitable matrices for the formation of AuNR nanocomposites. Furthermore, it has been demonstrated that the alignment of these nanostructures is achievable by the stretching of the nanocomposite films and this method has become the number one method for nanorod alignment in polymeric matrices.[9, 10, 11] However, other alternatives remain to be discovered.

4.2 About this Chapter

The possibility to directly align AuNR embedded in a polymeric matrix without the need of stretching the films was explored in this chapter. Various AuNR/polymer nanocomposites were synthesized and then subjected to light irradiation with the aim to excite either the transverse or longitudinal plasmon band in order to test the surface plasmon heating effect as a tool for the direct alignment of these anisotropic nanostrucures in polymeric matrices. Two types of gold nanorods were tested, with longitudinal plasmon bands $\geq$ 640 nm and aspect ratios (AR) of $\approx$ 3 and $\approx$ 4.5.

Initially, the study was conducted using crosslinked and non crosslinked SU-8 photoresist as a polymeric matrix. Upon success, other polymers such as polymethyl metacrylate (PMMA) and silicone (PDMS) were tested. As can be seen in Figure 4.1, SU-8 is an epoxy based photoresist and -as its name indicates- it is composed of an average of 8 epoxy groups per moiety. This photoresist has been designed for the preparation of thick, chemically and thermally stable images often used in micromachining, microelectronic, photolithography, microfluidics fabrications and biological applications.[12, 13, 14] Several advantages are associated with this polymeric resin, namely, high transparency, good adhesion, fast drying, near UV processing and good biocompatibility.[15]

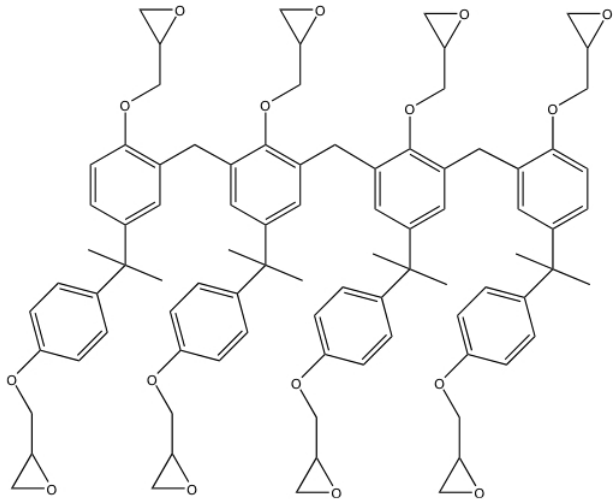

Figure 4.1: Molecular structure of SU-8 photoresist.

4.3 Experimental

4.3.1 Reagents

Gold (III) tetrachloroauric acid trihydrate ($HAuCl_4 \cdot 3H_2O$, 99.99 %), cetyltrimethyl ammonium bromide (C_{16}TAB, 96 %), sodium borohydride ($NaBH_4$, 99 %), silver nitrate ($AgNO_3$, >99 %), tetraoctylammonium bromide (TOAB) and Ascorbic acid (99 %) were purchased from Sigma-Aldrich and used without further purification. Aqueous solutions were prepared using 18.2 $M\Omega cm^{-1}$ Milli-Q water obtained from a Millipore system equipped with a 0.22 μm filter. SU-8 photoresist solution was purchased from MicroChem.

4.3.2 Instrumentation

Scanning Electron Microscopy

SEM images were recorded using a JSM-7500F field emission scanning electron microscope from JEOL Ltd.

UV-visible spectroscopy

UV-visible spectra were recorded using a Cary-100 UV-visible spectrophotometer.

Laser Irradiation Studies

Crosslinked and non-crosslinked films were irradiated using a Continnum Surelite SL-II-10 Nd:YAG pump laser with 355 nm third harmonic (≈6 ns); 690 nm and 740 nm pulses were generated by a Continnum Optical Parametric Oscillator, model SLOPO Plus (≈6 ns).

Light Emitting Diode Crosslinking

Crosslinked films were obtained by irradiating each non crosslinked layer under 400 nm LED irradiation (≈2.1 W) for 3 minutes.

4.3.3 Synthesis of Gold Nanorods

Au nanorods were synthesized based on a seed-mediated method reported by He *et al.*[16] Briefly, a seed solution was prepared by adding 100 μL of $HAuCl_4 \cdot 3H_2O$ (24 mM) to 7.5 mL of CTAB (0.1 M) and diluting to 9.4 mL. Next, 0.6 mL of an ice-cold $NaBH_4$ aqueous solution (0.01 M) was added while stirring for a couple of minutes. The solution was kept undisturbed for 45 minutes.

Next, a growth solution was prepared by consecutively adding 2.04 mL of $HAuCl_4$ (24 mM), 2 mL H_2SO_4 (0.5 M), 0.4 mL of $AgNO_3$ (10 mM) and 0.8 mL of ascorbic acid (0.1 M) into a 100 mL CTAB solution (0.1 M). Finally, 240 μL of seed solution were added into the growth solution while stirring and then the mixture was kept undisturbed for 19 h. Excess of surfactant was removed by centrifugation (12000 rpm, 10 min) and further redispersion of the AuNR in 100 mL of water.

Longer rods with an aspect ratio of 4.5 were prepared following the procedure stated on Chapter 2 and 3 of this thesis.[17]

4.3.4 Extraction of Gold Nanorods into Organic Solvents

Mercaptosuccinic acid (1 mL, 10 mM, pH 8-9) was mixed with 1 mL of centrifuged and redispersed AuNR aqueous solution. Then, 0.5 mL of TOAB in the desired organic solvent (50 mM) were added and shaken vigorously during 3 minutes. Upon separation the aqueous phase was removed achieving a AuNR organic solution.

4.3.5 Films Formation

Typically, 1 mL of SU-8 and 1.5 mL of AuNR (AR=3) in chloroform solution were mixed in a test tube and let sit for 12 hours. Then, the solutions were casted on microscope slides to form a thin layer and pre-baked at 65°C for 5 min and 95°C for 3 minutes. This procedure was repeated several times in order to achieve thicker non-crosslinked films.

Crosslinked films were obtained by irradiating each non-crosslinked layer under 400 nm LED irradiation (≈2.1W) for 3 minutes.

4.4 Results and Discussion

4.4.1 Gold Nanorods: Extraction and Optical Properties

Figure 4.2 illustrates the optical properties of the colloidal AuNRs used in this study. Their corresponding absorption spectra (Figure 4.2b) display the characteristic transverse plasmon band centered at approximately 532 nm as well as a longitudinal plasmon band centered at ≈ 650 nm and ≈ 750 nm for short AuNRs (AR = 3) and long AuNRs (AR = 4.5), respectively.

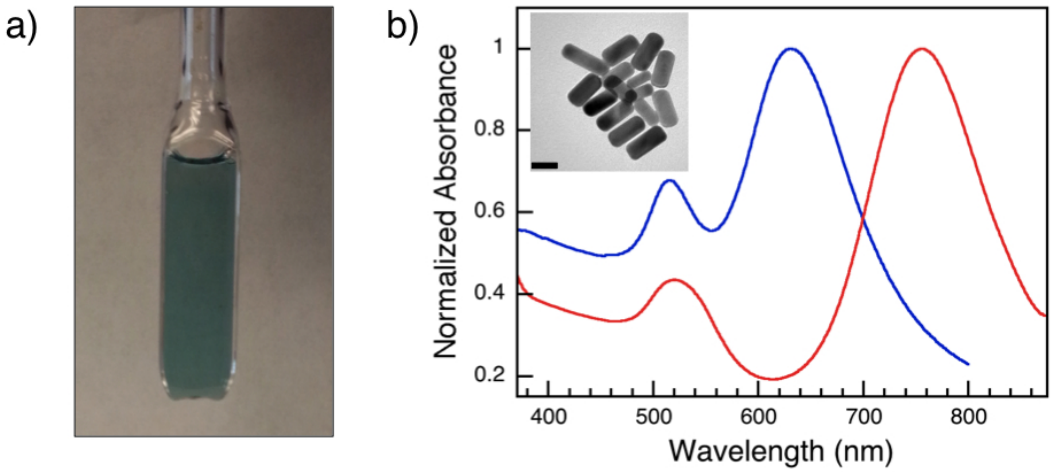

Figure 4.2: (a) Characteristic color of an aqueous AuNR (AR = 3) solution and (b) Absorption spectra of aqueous AuNR solutions of AR = 3 (*Blue*) and AR = 4.5 (*Red*). (inset) TEM image of AuNRs (AR = 3); scale bar = 20 nm.

As discussed in Chapter 1, the characteristic color of a AuNR solution is dependent on the aspect ratio of the suspended nanostructures. Figure 4.2a shows the characteristic blue color of an aqueous solution of short AuNRs which is consistent with the position of the longitudinal SPR band seen on the corresponding absorption spectrum. Similar results were obtained for the longer gold nanorods whose aqueous solution exhibited a red color attributed mainly to the sole contribution of the

transverse SPR band due to the fact that the longitudinal band falls into the infrared spectral region. A TEM image of the longer AuNRs can be seen on Figure 3.9 of this thesis.

In order to form nanocomposite films, the nanostructures were first transferred -by extraction- into an organic solvent compatible with the polymer cast solution. Initially, mercaptosuccinic acid (MSA) was added to the AuNR aqueous solution with the purpose of replacing the original surfactant (CTAB) and obtain gold nanorods capped with negatively-charged MSA molecules on the surface. Then, this solution was extracted using a solution of TOAB in either toluene or chloroform to allow the gradual transference of the MSA-capped AuNR into the organic solvent driven by the interaction between MSA and TOAB molecules.

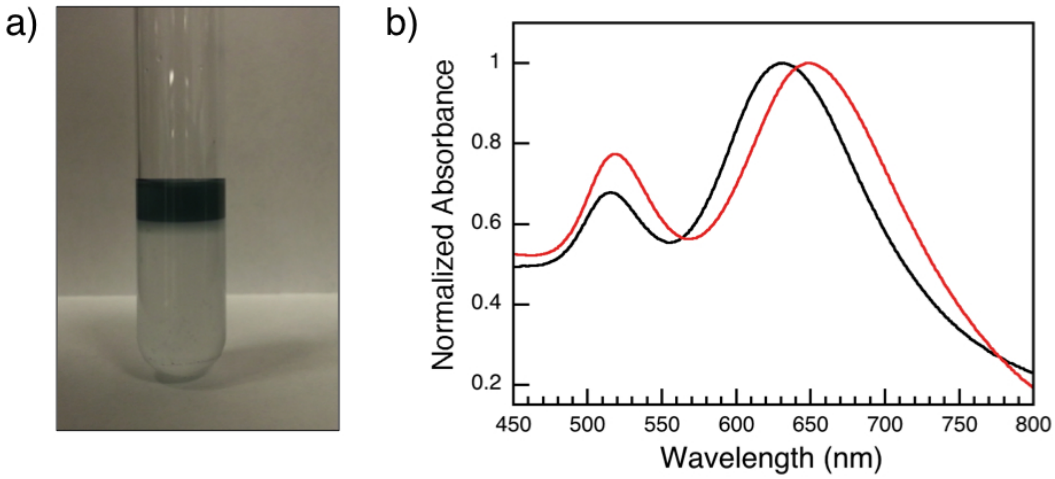

Figure 4.3: (a) Transference of AuNRs into organic solvents. Top layer: toluene; Bottom layer: water. (b) Absorption spectra of AuNRs of AR = 3 in toluene (*Red*) and water (***Black***).

Successful AuNRs transference is depicted in Figure 4.3a in which the nanostructures have been extracted from the aqueous phase (bottom) using toluene (top) as the organic phase. As expected, a red shift in the absorption spectrum -Figure 4.3b- was observed only for the LSPR band which can be attributed to the higher sensitivity of the LSPR to changes in the surrounding media.

4.4.2 AuNR/SU-8 Films

LSPR Excitation

The evolution of the absorption spectra at different irradiation times of a non-crosslinked film containing AuNRs with an aspect ratio of 3 is shown in Figure 4.4 left. As can be seen, when the film is subjected to 690 nm laser pulses the longitudinal SPR band intensity decreases accompanied by a simultaneous increase in the transverse SPR band, predominantly within the first minute of irradiation.

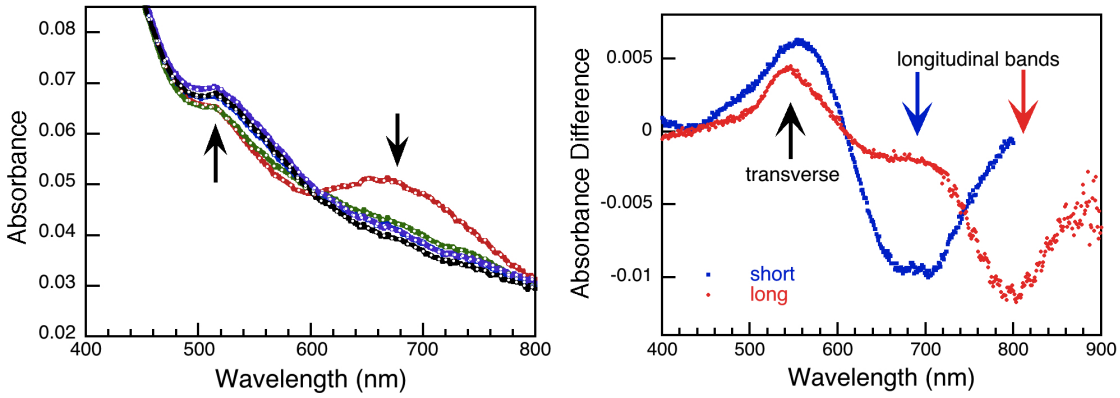

Figure 4.4: Left: Absorption spectra at different irradiation times. Initial film (*Red*), 30 seconds (*Green*), 110 seconds (*Blue*), 290 seconds (*Purple*) and 530 seconds (***Black***). Right: Change in absorption intensity at each wavelength after 290 seconds of 690 nm irradiation for AuNRs with aspect ratios of 3 (*short*) and 4.5 (*long*).

A difference spectrum showing the change in absorbance intensities at different monitored wavelengths at the end of the irradiation period characterizes the observed phenomenon. The corresponding difference spectra for AuNRs of average aspect ratios of 3 and 4.5 (Figure 4.4, right) exhibit the mentioned increase and decrease in intensities of both transverse and longitudinal plasmon band regions upon irradiation.

An equivalent phenomenon was observed for fully crosslinked films (Figure 4.5) indicating independence from the degree of crosslinking of the polymer film.

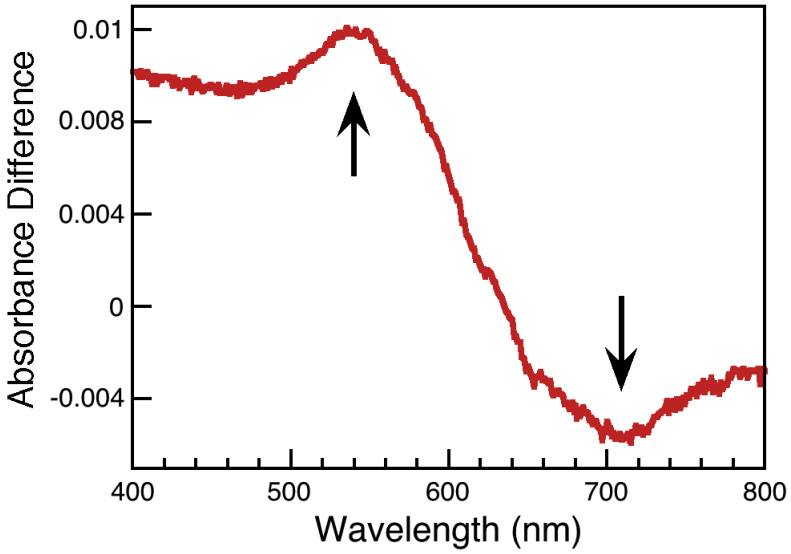

Figure 4.5: Change in absorbance of a crosslinked film at each wavelength after 290 seconds of 690 nm irradiation (SU-8, AuNRs of AR = 3.

The behavior observed can be explained based on the selective orientation of AuNRs *via* plasmon heating effect. As mentioned in Chapter 1, the literature presents several experiments utilizing the plasmon heating effect of metallic nanoparticles. Moreover, experiments performed using colloidal gold nanoparticles have suggested that temperatures well above 500°C can be achieved when irradiated with 532 nm light.[18] On the other hand, glass transition temperatures for SU-8 have been reported to be $\approx$ 50°C and $\approx$ 200°C for non-crosslinked and fully crosslinked SU-8

photoresists, respectively.[19, 20]

Initially, the AuNRs are randomly oriented in the polymer matrix. Thus, when excited by light, the absorption on the transverse and longitudinal regions will depend on the orientation of each individual particle with respect to the incident light direction. When the particle is oriented so as to absorb the 690 nm light (i.e., longitudinal SPR), the absorption leads to heat generation[18] in the immediate vicinity of the particle, softening the polymer; the AuNR moves randomly and if it accidentally aligns itself so as to appear transparent at 690 nm it will lock in that position for the simple reason that the polymer will no longer be subjected to thermal softening. A rod that does not align spontaneously will have another chance of absorbing light, potentially achieving the required alignment. This stochastic process eventually causes all the particles to align in the exposed region. Naturally, a particle that becomes effectively "transparent" at 690 nm has also oriented itself to favour 532 nm absorption (transverse SPR) -situation reflected in any of the difference spectra presented above.

TSPR Excitation

Transverse plasmon band excitation *via* 532 nm irradiation proved to be unsuccessful in orienting AuNRs. Only minor changes could be observed when the TSPR was excited (see Fig.4.6) which may reflect that a smaller volume of the polymer is softened, or the fact that the longitudinal band for AuNRs or interparticle interactions may cause some absorption in the green region [21, 22, 23, 24] restricting the mobility of the nanostructures and hence their alignment.

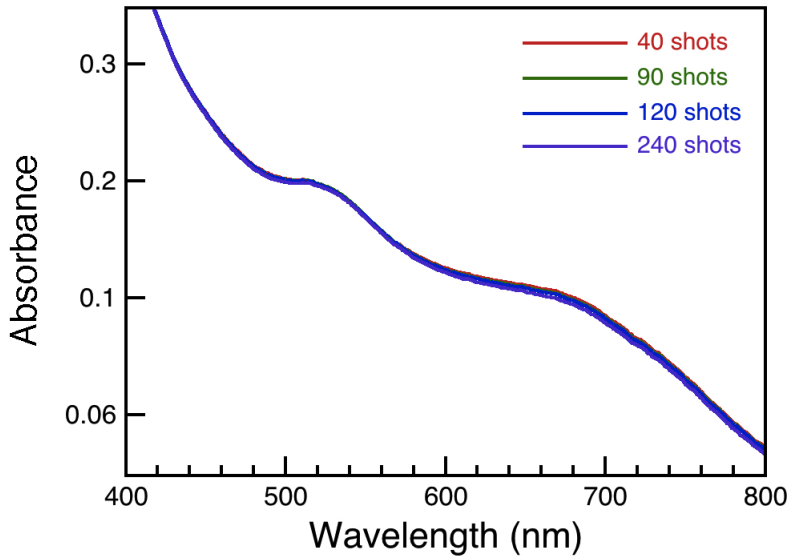

Figure 4.6: Absorption spectra at different irradiation times (532 nm). Initial film (*Red*), 90 seconds (*Green*), 120 seconds (*Blue*) and 240 seconds (*Purple*). Complete overlap of the spectra prevents detailed observation of individual traces. Polymer SU-8, AR = 3.

Ruling out Ablation

It has been previously reported that 532 nm laser irradiation can lead to ablation of gold nanoparticles.[25] In this process, polymorph and polydisperse gold nanostructures are converted predominantly into spherical AuNPs with their characteristic red color and absorption at around 530 nm.

Conceivably, a decrease in intensity of the LSPR band together with an increase on TSPR absorption could also be explained by invoking ablation of AuNRs leading to spherical AuNPs. In order to examine this possibility, irradiated non-crosslinked films were carefully dissolved in chloroform and SEM images were taken along with the corresponding UV-vis spectra.

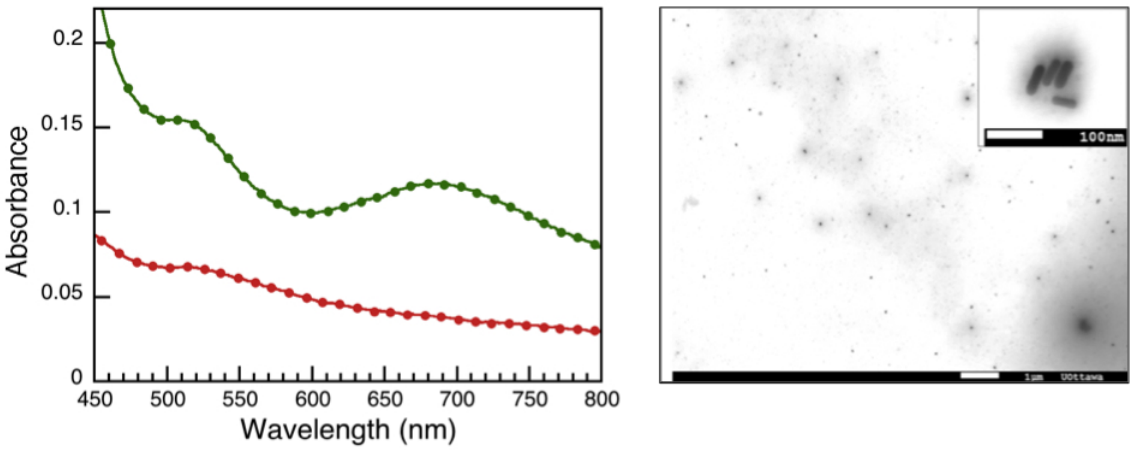

Figure 4.7: (Left) Absorption spectra of the SU-8 film after irradiation (*Red*) and the dissolved film (*Green*) for AuNRs with an aspect ratio of 3. Note that the optical path in the main figure is 17 times longer in solution than in films; 10 mm for the green (solution) and only 0.58 mm for the film. (Right) SEM image of AuNRs in the dissolved non-crosslinked AuNR/SU-8 film.

UV-vis spectroscopy revealed incomplete recovery of the longitudinal plasmon absorption band (Figure 4.7 left). Furthermore, extensive examination of SEM images showed that no spherical particles were present (Figure 4.7 right). The inset on Fig-

ure 4.7 shows a representative zoomed-in image of an irradiated dissolved film. No spherical nanoparticles were observed and the preservation of AuNR shape and their corresponding aspect ratio (1 : 3) was confirmed. It is worth noting that the dissolution of fully crosslinked films is not feasible. Nevertheless, the interpretation offered for non-crosslinked films can be extended to the crosslinked ones due to the homologous conditions of the experiments performed, the extremely similar results obtained (see Figure 4.5) and knowing that the glass transition temperature for crosslinked films is below the reported localized surface plasmon temperature.[18]

In the case of thin polymer films the spectral changes can only be monitored easily in the direction perpendicular to the film surface. For this reason, in order to inspect the spectral changes in both directions a 10 x 10 mm block of SU-8 polymer containing AuNRs (AR = 4) was constructed and the spectral differences were recorded. The block was prepared by slow evaporation of the solvent at room temperature over a period of 2 days following solution mixing.

Absorption spectra were recorded in the two directions (90 degree rotation) and then subtracted. As shown in Figure 4.8, the spectral changes when the sample is rotated by 90 degrees are consistent with AuNR reorientation. However, visual changes are not as evident as in their thin film counterparts. Same modified characteristics were appreciated on the opposite side (180 degree rotation) to the one exposed to light indicating the studied phenomenon occurs not only at the surface of the exposed area but also at the bulk.

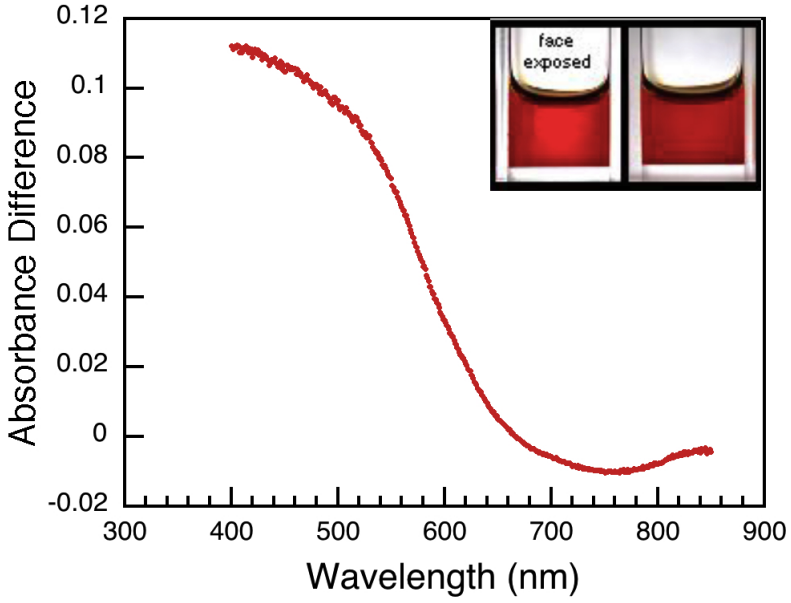

Figure 4.8: Absorption difference for a polymer 10 x 10 mm block made of SU-8 containing AuNR (AR = 3). The inset shows the face illuminated at 690 nm (left) and after 90 degree rotation of the cuvette the face that was not illuminated (right). The spectrum corresponds to the absorbance difference between the two cuvette faces (illuminated minus perpendicular).

AuNRs Alignment for Patterning Applications

The spontaneous alignment of AuNRs upon irradiation has clear implications for imaging. In order to illustrate the potential of AuNR alignment for patterning applications a maple leaf design was used as a mask leaving the pattern to be printed exposed to light irradiation. The results obtained upon the application of 690 nm laser pulses are presented on Figure 4.9. The red leaf represents the exposed part, while the periphery corresponds to the unexposed part of the film. It is also worth highlighting that stable images are obtained; even in non-crosslinked films the image persists for several months at room temperature.

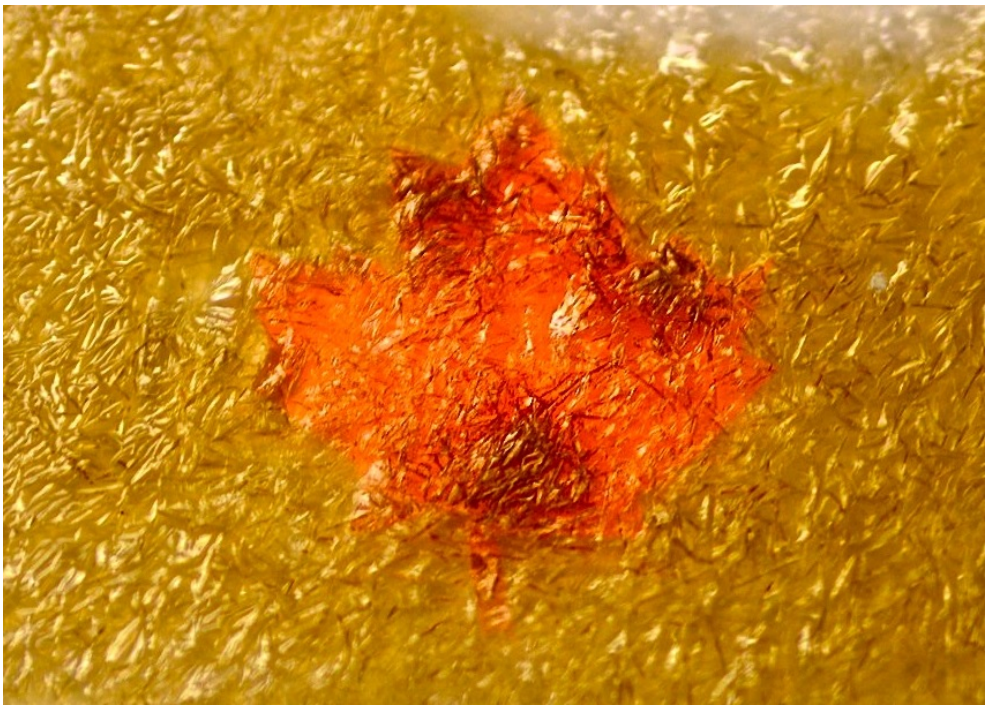

Figure 4.9: The red leaf represents the area where AuNRs have been aligned upon exposure to 690 nm light. The maple leaf is 11.4 mm wide and the film thickness is 0.58 mm.

4.4.3 Other Polymers

In order to explore the generality of the phenomenon studied in this chapter, tests were also performed in other polymers (Figure 4.10) such as polymethylmethacrylate (PMMA) and in silicone (PDMS); the former were successful, while the AuNRs proved incompatible with the latter. In the case of AuNR/PMMA films the orientation of AuNRs required to irradiate the samples with higher energies than the one needed for SU-8 photoresist. This may be a reflection of the higher Tg for PMMA which is something to consider if other polymers were to be used for patterning.

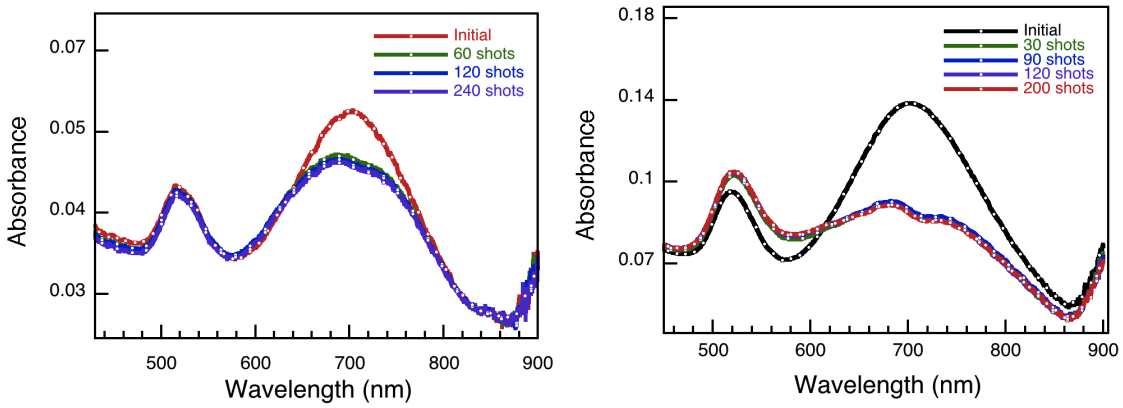

Figure 4.10: Absorption spectra of red-light oriented AuNR (AR = 3) in PMMA films exposed to 1 mJ (left) and 5 mJ (right) laser pulses at 690 nm. The number of laser pulses is given in each panel.

4.4.4 Randomization by Heat

In order to test if randomization of aligned AuNR is feasible previously oriented films were heated up to 100°C. In spite of the fact that the temperature used is close to the glass transition temperature for PMMA and well above of that of non-crosslinked SU-8 photoresist, heat did not lead to AuNR randomization. Seemingly, local changes in crosslinking might prevent reorientation.

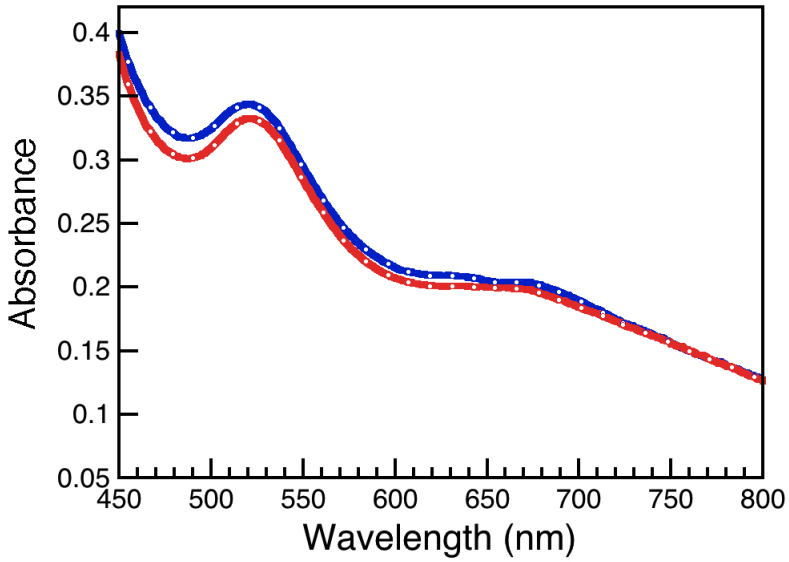

Figure 4.11: Absorption spectra of red-light oriented AuNRs in SU-8 film (*Blue*) and the same film after 1h heating (*Red*). Polymer SU-8, AR = 3. Notice a minor (but real) increase at 530 nm.

4.5 Conclusions

In this chapter gold nanorods of different aspect ratios were synthesized and successfully incorporated into SU-8 photoresist and PMMA films. By selectively exciting the longitudinal plasmon band of AuNRs it was possible to induce the spontaneous orientation of the nanostructures which lead to significant changes in the absorption spectrum of the films accompanied by a visible color change. The phenomenon shown in this chapter proved that the spontaneous self-assembly of AuNRs *via* plasmon excitation is a useful tool for patterning applications generating robust patterns which persist for extended periods of time.

REFERENCES

[1] NR Jana, L Gearheart, and CJ Murphy. Wet chemical synthesis of high aspect ratio cylindrical gold nanorods. *The Journal of Physical Chemistry B*, 105:4065–4067, 2001.

[2] JC Hulteen and CR Martin. General template-based method for the preparation of nanomaterials. *Journal of Materials Chemistry*, 7:1075–1087, 1997.

[3] BD Busbee and SO Obare. An improved synthesis of high aspect ratio gold nanorods. *Advanced Materials*, 15:414–416, 2003.

[4] CA Foss, , GL Hornyak, JA Stockert, and CR Martin. Optically transparent nanometal composite membranes. *Advanced Materials*, 5:135–136, 1993.

[5] X Huang, IH El-Sayed, W Qian, and MA El-Sayed. Cancer cell imaging and photothermal therapy in the near-infrared region by using gold nanorods. *The Journal of the American Chemical Society*, 128:2115–2120, 2011.

[6] MK Oo, Y Yang, Y Hu, M Gomez, H Du, and H Wang. Gold nanoparticle-enhanced and size-dependent generation of reactive oxygen species from protoporphyrin IX. *ACS Nano*, 6:1939–1947, 2012.

[7] M Boronat and A Corma. Molecular approaches to catalysis: Naked gold nanoparticles as quasi-molecular catalysts for green processes. *Journal of Catalysis*, 284:138–147, 2011.

[8] L Tian, E Chen, N Gandra, A Abbas, and S Singamanen. Gold nanorods as plasmonic nanotransducers: Distance-dependent refractive index sensitivity. *Langmuir*, 28:17435–17442, 2012.

[9] Y Dirix, C Bastiaansen, W Caseri, and P Smith. Oriented pearl-necklace arrays of metallic nanoparticles in polymers: A new route toward polarization-dependent color filters. *Advanced Materials*, 11:223–227, 1999.

[10] BM van der Zande, L Page, RA Hikmet, and A van Blaaderen. Optical properties of aligned rod-shaped gold particles dispersed in poly(vinyl alcohol) films. *The Journal of Physical Chemistry B*, 103:5761–5767, 1999.

[11] C Murphy and CJ Orendorff. Alignment of gold nanorods in polymer composites and on polymer surfaces. *Advanced Materials*, 17:2173–2177, 2005.

[12] DB Shao and SC Chen. Direct patterning of three-dimensional periodic nanostructures by surface-plasmon-assisted nanolithography. *Journal of Micromechanics and Microengineering*, 6:2279–2283, 2006.

[13] P Xue, J Bao, YJ Chuah, NV Menon, Y Zhang, and Y Kang. Protein covalently conjugated SU-8 surface for the enchancement of mesenchymal stem cell adhesion and proliferation. *Langmuir*, 30:3110–3117, 2014.

[14] J Carlier, S Arscott, V Thomy, JC Fourrier, F Caron, JC Camart, C Duron, and P Tabourie. Integrated microfluidics based on multi-layered SU-8 for mass spectrometry analysis. *Journal of Micromechanics and Microengineering*, 14:619–624, 2004.

[15] R Feng and RJ Farris. Influence of processing conditions on the thermal and mechanical properties of SU8 negative photoresist coatings. *Journal of Micromechanics and Microengineering*, 13:80–88, 2003.

[16] W He, S Hou, X Mao, X Wu, Y Ji, J Liu, X Hu, K Zhang, C Wang, Y Yang, and Q Wang. Peptide-tailored assembling of Au nanorods. *Chemical Communications*, 47:5482–5484, 2011.

[17] Z Zheng, T Tachikawa, and T Majima. Single-particle study of Pt-modified Au nanorods for plasmon-enhanced hydrogen generation in visible to near-infrared region. *The Journal of the American Chemical Society*, 136(19):6870–6873, 2014.

[18] C Fasciani, CJ Bueno-Alejo, M Grenier, JC Netto-Ferreira, and JC Scaiano. High-temperature organic reactions at room temperature using plasmon excitation: Decomposition of dicumyl peroxide. *Organic Letters*, 13:204–207, 2010.

[19] AD Campo and C Grenier. Gold nanorods: Synthesis, characterization and applications. *Journal of Micromechanics and Microengineering*, 17:R17–R95, 2007.

[20] SW Youn, A Ueno, M Takahashi, and R Maeda. Microstructuring of SU-8 photoresist by UV-assisted thermal imprinting with non-transparent mold. *Microelectronic Engineering*, 85:1924–1931, 2008.

[21] ML Marín, KL McGilvray, and JC Scaiano. Photochemical strategies for the synthesis of gold nanoparticles from Au(III) and Au(I) using photoinduced free radical generation. *The Journal of the American Chemical Society*, 130(49):16572–16584, 2008.

[22] H Chen, L Shao, Q Li, and J Wang. Gold nanorods and their plasmonic properties. *Chemical Society Reviews*, 42:2679–2724, 2013.

[23] KL McGilvray, MR Decan, D Wang, and JC Scaiano. Facile photochemical synthesis of unprotected aqueous gold nanoparticles. *The Journal of the American Chemical Society*, 128(50):15980–15981, 2006.

[24] J Pérez-Juste, I Pastoriza-Santos, LM Liz-Marzán, and P Mulvaney. Gold nanorods: Synthesis, characterization and applications. *Coordination Chemistry Reviews*, 249(17-18):1870–1901, 2005.

[25] CJ Bueno-Alejo, C D'Alfonso, NL Pacioni, M González-Béjar, M Grenier, O Lanzalunga, EI Alarcon, and JC Scaiano. Ultraclean derivatized monodisperse gold nanoparticles through laser drop ablation customization of polymorph gold nanostructures. *Langmuir*, 28(21):8183–8189, 2012.

Chapter 5

Plasmon Heating Mediated Friedel-Crafts Alkylation of Anisole Using Supported AuNP@Nb_2O_5 Catalysts

5.1 Introduction

Niobium oxides are a very versatile group of materials showing a broad variety of applications in which they can be used. Because of its larger bandgap compared to TiO_2 anatase and several other remarkable physical and chemical properties like high stability in aqueous media and strong surface acidity Nb_2O_5 has become a suitable candidate for several applications such as solar cells, sensing, catalysis and electrolytic capacitors, among others.[1, 2, 3, 4] Niobium pentoxide (Nb_2O_5) is the most thermodynamically stable form of the niobium-oxygen systems and has many polymorphic forms that give rise to a series of structural phases.

Great controversy has always existed with respect to the numerous polymorphs of Niobium pentoxide generating contradictions and confusion. It wasn't until 1966 when considerable efforts started to be directed towards conveying the information gathered regarding the structural complexity of Nb_2O_5 materials into a more universal classification system. The most extended and accepted one was first adopted by Schafer *et al.* in which the most stable polymorphs are classified based primarily on the temperature at which they were obtained: TT, T, M, H (from the german Tief-Tief, Tief, Medium and Hoch, meaning low-low, low, medium and high, respectively).[5]

5.1.1 Fundamental Properties of Nb_2O_5

Crystal Structure

Niobium pentoxide presents extensive polymorphism. It can exist in an amorphous state as a mixture of distorted NbO_6 octahedra and NbO_4 tetrahedra or in any of its 15 crystalline polymorphic forms. The most stable and commonly obtained structures are TT-Nb_2O_5 (pseudohexagonal), T-Nb_2O_5 (orthorombic) and H-Nb_2O_5 (mon-

oclinic) whose structures are shown on Figure 5.1. Among them, the H form is the most thermodynamically stable phase while TT-Nb_2O_5 is the least stable one.[6, 7, 8]

TT-Nb_2O_5 has a pseudo hexagonal crystal lattice. On the *ab* plane, each niobium atom is located at the centre of either four, five or six oxygen atoms; along the *c* axis, the atoms arrange in a way that niobium and oxygen atoms are intercalated (Nb-O-Nb-O). Each unit cell encompasses half of the corresponding Nb_2O_5 theoretical formula presenting a constitutional defect composed of an extra oxygen atom on the plane *ab*. Yet, it is a one atom oxygen deficiency along the *c* axis the one responsible for the distorted hexagonal lattice.

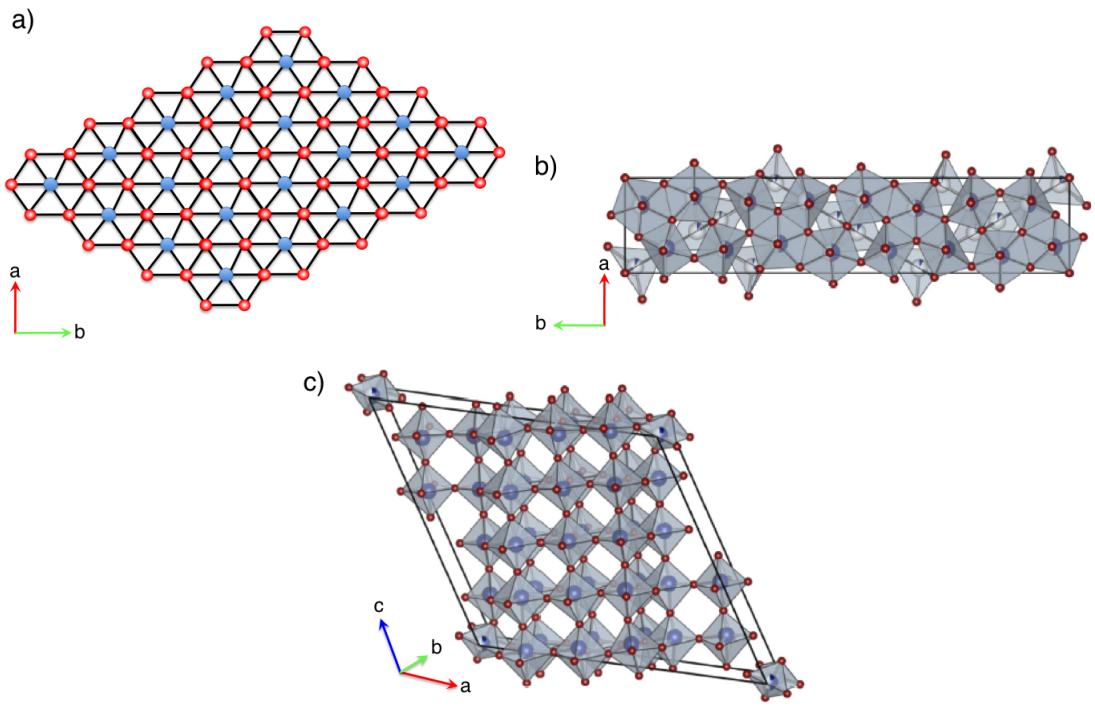

Figure 5.1: Pseudohexagonal structure of the TT-Nb_2O_5 phase (a), orthorhombic structure of T-Nb_2O_5 phase (b) and monoclinic structure of the H-Nb_2O_5 phase (c). Blue spheres represent niobium atoms; red spheres represent oxygen atoms. Adapted with permission from ref. [6]. Copyright (2017) Elsevier.

In a T-Nb_2O_5 polymorph (Figure 5.1b) each niobium atom is located in the centre of either six or seven oxygen atoms forming a mixture between pentagonal bipyramids and distorted octahedra connected to each other -on the plane *ab*- trough the edges or corners while connecting only through the corners along the *c* axis.

H-Nb_2O_5 (Figure 5.1c) has a monoclinic lattice formed by blocks of dimensions 3 x 4 and 3 x 5 NbO_6 octahedra units connected through their corners on the plane *ab* and through the edges along the *c* axis.

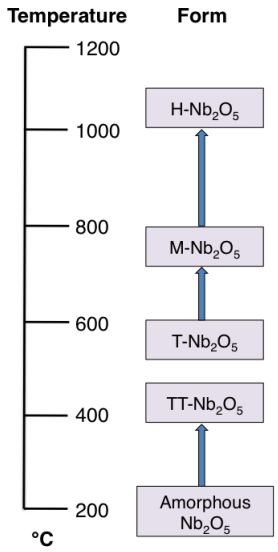

Figure 5.2: Temperature dependent Nb_2O_5 phase transformations. Adapted from ref. [9].Copyright (2017) Elsevier.

The different polymorphs can be obtained by regulating the temperature during synthesis. Moreover, it is possible to go from a less stable phase to a more stable one *via* heat treatment, as shown in Figure 5.2.

Amorphous niobium pentoxide is commonly obtained at relatively low temperatures compared to the other phases and can be further crystallized into TT-Nb_2O_5 or T-Nb_2O_5 by heat treatment at approximately 500°C to 600°C. At higher temper-

atures (≈ 800°C) the structure can be transformed into the M-Nb_2O_5 (tetragonal) polyform to finally reach the most thermodynamically stable phase (H-Nb_2O_5) when treated at temperatures above 1000°C. Although temperature control is a useful and simple tool to selectively obtain different polymorphs it is also possible to vary other parameters during synthesis in order to achieve the desired Nb_2O_5 structure.

Electrical Properties

Nb_2O_5 is a wide band gap *n*-type semiconductor. Its band gap energy ranges between 3.0 and 5.3 eV and is attributable to the conduction band formed by the empty 4d orbitals of the Nb^{5+} atoms. The band gap values obtained vary considerable within the presented range. As seen in Table 5.1, Nb_2O_5 based materials typically behave as a conductive material. However, in some cases it can also act as an insulator depending on how the synthetic process was conducted.

Table 5.1: Band gap energy values reported for Niobium Pentoxide

Phase	Eg (eV)	Material	Reference
Amorphous Nb_2O_5	3.4	Thin Films	[10]
	3.4-5.3	Thin Films	[11]
	3.4	Sol-gel powders	[12]
TT-Nb_2O_5	3.4	Sol-gel powders	[12]
T-Nb_2O_5	3.4	Sol-gel powders	[12]
	3.4	Single crystal	[12]
H-Nb_2O_5	3.4	Sol-gel powders	[12]
	3.0	Single crystal	[13]

Lewis and Brønsted Acidity

In 1983, Iizuka *et al.*[14] investigated the acid properties of Nb_2O_5 by conducting an infrared spectroscopic study of pyridine adsorbed on niobium pentoxide. When Nb_2O_5 was treated at relatively low temperatures ($\approx$ 100 °C - $\approx$ 150°C) both Brønsted and Lewis acid sites were detected. Nevertheless, at higher pre-treatment temperatures ($\approx$ 300°C), a sharp decrease in Brønsted acidity was observed while the Lewis acid band remained and reached its maximum. At pre-treatment temperatures above $\approx$ 500°C both types of acid sites decreased remarkably.

Brønsted acid sites (NbO_6 octahedra) are generated by the formation of exposed -OH groups *via* proton transfer from a water molecule promoted by the highly polarized Nb-O bonds. On the other hand, Lewis acid sites (NbO_4 tetrahedra) are formed due to the presence of exposed cations in proximity to oxygen vacant sites. [15] For this reason, at pre-treatment temperatures of approximately 300°C dehydration occurs decreasing the overall Brønsted acidity accompanied by an increase in Lewis acidity due to the higher quantity of exposed cations close to oxygen vacancies.

5.1.2 Synthesis of Nb_2O_5

In the past decades, several synthetic routes have been developed in order to obtain Nb_2O_5 based materials. *i.e.* electrodeposition, anodization, vapour phase deposition, solvothermal and hydrothermal, thermal oxidation and sol-gel methods. Among them, the most used ones are the hydrothermal/solvothermal and sol-gel methods.

Hydrothermal/Solvothermal Methods

In general terms, hydrothermal/solvothermal methods involve an ionic Nb^{5+} source in an acidic or basic media -to induce deposition of Nb_2O_5- heated at elevated temperatures for a predetermined length of time. This process allows nucleation and growth of crystalline Nb_2O_5 under relatively mild conditions; it has the advantage of not requiring costly equipment and it can be optimized to yield homogeneous crystalline powders.[16]

Sol-Gel Methods for Mesoporous Nb_2O_5

As explained in detail in Chapter 2, sol-gel processes are the main methods used to prepare mesoporous materials -including niobium oxides- by converting the selected monomers into a colloidal solution (sol) that acts as a precursor for the formation of an integrated network (gel).

An analogous concept to the templating mechanism and acid catalysed hydrolysis followed by condensation -shown on Figures 2.4 and 2.3, respectively- apply in the case of the niobium oxide mesoporous materials prepared in this chapter. In this research, niobium ethoxide ($Nb(OEt)_5$) is used as the source of niobium whilst the cylindrical micelles -that will self assemble to form the template on which Nb_2O_5 will grow- are conformed by the association of pluronic acid (P-123) molecules.[17, 18]

P-123 is a poly(ethylene)glycol - poly(propylene)glycol - poly(ethylene)glycol triblock copolymer (PEG-PPG-PEG). It is composed of a seventy unit poly(propylene) oxide central hydrophobic chain and two twenty unit poly(ethylene)oxide hydrophilic chains at the ends (See Figure 5.3). Pluronic acid is known to template 2D hexagonal structures under acidic aqueous conditions.[17] However, even in the case of hexagonally ordered structures a much poorer regularity is obtained for Nb_2O_5 materials in comparison mesoporous silica.[19]

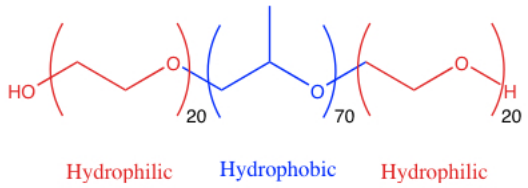

Figure 5.3: Chemical structure of the amphiphilic triblock copolymer P-123.

Because the structural, physical and chemical properties of niobium pentoxide are affected by temperature the removal of the template by calcination at high temperatures ($\approx 500°C$) is often avoided and replaced by soxhlet extraction at much lower temperatures.

5.1.3 Nb_2O_5 as a Catalyst

In the past couple of decades, the number of catalytic applications for Nb_2O_5 have increased considerably. Furthermore, the various functions of niobium oxide materials in different heterogeneous catalytic processes have been well established. Four main possible roles have been attributed to Nb_2O_5 in catalysis; niobium pentoxide can act as a promoter or active phase, as a support, as a solid acid catalyst or behave as a redox material.[7]

It has been previously reported that the presence of small quantities of niobium pentoxide enhances the selectivity, catalytic activity and shelf life of some functional catalysts.[20, 21] Also, when mixed with other metals or metal oxides, photosensitivity and redox properties can be induced.[22, 23, 24] Last but not least, the surface of hydrated Nb_2O_5 can exhibit high catalytic activity and selectivity towards acid catalyzed reactions due to its tunable Brønsted and Lewis acidity. Moreover, it has been proven that -remarkably- the Lewis acid sites on the surface of hydrated Nb_2O_5 can be water tolerant, a feature that highly contributes to the stability and applicability of niobium oxide based catalysts in contrast to other metal oxides.

Pure Nb_2O_5 has been used as a catalyst for countless reactions. *i.e.* transesterification of β-keto esters in the presence of various alcohols[25, 26], oxidative dehydrogenation of organic materials[27, 28] and polycondensations[29], among others.

5.1.4 Friedel-Crafts Reaction

The Friedel-Crafts alkylation reaction -first reported in 1877- is one of the oldest and most useful Lewis acid-assisted reactions for the transformation of aromatic compounds.[30] Typically, a Friedel-Crafts alkylation occurs *via* electrophilic substitution using stoichiometric and/or substoichiometric amounts of either Brønsted acids or strong mineral Lewis acids such as $AlCl_3$, as shown in Figure 5.4.

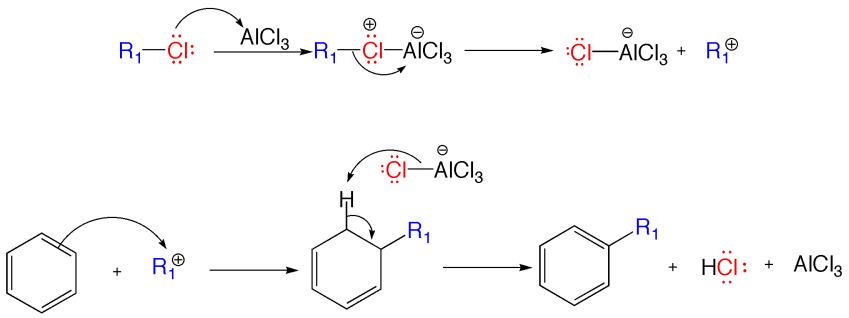

Figure 5.4: General mechanism for a Friedel-Crafts alkylation reaction.

On a first instance the chlorine atom of the alkyl halide reacts with the Lewis acid. Upon loss of the halide to the Lewis acid a carbocation is formed that will then be attacked by the benzene ring following an electrophilic aromatic substitution pathway. It has been previously reported that the mechanism for Friedel-Crafts alkylation over solid acid catalysts is analogous to the one in homogeneous systems where Lewis acid catalysts are used.[31, 32, 33]

Niobium-based acid catalysts have shown to be very promising as its Lewis acid sites present a certain degree of water tolerance, unlike other solid Lewis acid catalysts

-such as $AlCl_3$, $FeCl_3$, BF_3 and $ZnCl_2$- which undergo water deactivation[34, 35, 36] making Nb_2O_5 a more robust catalyst compared to the conventional ones.[37] However, the main drawback continues to be the elevated temperatures required to perform the catalysis.[38, 34, 35] The harsh conditions required to achieve these transformations have stimulated the synthesis and design of new catalysts capable of performing under milder conditions. Moreover, it is important to develop new photocatalytic materials that can be controlled and activated by light promoting environmentally friendly processes. Adapting traditional thermal processes to light activation generally allows for milder experimental conditions and provides spatio-temporal control making them suitable for imaging and on-demand triggering. Furthermore, heterogeneous metal-nanoparticle photocatalysts have been recognized as suitable materials for green chemistry due to their efficient light harvesting properties.[39]

As mentioned in previous chapters, surface plasmon resonance (SPR) excitation of noble metal nanoparticles can induce antenna-like interactions leading to enhanced absorption, electron/hole transfer and localized plasmon heating. These effects can contribute to catalysis by activating molecules in the vicinity of the nanoparticles facilitating chemical transformations.[40] It has been reported that the excitation of the SPR of AuNPs can lead to local temperatures of approximately 500°C.[41] This localized plasmon heating has been reported to facilitate some processes such as the generation and release of singlet oxygen from anthracene endoperoxide-functionalized AuNPs and to promote the de-hybridization of double stranded DNA.[42]

Two aspects related to plasmon excitation are mainly used in heterogeneous catalysis, namely, charge-transfer and heating. Many examples are available in the literature regarding the active participation of charge-transfer -resulting from plasmon excitation- in the local chemistry; hydrocarbon reforming, oxidation and hydrogenation reactions, as well as the decomposition of phenol *via* assisted Fenton decompo-

sition of hydrogen peroxide are some of the examples found in the literature.[43, 44]

Besides the active participation of AuNP in the localized chemistry of catalytic processes it has also been reported that plasmonic nanostructures can be used to drive chemical reactions by behaving as a heat source alternative to conventional bulk heating providing the necessary energy for the catalytic reactions to occur at a lower temperature.[43] Moreover, it has been demonstrated that the plasmon excitation of AuNP deposited on metal oxide solids can enhance the performance of a catalyst through the SPR effects by assisting photocatalytic redox reactions or energy conversion processes giving rise to superior light-to-heat conversion efficiencies.[43, 45]

While there are a few reports related to photocatalytic Friedel- Crafts chemistry, they refer to the photoexcitation of organic substrates rather than the photoactivation of the catalytic reaction.

5.1.5 About this Chapter

This chapter examines the possibility of combining the Lewis acidic properties of two niobium oxide-based materials -previously characterized by other members of Scaiano Group [46, 47]- with the localized plasmon heating effect of AuNPs in order to perform a Friedel-Crafts reaction at lower temperatures eliminating the need of an external heat source.

Two different niobium oxide catalysts were synthesized in order to assess the feasibility of plasmon-mediated catalysis of the Friedel-Crafts alkylation of anisole by benzyl chloride. AuNPs were supported either on commercial niobium oxide (HY 340) or on mesoporous niobium oxide by adsorbing the gold salt in the materials followed by reduction -with sodium borohydride- to its metallic form.

The achievement of a water tolerant catalyst is also one of the goals in this chapter. Commonly used solid acids -such as $AlCl_3$ are not water tolerant, making niobium

oxide based catalysts better candidates for this purpose due to the higher water tolerance its Lewis acid sites present in comparison to other solid acids.

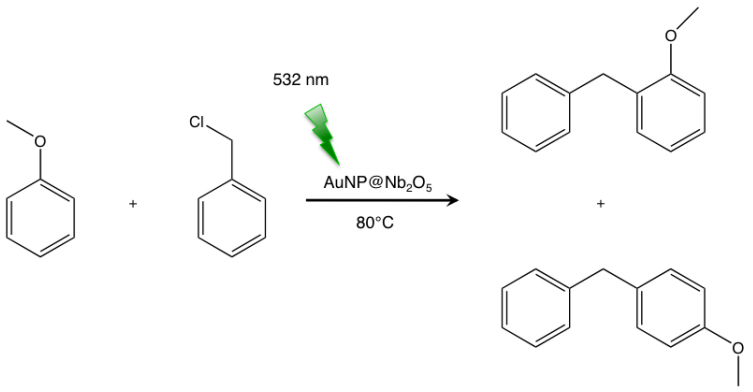

Figure 5.5: Schematic representation of the Friedel-Crafts alkylation of anisole by benzyl chloride using the synthesized catalysts.

For this reason, information was gathered regarding the extent of the water tolerance of Lewis acid sites present in the Nb_2O_5 catalysts considered in this study. This also constitutes fundamental information needed for future and undergoing projects, such as the determination of the range of applicability of other niobium based materials. *i.e.* we are currently trying to discover the range of applicability of iridescent niobium oxides in organic chemistry, for which $AlCl_3$ and other solid acids can not be used for.

5.2 Experimental

5.2.1 Reagents

Niobium (V) ethoxide ($Nb_2(OEt)_5$), pluronic acid (P-123), gold(III) chloride trihydrate ($HAuCl_4 \cdot 3H_2O$), sodium chloride (NaCl), hydrochloric acid (HCl), benzyl chloride (99 %), anisole (99 %) and ethanol (98 %) were acquired from Sigma Aldrich and used without further purification. Niobium oxide (Nb_2O_5) HY-340 was a gift courtesy of CBMM-Brazil. For the preparations that required aqueous conditions purified water *via* a Millipore Milli-Q system (resistivity 18.2MΩ cm^{-1} at 25°C; 0.22 μm filter) was used.

5.2.2 Instrumentation

Gas Chromatography (GC-FID)

Product analyses and quantification were performed in a PerkinElmer gas chromatograph, model Clarus 480 equipped with a flamed ionization detector system.

Infrared Spectroscopy

Sample analyses were performed *via* infra red spectroscopy using a Thermo Nicolet NEXUS 670 FT-IR.

UV Visible Spectroscopy

AuNPs supported on Nb_2O_5 materials were characterized using an Agilent Cary 7000 Universal Measurement Spectrophotometer set in diffuse scattering mode.

Transmission Electron Microscopy

TEM analyses were carried out on a JEM 2100F FETEM microscope (JEOL, 200 kV, 0.14 nm resolution). For this purpose, samples were prepared by sonicating a suspension of the material in ethanol on a carbon-coated copper grid. The digital analysis of the TEM micrographs was performed using Digital MicrographTM 3.6.1 by Gatan.

5.2.3 Synthesis of Mesoporous Nb_2O_5

Mesoporous Nb_2O_5 was synthesized based on a method reported by Marín *et al.*[48] Briefly, 11 mL of Milli-Q water at 40°C was used to disperse 1.5 g of P-123. Then, 45 mL of HCl (2 M) and 5 g of $Nb(OEt)_5$ (15.7 mmol) were added drop wise under stirring and left to stir for 24 hours at 40°C. The solution was then put in a Teflon-lined autoclave at 100°C for 48 hours. The resulting solid was filtered, washed with Milli-Q water and dried under air at room temperature. Finally the surfactant was removed by a two-step Soxhlet extraction using 300 mL of 1 % HCl in 95 % EtOH and 120 mL of 95 % EtOH respectively. The template-free mesoporous $Nb_2O_5 \cdot nH_2O$ was dried in the oven at 120°C for 18 hours.

5.2.4 Synthesis of $Na^+/Nb_2O_5 \cdot nH_2O$

$Na^+/Nb_2O_5 \cdot nH_2O$ was synthesized based on a method reported by Nakajima *et al.*[37] Briefly, 1 g of $Nb_2O_5 \cdot nH_2O$ was suspended in 200 mL of 0.2 M NaCl. The pH of the solution was adjusted to 5.5-5.8 by adding 0.05 M NaOH and the final solution was stirred for 24h. Then, the solid was collected by suction filtration and washed with Milli-Q water until Na^+ and Cl^- ions were no longer detected with crystal violet indicator and dried at 100 °C for 12 h. Finally, $Na^+/Nb_2O_5 \cdot H_2O$ was dried in the

oven at 120°C for 18 hours. The treatment of $Nb_2O_5 \cdot nH_2O$ with Na^+ blocks the Brønsted acid sites and was used as a mode of comparison during this work.

5.2.5 AuNP Incorporation on Nb_2O_5 Materials

HY-340 AuNP@Nb_2O_5 and mesoporous AuNP@Nb_2O_5 were synthesized based on a method developed by Mitsudome *et al.*[49] Briefly, 300 mg of Nb_2O_5 material was added to 100 mL of an aqueous $HAuCl_4 \cdot 3H_2O$ (176.58 μM). Then, 0.09 mL of a 10 % NH_4OH solution was added and the resulting mixture was stirred overnight at room temperature.

The solid containing Au^{3+} was filtered, washed with water, and re-suspended in 100 mL of a 200 mM solution of sodium borohydride and stirred for 2 h in order to reduce the gold salt. Finally, the purple solid was filtered, washed with water, dried under ambient conditions and lyophilized in order to remove the excess of water. The catalysts were kept in a desiccator and protected from light. The average nanoparticle diameter was determined to be 4.4 nm (mesoporous AuNP@Nb_2O_5) and 6.2 nm (HY-340 AuNP@Nb_2O_5) by TEM analysis.

5.2.6 Catalytic Reactions

Friedel-Crafts alkylation reactions were performed under nitrogen gas flow in a Pyrex batch reactor connected to a condenser. Briefly, 65 mg of the catalyst was added to a mixture of the aromatic reagents, anisole (15 ml) and benzyl chloride (1 mL). The reaction was heated up by means of a silicone oil bath to 80, 100, 120 and 150°C, respectively.

To analyze the time and temperature dependence of each reaction, 0.1 mL aliquots were taken, rapidly cooled to room temperature, centrifuged at 3200 rpm and analyzed

by gas chromatography coupled to a flame ionization detector (GC-FID). The plasmon heating effect was evaluated by irradiating a mixture of 2 mg of the corresponding catalyst, 184.7 μL of anisole and 12.6 μL of benzyl chloride in an NMR tube placed in a QuadLED setup (532 nm), see Figure 5.13. The NMR tube was connected to a thermocouple detector and a Teflon tube flowing N_2 gas.

5.2.7 Pyridine Adsorption Experiments

The amount of Lewis and Brønsted acid sites on the Nb_2O_5 materials was determined by the pyridine adsorption method by FT-IR measurements.[50, 51] Sample preparation was performed by pressing 50 mg of the corresponding catalyst into self-supporting disks (20 mm diameter) and then placed in an IR cell attached to a high pressure and temperature control closed system.

The pellet obtained was dehydrated at 150°C for 1 h under vacuum and then exposed to pyridine vapor at 150°C for 30 min. FT-IR spectra were recorded before and after pyridine adsorption and the number of Lewis (L-Py) and Brønsted (Py-H^+) acid sites was quantified considering a molecular absorption coefficient of 3.15 μmol cm^{-1} for L-Py and 1.20 μmol cm^{-1} for Py-H.

5.3 Results and Discussion

5.3.1 Material Characterization

Figure 5.6 shows the TEM images of the AuNP/Nb_2O_5 nanocomposites. The average diameter of the supported gold nanoparticles was found to be 6.2 nm and 4.4 nm for AuNP@Nb_2O_5 (HY-340) and AuNP@mesoNb_2O_5, respectively and the corresponding histograms. As can be seen highly polydispersed nanoparticles are obtained when amorphous niobium oxide is used. However a more monodispersed distribution is obtained when the mesoporous materials is used, probably due to the more organized structure (See Figure 5.7).

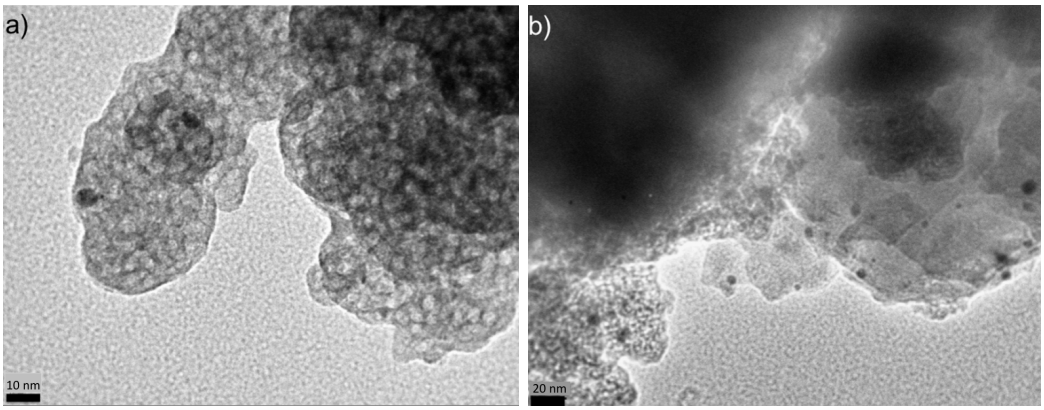

Figure 5.6: TEM micrographs of (a) amorphous AuNP/Nb_2O_5 and (b) mesoporous AuNP/Nb_2O_5

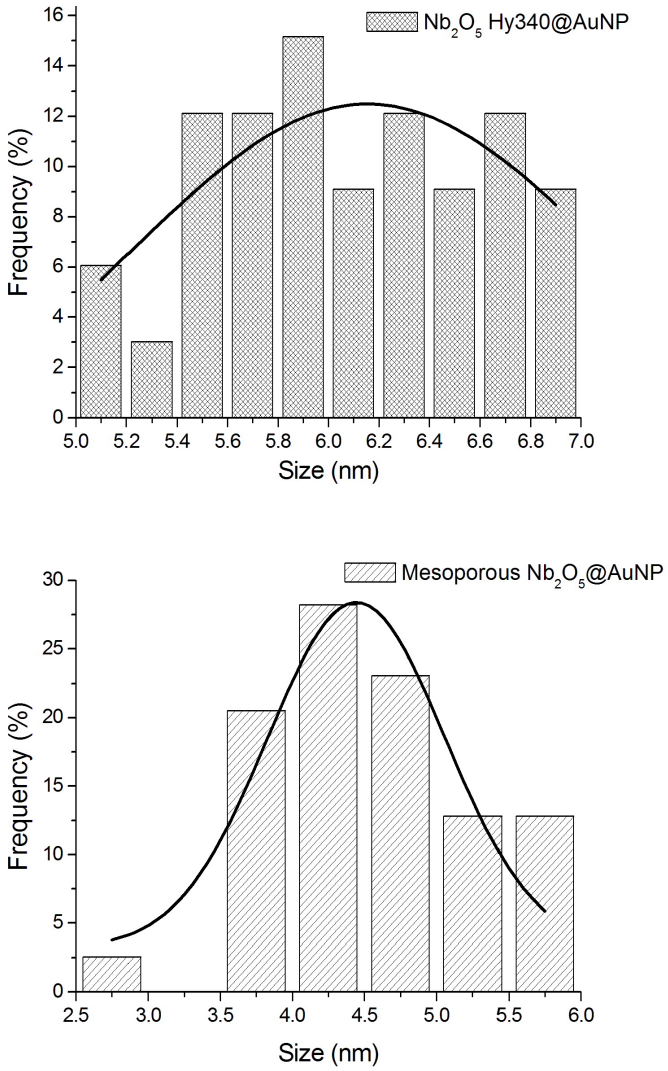

Figure 5.7: Size distribution histograms (a) amorphous AuNP/Nb_2O_5 , (b) mesoporous AuNP/Nb_2O_5

The number of Lewis and Brønsted acid sites for the different AuNP/Nb_2O_5 nanocomposites and bare niobium oxide materials was determined by the pyridine vapour adsorption method and reported on Table 5.2. These amounts were estimated by analyzing the characteristic FT-IR peaks at 1450 cm^{-1} and 1540 cm^{-1}. The former corresponds to pyridine-Lewis acid coordination adducts while the latter represents the number of pyridinium (PyH^+) ions formed upon reaction with the Brønsted acid sites.

Table 5.2: Number of Brønsted and Lewis acid sites for different Nb_2O_5 nanocomposites determined by pyridine adsorption.

Material	Brønsted Acids ($\mu molg^{-1}$)	Lewis Acids ($\mu molg^{-1}$)
Nb_2O_5 (HY-340)	0.29	0.0091
Na^+/Nb_2O_5 (HY-340)	0.0	0.014
AuNP@Nb_2O_5 (HY-340)	0.17	0.021
Nb_2O_5 (mesoporous)	0.031	0.039
AuNP@Nb_2O_5 (mesoporous)	0.015	0.032

The decrease in Brønsted acidity of the catalyst upon AuNPs incorporation can be attributed to the use of sodium borohydride as a reducing reagent during the synthesis in which an exchange between the sodium ions of $NaBH_4$ and the protons of the Brønsted acid sites is most likely to occur. This is clearly seen in the case of AuNP@Nb_2O_5 and is corroborated by the comparison between the Brønsted acidity of Nb_2O_5 and Na^+/Nb_2O_5 in which the acidity drastically decreases when sodium ions are added. The Lewis acidity of the catalyst stays relatively constant when AuNPs are incorporated either on Nb_2O_5 or on mesoporous Nb_2O_5. The gold loading of these materials is ≈2% which is comparable to the loading used in other AuNP supported catalysts (1%-5%).[52, 53]

5.3.2 Evaluation of Catalytic Activity

With the aim of exploring the extent of the contribution of AuNPs to the catalytic activity of the niobium-based materials, the Friedel-Crafts alkylation reactions were performed at different temperatures and followed over time in the presence and absence of LED irradiation. The reactions between anisole and benzyl chloride in the presence of the synthesized Nb_2O_5 hybrid materials were performed using a 1:50 benzyl chloride: anisole ratio in order to obtain quantitative amounts of alkylated ortho and para- isomer products avoiding, at the same time, the formation of secondary dialkylated products.

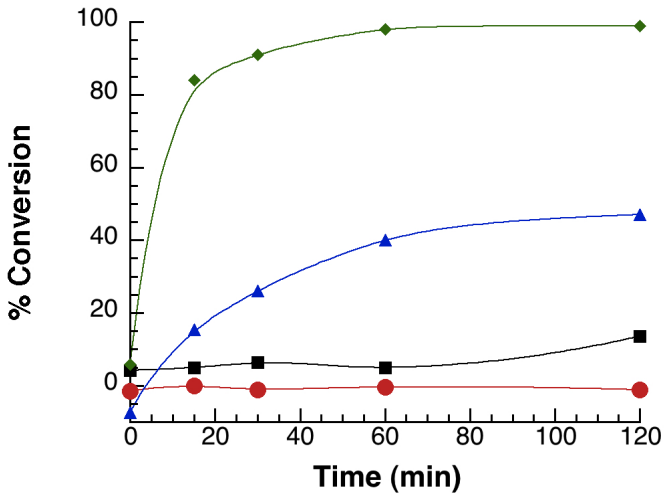

Figure 5.8: % Conversion of benzyl chloride with time at (*Red*) 80°C, (***Black***) 100°C, (*Blue*) 120°C and (*Green*) 150°C using AuNP@Nb_2O_5 (HY-340) as catalyst, under dark conditions.

As can be seen on Figures 5.8 and 5.9, in order for the reactions to proceed in the absence of LED irradiation, temperatures above 120°C were required when using either bare Nb_2O_5 materials or supported-AuNP nanocomposites as catalysts. Nonetheless, the conversions increased significantly at higher temperatures reaching 80 % and 100 % for AuNP@Nb_2O_5 mesoporous and AuNP@Nb_2O_5 (HY-340), re-

spectively. It is worth highlighting that at 80°C no conversion of benzyl chloride was observed under dark conditions.

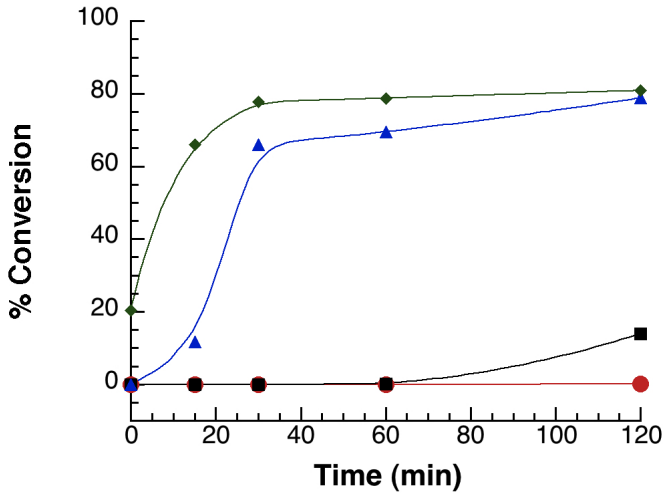

Figure 5.9: % Conversion of benzyl chloride with time at (*Red*) 80°C, (***Black***) 100°C, (*Blue*) 120°C and (*Green*) 150°C using AuNP@Nb_2O_5 (mesoporous) as catalyst, under dark conditions.

When comparing the AuNP-supported catalysts with the analogous bare supports -Figures 5.10 and 5.11- the latter were more active in the absence of light yet, the opposite was observed under LED irradiation (Figure 5.12) in which no benzyl chloride conversion was obtained using bare supports.

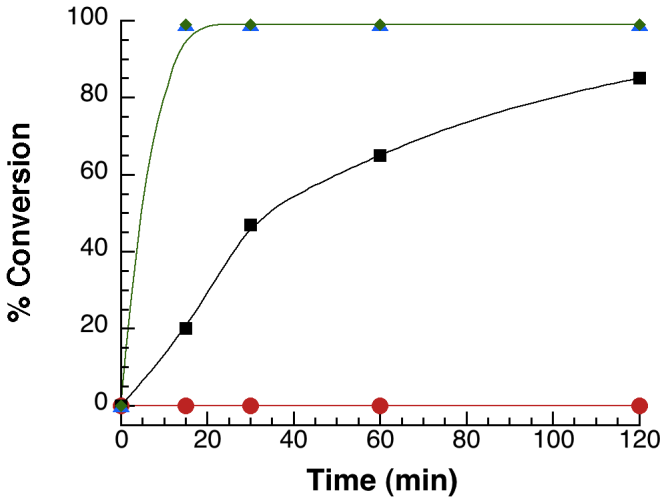

Figure 5.10: % Conversion of benzyl chloride with time at (*Red*) 80°C, (***Black***) 100°C, (*Blue*) 120°C and (*Green*) 150°C using Nb_2O_5 HY-340 as catalyst (there is an overlap between the curves at 120°C (*Green*) and 150°C (*Blue*)).

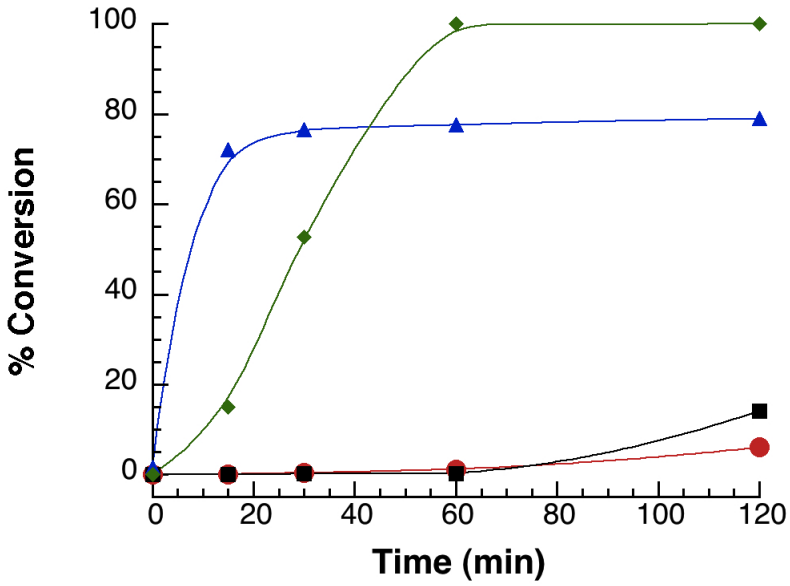

Figure 5.11: % Conversion of benzyl chloride with time at (*Red*) 80°C, (***Black***) 100°C, (*Blue*) 120°C and (*Green*) 150°C using mesoporous Nb_2O_5 as catalyst.

Figure 5.12 shows the percent conversion of benzyl chloride with time for the reactions catalyzed by AuNP@Nb_2O_5 (HY-340) and AuNP@Nb_2O_5 (mesoporous) under LED irradiation. During irradiation, the sample temperature reached 80°C; such bulk heating can be attributed to intense light absorption by the sample; see Figure 5.13 for the QuadLED irradiation system. However, in spite of the fact that the temperature reached was much lower than the temperature required for the reaction to proceed thermally (120°C), 90 % conversion was obtained within 2 hours. Therefore, product formation under irradiation conditions can be attributed to the local plasmon heating effect generated by plasmon excitation.

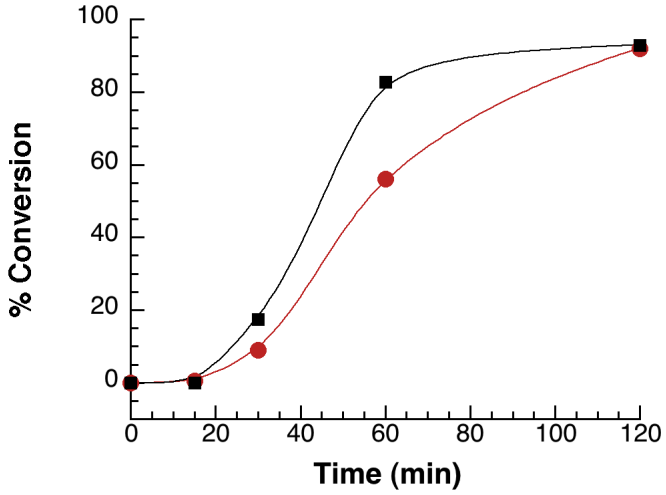

Figure 5.12: % Conversion of benzyl chloride with time under green light LED irradiation. (***Black***) AuNP@Nb_2O_5 and (*Red*) mesoporous AuNP@Nb_2O_5 (Temperature $\leq$ 80°C).

The conversion of benzyl chloride proceeded faster when using AuNP@mesoNb_2O_5 compared to AuNP@Nb_2O_5 (HY 340). These results are consistent with the fact that the former has a much higher surface area than the latter, reflecting its mesoporous structure. Since catalysis is a surface phenomenon this often results in faster reactions. In addition, these results agree with the fact that AuNP@Nb_2O_5 (mesoporous) contains more Lewis acid sites, which are suggested as responsible for the catalysis.

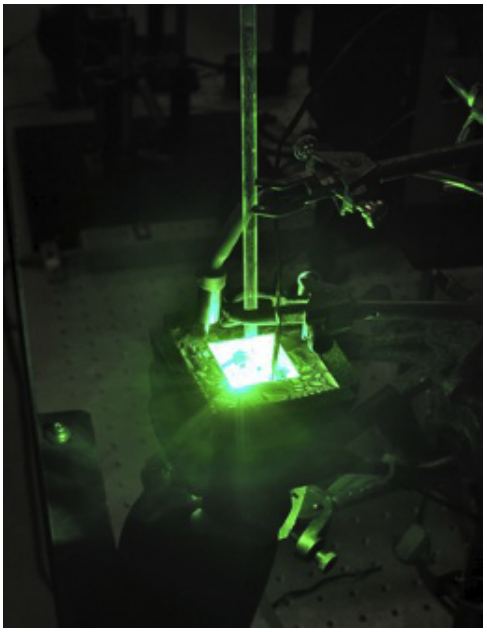

Figure 5.13: QuadLED irradiation setup showing the sample being irradiated from four different directions.

5.3.3 Stability Assays

So far, the use of supported AuNP in catalysis has been reported in the literature to elucidate the nature of active sites and reaction mechanisms.[54, 55, 56, 57] Only a few publications have included information on the thermal stability and stabilization of gold nanoparticles on solid supports.[56, 45]

In this study, the stability of AuNP@Nb_2O_5 solid materials was assessed by monitoring the surface plasmon band of AuNPs by UV-vis diffuse reflectance (DR) spectroscopy. The corresponding DR spectra of AuNP@Nb_2O_5 before and after reaction under LED irradiation at 80°C can be seen in Figure 5.14. A blue shift and change in the shape of the SPR band was recorded which is consistent with either a decrease in size and/or degree of aggregation of the AuNP, as previously reported in the literature.[58, 59, 60, 61]

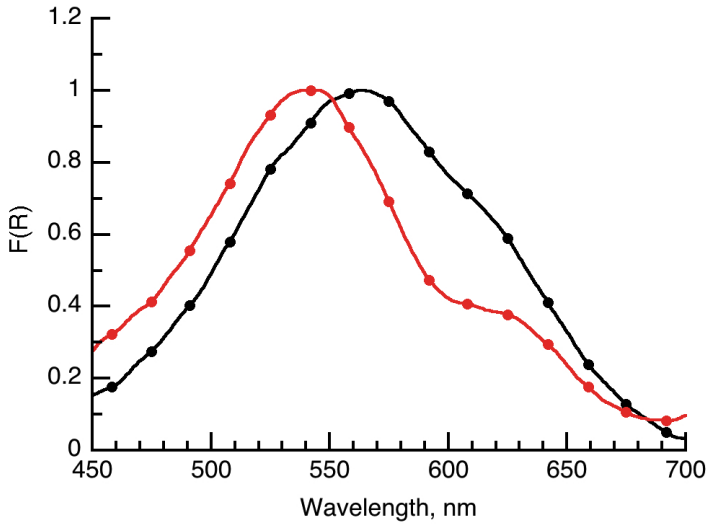

Figure 5.14: Normalized diffuse reflectance spectrum of AuNP@Nb_2O_5 (HY-340) (***Black***) freshly made catalyst and (*Red*) after the reaction with LED 80°C

SEM studies were not conclusive to establish a decrease in size and/or degree of aggregation due to the polydisperse nature of the AuNPs on the catalyst. The possibility that the blue shift reflected Au cations leaching into solution,[62] was ruled out as the supernatant tested negative for gold in solution. The recyclability of the AuNP@Nb_2O_5 catalysts was tested obtaining a maximum conversion of approximately 11 % upon a second use. A blue shift in the diffuse reflectance spectrum was also observed when performing the reaction using a conventional heat source (Figure 5.15), which can also be interpreted as a possible decrease in AuNP size and/or degree of aggregation, which may cause deactivation of the catalytic sites.

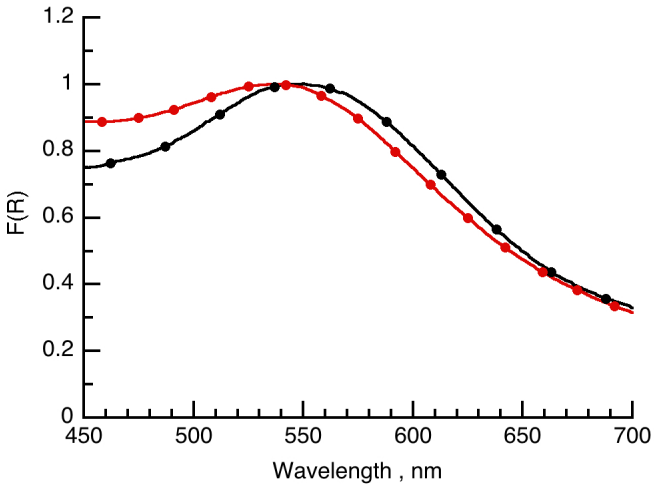

Figure 5.15: Normalized diffuse reflectance spectra of mesoporous AuNP@Nb_2O_5 freshly made (***Black***) and after thermal reaction, 120°C (*Red*).

Storage time dependence of the catalytic activity for plasmon-mediated reactions was also evaluated. In the case of AuNP@Nb_2O_5 (HY-340), the percent conversion of benzyl chloride decreased from 100 % for a freshly prepared catalyst to approximately 60 % and 13 % for reactions performed utilizing the same catalyst batch upon 1 week and 2 weeks aging, respectively (see Figure 5.16).

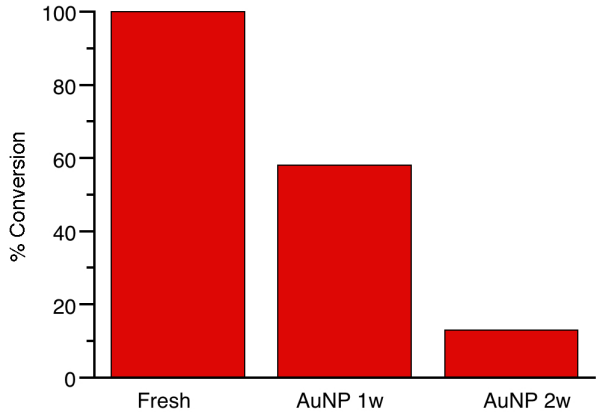

Figure 5.16: % Conversion of benzyl chloride with AuNP@Nb_2O_5 (HY-340) catalyst with storage time -under air and at room temperature- upon reaction under green LED irradiation: freshly made catalyst, after 1 week (AuNP 1w) and 2 weeks (AuNP 2w).

A slower decay in activity was observed for AuNP@mesoNb_2O_5 for which 38 % benzyl chloride conversion was still retained after five weeks storage time (Figure 5.17). The DR spectra of freshly prepared AuNP@Nb_2O_5 catalyst and the same catalyst 2 weeks after preparation remained virtually unchanged.

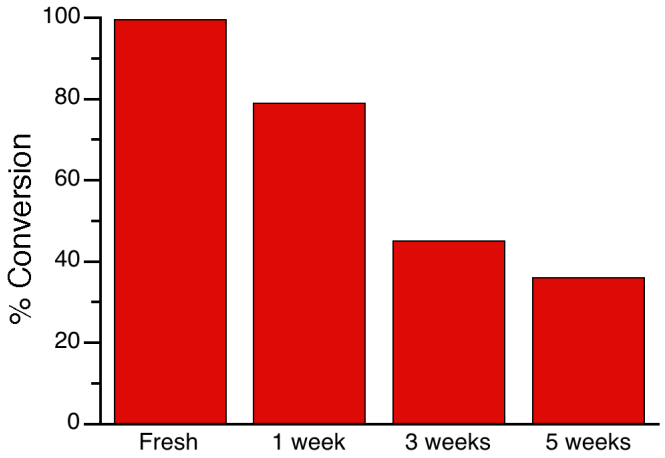

Figure 5.17: % Conversion of benzyl chloride with AuNP@Nb_2O_5 (mesoporous) catalyst with storage time -under air and at room temperature- upon reaction under green LED irradiation: freshly made catalyst, after 1 week (AuNP 1w) and 2 weeks (AuNP 2w).

In 2011, Nakashima *et al.*, proposed the use of hydrated niobic acid (Nb_2O_5 nH_2O) as heterogeneous Lewis acid catalyst proving that in spite the presence of water molecules some of the NbO_4-H_2O adducts formed could still behave as active Lewis sites.[37] However, the decrease in catalytic activity with storage time, and the Lewis acid affinity for water molecules proposed by Nakashima, suggest that the deactivation of the catalysts with storage time could be due to the adsorption of water molecules, making the catalyst less active when used after long storage periods. This hypothesis would also explain the fact that the mesoporous AuNP@Nb_2O_5 catalyst remained active for longer storage times ($>$ 5 weeks) compared to its amorphous analogue since the acid sites located inside the channels of the mesoporous materials are less accessible to water.

Lyophilization of a fully deactivated catalyst for 8 hours was performed to establish if Lewis acid deactivation was due to water adsorption, and the possibility to recover the lost catalytic activity by removing adsorbed water. Further analysis of the DR spectra (Figure 5.18) showed that the blue shift in the absorption maxima upon complete catalyst deactivation (by 5 week storage) was reversed by lyophilization; the DR spectra of the lyophilized sample matches the one corresponding to the freshly prepared catalyst. Additionally, the catalytic activity of the lyophilized sample was tested resulting in 18 % conversion compared to the null percentage before lyophilization indicating partial recovery of the catalytic activity. Heating of the catalyst under vacuum was also considered for water removal; however, complete catalyst deactivation was maintained making lyophilization the best method for reactivation.

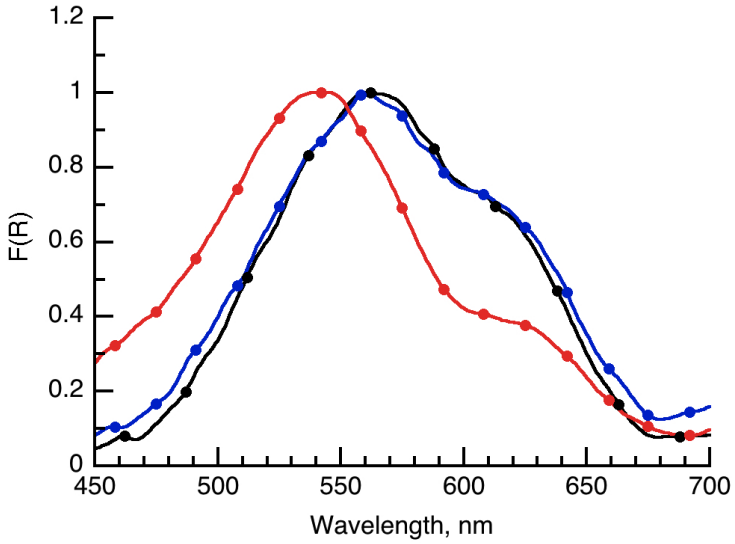

Figure 5.18: Normalized diffuse reflectance spectra of AuNP@b_2O_5 (HY-340) (***Black***) freshly prepared, (*Red*) fully deactivated and (*Blue*) lyophilized.

Finally, the partial reactivation of the plasmon-mediated catalytic activity of a 5-week-old lyophilized sample of amorphous AuNP@Nb_2O_5 (HY-340) was tested giving 18 % benzyl chloride conversion in 2 hours compared to the 100 % and 0 % observed for the freshly made and deactivated catalyst, respectively. The fact that the reactivation of the catalyst is incomplete indicates that either extended lyophilization times are needed or that the deactivation is partially reversible. Future efforts will be made in order to study in depth the deactivation/reactivation process of these catalysts and the optimization of the storage conditions.

5.4 Conclusions

The capabilities of these new hybrid materials to behave as catalysts were tested. The Friedel-Crafts alkylation of anisole by benzyl chloride was catalyzed by AuNPs supported Nb_2O_5 composites. This work serves as a proof of concept indicating that the localized plasmon heating effect by means of green light irradiation can in fact act as an alternative heat source and allows for this reaction to occur at lower temperatures. The localized heating produced *via* plasmon excitation permitted the acid catalyzed reaction to occur -at the Lewis acid sites on the Nb_2O_5 support- at 80°C while thermal-dark reactions using a conventional heat source, required temperatures of 120°C or higher. On the other hand, the deactivation of the studied catalysts with storage time would likely be due to water adsorption and it is partially reversible upon water removal by lyophilisation. In this chapter, the capabilities of the new catalyst were tested obtaining materials that granted water tolerance, spatial and temporal control offering at the same time the possibility to easily control Brønsted and Lewis acid sites, *i.e.* by the use of NaCl.

REFERENCES

[1] R Jose, V Thavasi, and S Ramakrishna. Metal oxides for dye-sensitized solar cells. *Journal of the American Ceramic Society*, 92:289–301, 2009.

[2] AG Prado, LB Bolzon, CP Pedroso, AO Moura, and LL Costa. Nb_2O_5 as efficient and recyclable photocatalyst for indigo carmine degradation. *Applied Catalysis B: Environmental*, 82:219–224, 2008.

[3] SB Ficarro, JR Parikh, NC Blank, and JA Marto. Niobium (V) oxide: Application to phosphoproteomics. *Analytical Chemistry*, 80:4606–4613, 2008.

[4] P Periasamy, HL Guthrey ans AI Abdulagatov PF Ndione, JJ Berry, DS Ginley, SM George, PA Parrilla, and RP O'Hayre. Metal-insulator-metal diodes: Role of the insulator layer on the rectification performance. *Angewandte Chemie International Edition*, 25:1301–1308, 2013.

[5] H Schafer, R Gruehn, and F Schulte. The modifications of niobium pentoxide. *Angewandte Chemie International Edition*, 5:40–52, 1966.

[6] C Nico, T Monteiro, and MPF Graca. Niobium oxides and niobates physical properties: Review and prospects. *Progress in Materials Science*, 80:1–37, 2016.

[7] I Nowak and M Ziolek. Niobium compounds: Preparation, characterization and applications in heterogeneous catalysis. *Chemical Reviews*, 99:3203–3624, 1999.

[8] I Nowak and M Ziolek. Niobium compounds: Preparation, characterization and applications in heterogeneous catalysis. *Chemical Reviews*, 99:3203–3624, 1999.

[9] EI Ko and JG Wiessman. Structures of niobium pentoxide and their implications on chemical behavior. *Catalysis Today*, 8:27–36, 1990.

[10] DAB de Filho, DW Franco, PPA Filho, and OL Alves. Niobia films: surface morphology, surface analysis, photoelectrochemical properties and crystallization process. *Journal of Materials Science*, 33:2607–2616, 1998.

[11] JW Schultze and MM Lohrengel. Stability, reactivity and breakdown of passive films. problems of recent and future research. *Electrochimica Acta*, 45:2499–2513, 2000.

[12] R Brayanera and F Bozon-Verduraz. Nb_2O_5 prepared by soft chemical routes: morphology, structure, defects and quantum size effect. *Physical Chemistry Chemical Physics*, 5:1457–1466, 2003.

[13] MRN Soares, S Leite, C Nico, M Peres, AJS Fernandes, MPF Graca, M Matos, R Monteiro, T Monteiro, and FM Costa. Effect of processing method on physical properties of Nb_2O_5. *Journal of the European Ceramic Society*, 31:501–506, 2011.

[14] T Iizuka, K Ogasawara, and K Tanabe. Acidic and catalytic properties of niobium pentoxide. *Bulletin of the Chemical Society of Japan*, 56:2927–2931, 1983.

[15] Y Zhao, X Zhou, L Xe, and SCE Tsang. Nanostructured (Nb_2O_5) catalysts. *Nano Reviews*, 3:17631–17641, 2012.

[16] ICMS Santos, LH Loureiro, MFP Silva, and AMV Cavaleiro. Studies on the hydrothermal synthesis of niobium oxides. *Polyhedron*, 21:2009–2015, 2002.

[17] D Zhao, Q Huo, J Feng, BF Chmelka, and GD Stucky. Nonionic triblock and star diblock copolymer and oligomeric surfactant syntheses of highly ordered, hydrothermally stable, mesoporous silica structures. *Journal of the American Chemical Society*, 120:6024–6036, 1997.

[18] J Yi and M Kruk. Pluronic-P123-templated synthesis of slica with cubic Ia3d structure in the presence of micelle swelling agent. *Langmuir*, 31:7623–7632, 2015.

[19] P Yang, D Zhao, DI Margolese, BF Chmelka, and GD Stucky. Block copolymer templating syntheses of mesoporous metal oxides with large ordering lengths and semicrystalline framework. *Chemistry of Materials*, 11:2813–2826, 1999.

[20] E Wada M Kitano K Yamamoto K Nakajima, S Hayashid, and M Hara. Synthesis of niobium-doped titanate as solid acid catalysts. *Catalysis Science and Technology*, 6:4832–4839, 2016.

[21] T Shishido, T Kitano, K Teramura, and T Tanaka. Bronsted acid generation over alumina-supported niobia by calcination at 1173K. *Catalysis Letters*, 129:383–386, 2009.

[22] T Uchijima. SMSI effect in some reducible oxides including niobia. *Catalysis Today*, 28:105–117, 1996.

[23] Rakesh, S Ananda, NMM Gowda, and KR Raksha. Synthesis of niobium doped ZnO nanoparticles by electrochemical method: Photodegradation of indigo carmine dye and antibacterial study. *Advances in Nanoparticles*, 3:133–147, 2014.

[24] YN Tan, CL Wong, and AR Mohamed. An overview on the photocatalytic

activity of nano-doped TiO_2 in the degradation of organic pollutants. *ISRN Materials Science*, Article ID 261219:1–18, 2011.

[25] Z Chen, T Iizuka, and K Tanabe. Niobic acid as an efficient catalyst for vapor phase esterification of ethyl alcohol with acetic acid. *Chemical Letters*, 13:1085–1088, 1984.

[26] IMI de Sairre, ES Bronze-Uhle, and PM Donate. Niobium (V) oxide: A new and efficient catalyst for the transesterification of β-keto esters. *Tetrahedron Letters*, 46:2705–2708, 2005.

[27] RHH Smits, K Seshan, and JRH Ross. The selective dehydrogenation of propane over niobium pentoxide. *Journal of the Chemical Society, Chemical Communications*, 0:558–559, 1991.

[28] B Michalkiewicz, J Srenscek-Nazzal, P Tabero, B Grzmil, and U Narkiewicz. Selective methane oxidation to formaldehyde using polymorphic T-, M- and H-forms of niobium(V) oxide as catalysts. *Chemical Papers*, 62:106–113, 2008.

[29] T Kushimoto, Y Ozawa, A Baba, and H Matsuda. Nioum compound catalyst for polycondensation reaction to form polyethylene terephthalate(PET). *Catalysis Today*, 16:571–578, 1993.

[30] C Friedel and JM Crafts. Sur une nouvelle methode generale de synthese d'hydrocarbures, d'acetones, etc. *Comptes Rendus Chimie*, 84:1392–1395, 1877.

[31] K Bachari and O Cherifi. Benzylation of benzene and other aromatics by benzyl chloride over copper-mesoporous molecular sieves materials. *Catalysis Communications*, 7:926–930, 2006.

[32] K BAchari and O Cherifi. Benzylation of aromatics on tin-containing mesoporous materials. *Applied Catalysis A: General*, 319:259–266, 2007.

[33] Y Ma, QL Wang, W Jian, and B Zuo. Friedel-Crafts acylation of anisole over zeolite catalysts. *Applied Catalysis A: General*, 165:199–206, 1997.

[34] M Rueping and BJ Nachtsheim. A review of new developments in the friedel-Crafts alkylation - from green chemistry to asymmetric catalysis. *Beilstein Journal of Organic Chemistry*, 6(6), 2010.

[35] MHC De la Cruz, JFC Da Silva, and ER Lachter. Liquid phase benzylation of aromatic compounds with benzyl alcohol catalyzed by niobium phosphate. *Applied Catalysis A: General*, 245:377–382, 2003.

[36] MHC De la Cruz, JFC Da Silva, and ER Lachter. Synthesis of pharmaceutical intermediates by toluene benzylation over heteropoly acids on different supports. *Journal of Natural Gas Chemistry*, 16:186–192, 2007.

[37] K Nakajima, K Baba, R Ryouhei, M Kitano, JN Kondo, S Hayashi, and M Hara. Niobium oxide as a heterogeneous catalyst with water-tolerant Lewis acid sites. *The Journal of the American Chemical Society*, 133:4224–3052, 2011.

[38] M Moraes, W de SF Pinto, WA González, LMPM Carmo, NMR Pastura, and ER Lachter. Benzylation of toluene and anisole by benzyl alcohol catalysed by niobic acid: Influence of pretreatment temperature in the catalytic activity of niobic acid. *Applied Catalysis A: General*, 138:L7–L12, 2007.

[39] AO Ibhadon and P Fitzpatrick. Heterogeneous photocatalysts: Recent advances and applications. *Catalysis*, 3:189–218, 2013.

[40] JC Scaiano and K Stamplecoskie. Can surface plasmon fields provide a new way to photosensitize organic photoreactions? from designer nanoparticles to custom applications. *Journal of the American Chemical Society*, 4:1177–1187, 2013.

[41] C Fasciani, CJB Alejo, M Grenier, JC Netto-Ferreira, and JC Scaiano. High-temperature organic reactions at room temperature using plasmon excitation: Decomposition of dicumyl peroxide. *Organic Letters*, 13:204–207, 2011.

[42] HL Tu, YS Lin, HY Lin, Y Hung, LW Lo, YF Chen, and CY Mou. In vitro studies of functionalized mesoporous silica nanoparticles for photodynamic therapy. *Advanced Materials*, 21:172–177, 2009.

[43] P Christopher, H Xin, and S Linic. Visible-light-enhanced catalytic oxidation reactions on plasmonic silver nanostructures. *Nature Chemistry*, 3:467–472, 2011.

[44] S Navalon, R Martin, M Alvaro, and H García. Gold on diamond nanoparticles as a highly efficient Fenton catalyst. *Angewandte Chemie International Edition*, 49:8403–8407, 2010.

[45] J Qiu and WD Wei. Surface plasmon-mediated photothermal chemistry. *Journal of Physical Chemistry C*, 118:20735–20749, 2014.

[46] ML Marin, GL Hallet-Tapley, S Impellizzeri, C Fasciani, S Simoncelli, JC Netto-Fereira, and JC Scaiano. Synthesis, acid properties and catalysis by niobium oxide nanostructured materials. *Catalysis Science and Technology*, 4:3044–3052, 2014.

[47] ML Marin, GL Hallet-Tapley, S Impellizzeri, C Fasciani, S Simoncelli, JC Netto-Fereira, and JC Scaiano. Mechanistic insights into the Nb_2O_5 catalyzed in situ condensation of a fluorescent halochromic assembly. *Catalysis Science and Technology*, 5:169–175, 2015.

[48] ML Marin, GL Hallett-Tapley, S Impellizzeri, C Fasciani, S Simoncelli, JC Netto-Ferreira, and JC Scaiano. Synthesis, acid properties and catalysis by niobium oxide nanostructured materials. *Catalysis Science and Technology*, 4:3044–3052, 2014.

[49] T Mitsudome, Y Mikami, H Funai, T Mizugaki, K Jitsukawa, and K Kaneda. Oxidant-free alcohol dehydrogenation using a reusable hydrotalcite-supported silver nanoparticle catalyst. *Angewandte Chemie International Edition*, 47:138–141, 2008.

[50] EP Parry. An infrared study of pyridine adsorbed on acidic solids. Characterization of surface acidity. *Journal of Catalysis*, 2:371–379, 1963.

[51] CA Emis. Determination of integrated molar extinction coefficients for infrared absorption bands of pyridine adsorbed on solid acid catalysts. *Journal of Catalysis*, 141:347–354, 1993.

[52] T Murayama, W Ueda, and M Haruta. Deposition of gold nanoparticles on niobium pentoxide with different crystal structures for room-temperature carbon monoxide oxidation. *Chem. Cat. Chem.*, 8:2620–2624, 2016.

[53] A Primo, A Corma, and H García. Titania supported gold nanoparticles as photocatalyst. *Physical Chemistry Chemical Physics*, 13:886–910, 2011.

[54] ILC Buurmans and BM Weckhuysen. Heterogeneities of individual catalyst particles in space and time as monitored by spectroscopy. *Nature Chemistry*, 4:873–886, 2012.

[55] PVJ Kamat. Photophysical, photochemical and photocatalytic aspects of metal nanoparticles. *Journal of Physical Chemistry B*, 106:7729–7744, 2002.

[56] Z Ma and S Dai. Development of novel supported gold catalysts: A materials perspective. *Nano Research*, 4:3–32, 2011.

[57] K Watanabe, D Menzel, N Nilus, and HJ Freund. Photochemistry on metal nanoparticles. *Chemical Reviews*, 106:4301–4320, 2006.

[58] K Heo, C Miesch, T Emrick, and RC Hayward. Thermally reversible aggregation of gold nanoparticles in polymer nanocomposites through hydrogen bonding. *Nano Letters*, 13:5297–5302, 2013.

[59] PK Jain, W Huang, and MA El-Sayed. On the universal scaling behavior of the distance decay of plasmon coupling in metal nanoparticle pairs: A plasmon ruler equation. *Nano Letters*, 7:2080–2088, 2007.

[60] Z Liu and MJ Jiang. Reversible aggregation of gold nanoparticles driven by inclusion complexation. *Journal of Materials Chemistry*, 17:4249–4254, 2007.

[61] P Peng, A Hu, and Y Zhou. Laser sintering of silver nanoparticle thin films: Microstructure and optical properties. *Applied Physics A*, 108:685–691, 2012.

[62] A Dimitrowicz, P Jamroz, K Greda, P Nowak, M Nyk, and M Pohl. The influence of stabilizers on the production of gold nanoparticles by direct current atmospheric pressure glow microdischarge generated in contact with liquid flowing cathode. *Journal of Nanoparticle Research*, 17:185, 2015.

Chapter 6

Conclusions and Future Directions

6.1 Conclusions

This thesis has explored the various plasmon-mediated photothermal phenomena generated by the localized plasmon heating effect -activated by plasmon excitation *via* visible and/or NIR irradiation- following the nanofabrication of applicable devices. For each one of the systems developed in this thesis the localized surface plasmon heating effect proved to play an important role and potently contribute to these systems by either granting key properties that improve their overall function or by conferring what is needed for them to actually be applicable. In addition, this thesis has contributed to the field of nanofabrication of applicable devices by combining simple synthetic procedures that have allowed the successful combination of plasmonic properties of gold nanostructures with those of mesoporous materials, polymer matrices and catalytic Nb_2O_5 supports. Even if at a first glance the localized surface plasmon heating effect seems to be a simple and easy to understand effect, in reality the SPR is rather complex and the proper understanding of the complexity of their properties and behavior is what allows it to be compatible with numerous materials.

Localized Surface Plasmon in Drug Delivery

We demonstrated that plasmon excitation can be used to control and modify the dynamic of cargo diffusion from mesoporous MCM-41 by means of the localized surface plasmon heating effect that influences -through heat release- the guests and solvents within the channels of the material conferring the designed drug delivery systems with spatial and temporal control (Chapter 2). Moreover, in Chapter 3 we proved that the start of the release from gated systems endowed with thermo-responsive gates -enabling "zero" premature release- can also be successfully controlled through plasmon excitation (see Figure 6.1). Furthermore, we demonstrated that the plasmonic

properties of anisotropic gold nanorods (AuNRs) and isotropic spherical nanoparticles can be combined to provide the delivery systems with a wavelength-controlled delivery feature giving rise to various rates of release and system activation modes. The incorporation of gold nanostructures and the visible and NIR light activation components promises to expand the versatility of these systems to biological samples in which damage would be incurred by using UV light. Furthermore, the main contribution granted by the anisotropy of gold nanorods is the above mentioned NIR activation component that broadens the applicability of the drug delivery systems by enabling their use in biological samples that would require deeper light penetration.

The main contribution of this part of the research was to report for the first time that plasmon excitation can be used to control both the start of the release process and the rates of cargo delivery through excitation of either the longitudinal or transverse plasmon of gold nanorods and/or the single plasmon band of gold nanoparticles.

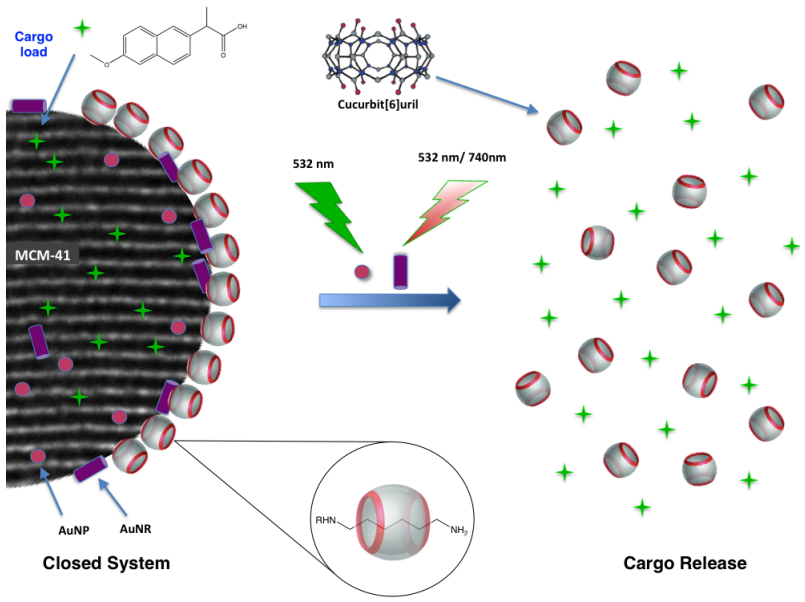

Figure 6.1: Graphical abstracts corresponding to plasmon-mediated drug delivery from gated MCM-41 systems.

Localized Surface Plasmon in Patterning Applications

Chapter 4 contributed to the development of a simple method for the embedment of gold nanorods in various polymeric matrices and the further photoactivated self-assembly of gold nanorods (AuNRs) to create robust patterns that persist for extended periods of time. The possibility of orienting AuNRs by selectively exciting the longitudinal plasmon band without incurring in ablation -keeping their size and shape unmodified- was achieved. Further exploration of the phenomenon of photoactivated orientation of gold nanorods (AuNRs) under red light activation allowed us to conclude that the nature of the polymer softening phenomenon is driven by the localized plasmon heating effect. Figure 6.2 stands as a proof of how feasible is to use this phenomenon for patterning applications.

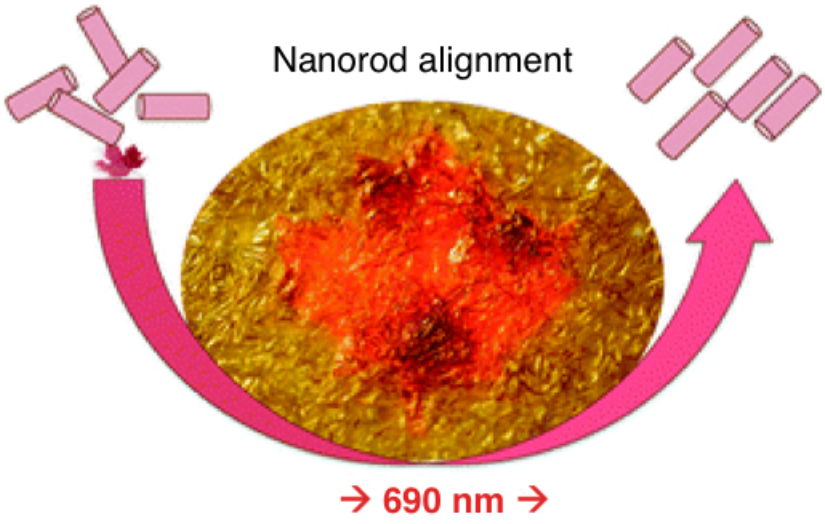

Figure 6.2: Graphical abstracts corresponding to photo-patterning by plasmon excitation of AuNRs embedded in a polymer matrix.

Localized Surface Plasmon as an Alternative Heat Source for Friedel-Crafts Alkylation at Lower Bulk Temperatures.

Chapter 5 served as a proof of concept demonstrating that, under irradiation, the localized plasmon heating effect of AuNPs can be used as an alternative heat source to perform the Nb_2O_5 catalyzed Friedel-Craft alkylation reaction of anisol by benzyl chloride at much lower bulk temperatures compared to its dark (thermal) counterpart. Moreover, we offered some insight in the deactivation of the catalyst with storage time which is most likely due to the deactivation by water adsorption that proved to be partially reversible upon water removal by lyophilization. The capabilities of the new catalysts were tested obtaining materials that granted spatial and temporal control and a degree of water tolerance that is superior to other commonly used solid acids -such as $AlCl_3$- while offering at the same time the possibility to easily control Brønsted and Lewis acid sites, *i.e.* by the use of NaCl.

6.2 Future Directions

The findings that are central to this dissertation provide a natural guide for future research in each one of the topics of study. Future work will be aimed at extending the ideas explored herein to gain additional important information and to address and develop several other relevant systems and applications that can benefit from plasmon-mediated photothermal phenomena. Furthermore, it would be interesting to try plasmonic nanostructures made of other metals like silver and copper that could be more convenient, depending on the application to be developed and the problem to be solved.

6.2.1 Drug Delivery Systems

Biological Assays

It will be important to gather information regarding the biocompatibility of the drug delivery systems developed herein with various biological environments through *in vitro* release studies of drugs and dyes other than the test drug -naproxen- used in this thesis as well as performing an evaluation of the cytotoxicity and further testing of the *in vivo* bio-compatibility, bio-distribution and possibility of targeting.

The cytotoxicity -degree to which something is toxic to living cells- can be evaluated through various assays. While several methods -including microscopic analysis and automated cell counting- exist to determine the viability and proliferation of cells in response to stimuli, indirect methods -based on colorimetric and fluorometric reagents- are currently the most attractive alternatives since these assays are rapid and easy to perform.

The MTT assay developed by Mossman[1] is one of the most commonly used methods to determine live cell number because of its convenience and safe characteristics. It is a colorimetric assay based on the enzymatic reduction of 3-(4,5-dimethylthiazol-2-yl)-2, 5-diphenyltetrazolium bromide (MTT) -originally yellow in color- into a purple formazan crystal in live cells (see Figure 6.3).

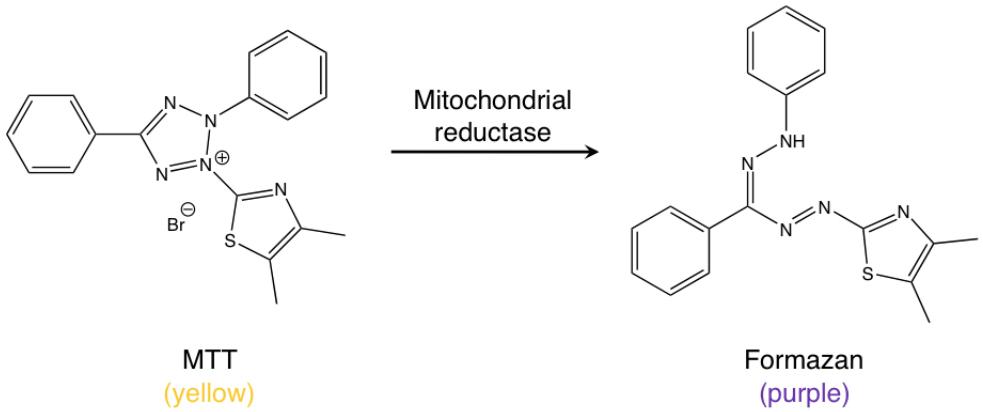

Figure 6.3: Diagram ilustrating the MTT method for cytotoxicity determination.

The formazan can then be solubilized producing a colorimetric signal at 570 nm at a concentration proportional to the cell number and activity.

This method will be useful to assess the cytotoxicity of the empty carriers besides evaluating the possible toxic effects of the cargo-loaded drug delivery systems on primary cell cultures. Also, MTT will be suitable to determine the growth factor activity and to evaluate the cytostatic potential of the compounds that might want to be loaded.[2]

As previously reported, studies of the bio-compatibility and bio-distribution for mesoporous materials can be performed through the administration of the system by injecting doses that range from 5mg/Kg to 50mg/Kg of body weight in mice.[3]

The development of target specificity for the drug delivery systems presented in this thesis will be considered. In the case of mesoporous materials, the selectivity toward specific targets can be modeled by surface functionalization of various organic molecules *via* covalent bonding. A wide variety of targeting agents are currently available and are usually based on organic molecules that already exist in the biological environment, hence, are bio-degradable and generally non toxic.[4]

Cargo Delivery for Other Applications

Mesoporous materials, such as MCM-41 have been used as cargo carriers in a multitude of environments so it would be very useful to implement our plasmon-mediated delivery systems for applications other than drug delivery in biological environments.

One possible example is the use of these mesoporous systems as pesticide carriers. Pesticides are widely used to kill insects, fungi, bacteria, weeds and other organisms bringing great benefits to society.[5] However, when pesticides are applied, more than 90% of their totality gets lost in the environment making it unable to reach the area that requires pest control increasing costs and leading to environmental pollution.[6] It is because of the reasons presented above that improving the delivery of pesticides has become a very active field of research in the past couple of decades. Furthermore, in the last decade the development of nanocarriers endowed with properties that facilitate the controlled release of agrochemicals has gained considerable attention.[7, 8, 9] Similar to the case of mesoporous materials for drug delivery in biological systems the development of controlled-release formulations of pesticides are considered a suitable alternative for delivering active ingredients at a desired rate (see Figure 6.4).[10, 11, 12, 13]

The light controlled delivery achieved by the systems developed in this thesis will be considered for testing as pesticide carriers and delivery systems. Because of their visible/NIR activation components it would be interesting to test using sunlight as the activation light source.

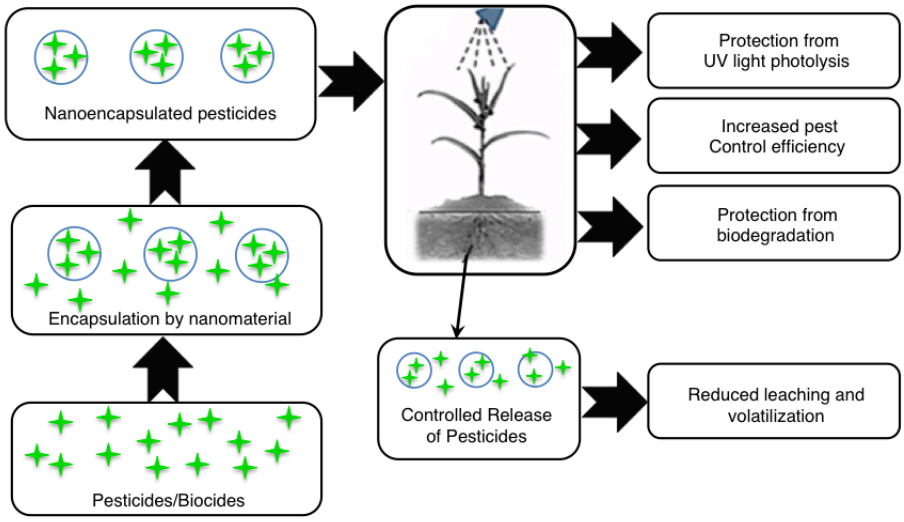

Figure 6.4: Diagram exemplifying the use of nanocarriers for pesticide encapsulation and delivery. Adapted with permission from ref. [9]. Copyright (2017) American Chemical Society.

6.2.2 Mesoporous AuNP@Nb_2O_5 Based Catalysts

The AuNP@Nb_2O_5 catalysts developed herein serve as a proof of concept that the localized surface plasmon heating effect can be used as an alternative heat source allowing to perform Friedel-Crafts reactions at lower temperatures. As future directions on this matter a more in depth study focused on the nature of the deactivation and partial reactivation of the catalytic acid sites of the Nb_2O_5 based catalysts will be considered. Furthermore, it is of extreme importance to be able to achieve a finer tuning of the Lewis to Brønsted acid proportions and strengths in order to optimize catalytic activity of Nb_2O_5 catalysts.

In 2010, Maclachlan et al. proposed the synthesis of free-standing mesoporous silica films with tunable chiral nematic structure using cellulose nanocrystals (CNCs) as template.[14] Upon CNCs removal, photonic mesoporous inorganic solids that possess a characteristic twisting repeating unit -called pitch- were obtained in the form of iridescent films. By modifying the CNCs/silica precursor ratio it was possible to obtain

materials with different pitch which translated into materials with different optical properties. Interestingly, their research was further expanded to other materials such as Nb_2O_5 (see Figure 6.5).

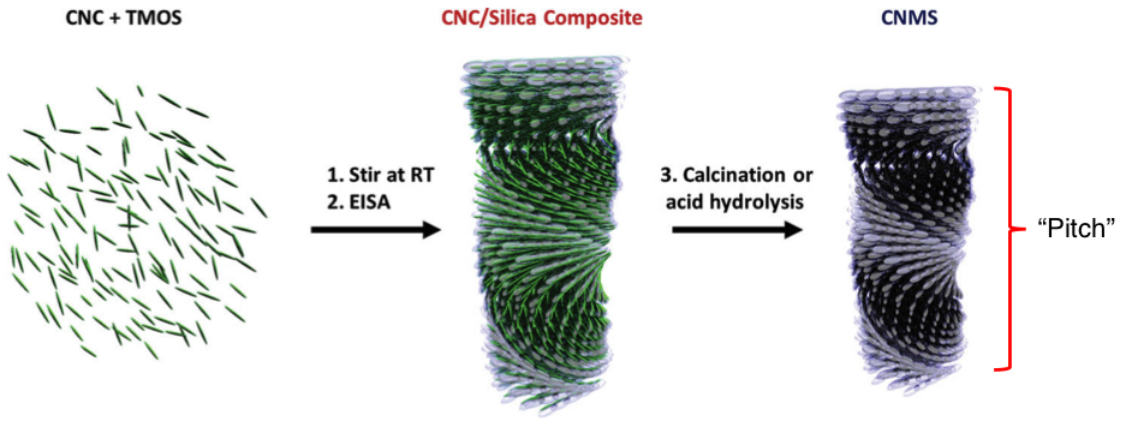

Figure 6.5: Diagram exemplifying the synthesis of chiral-nematic mesoporous silica materials. Reproduced with permission from ref.[15]. Copyright (2017) Wiley.

It is well known that for niobium oxide based materials the precise arrangement of atoms on facets, edges and corners may be very different from the bulk giving in most cases unique activity and selectivity towards chemical reactions, which is in turn relate to the Lewis acid to Brønsted acid ratio and their respective strengths.[16]

Due to the very early stages in which the development of chiral-nematic mesoporous Nb_2O_5 materials is, little to no information with respect to their structure and properties has been reported. This poses as a convenient platform to study these new materials, obtain more detailed information regarding its structural properties, and at the same time, test the possibility of developing -through pitch tuning- a more precise way of adjusting Lewis to Brønsted acid site ratios to optimize catalytic activity.

Since the incorporation of gold nanoparticles on Nb_2O_5 proved to be successful during this dissertation and the localized surface plasmon heating effect allowed to

perform a Nb_2O_5 catalyzed Friedel-Craft reaction at lower bulk temperatures the above mentioned chiral-nematic materials will be tested as catalysts upon the incorporation of AuNPs in order to establish the possibility of performing reactions -that commonly require elevated temperatures- at lower bulk temperatures but most importantly to determine the application scope of the chiral-nematic mesoporous Nb_2O_5 materials and gather structural information.

6.3 Claims to Original Research

1. Study that demonstrates that the localized plasmon heating effect can be effectively used to modify the dynamic of cargo release from supramolecular systems.

2. Study leading to the nanofabrication of plasmon-mediated spatio-temporal controlled mesoporous cargo delivery systems where rates of delivery can be controlled by visible light.

3. Study leading to the nanofabrication of plasmon-mediated spatio-temporal controlled and wavelegnth-controlled mesoporous gated cargo delivery systems.

4. Study leading to the nanofabrication of gated drug delivery systems with a "zero" premature release feature, in which the control of both the start of the release and the rates of cargo delivery is possible by means of visible and NIR irradiation.

5. Development of a patterning method based on the NIR plasmon-mediated self assembly of gold nanorods in polymer matrices that give rise to robust and persistent patterns.

6. Study leading to the development of AuNP@Nb_2O_5 based catalysts for the plasmon-mediated catalyzed Friedel-Craft alkylation of anisole by benzyl chloride at lower bulk temperatures.

6.4 Publications Resulting from Work Presented in This Thesis

(i) DT Marquez, AI Carrillo and JC Scaiano. Plasmon Excitation of Supported Gold Nanoparticles Can Control Molecular Release from Supramolecular Systems. *Langmuir*, **2013**, 29, 10521-10528.

(ii) DT Marquez and JC Scaiano. Plasmon Induced Self-Assembly of Gold Nanorods in Polymer Films. *Chemical Communications*, **2015**, 51, 1911-1913.

(iii) DT Marquez and JC Scaiano. Visible and Near-Infrared Plasmon-Mediated Molecular Release from Cucurbit[6]uril Mesoporous Gated Systems. *Langmuir*, **2016**, 32, 13764-13770.

(iv) CG Dos Santos, DT Marquez, CL Crites, JC Netto-Ferreira and J.C. Scaiano. Plasmon Heating Mediated Friedel-Crafts Alkylation of Anisole using Supported AuNP@Nb_2O_5 Catalysts. *Tetrahedron Letters*, **2017**, 58, 427-431.

6.5 Publications Resulting from Work Not Presented in This Thesis

(i) NC Angeluzzi, M Munoz, DT Marquez, MS Baptista, AM Edwards, EI Alarcon and JC Scaiano. Silica Nanoreactors from Silylated Riboflavin for Efficient Singlet Oxygen Delivery. *Journal of Materials Chemistry B*, **2014**, 2, 4221-4225.

(ii) AM Alshehri, KLN Deepak, DT Marquez, S Desgreniers, and VR Bhardwaj. Localized Nanoclusters Formation in PDMS upon Irradiation with Femtosecond Laser. *Optical Materials Express*, **2015**, 5, 858-869.

(iii) DLN Kallepalli, AM Alshehri, DT Marquez,L Andrzejewski, JC Scaiano and R Bhardwaj. Ultra-high Density Optical Data Storage in Common Transparent Plastics. *Scientific Reports*, **2016**, 6, doi:10.1038/srep26163.

(iV) C Lazurko, N Marina, DT Marquez, S Kilty and JC Scaiano. Biofilm Prevention and Inhibition Using Sweetener-Coated Silver Nanostructures, *in progress.*

REFERENCES

[1] T Mosmann. Rapid colorimetric assay for cellular growth and survival: application to proliferation and cytotoxicity assays. *Journal of Immunological Methods*, 65:55–63, 1983.

[2] P Banks P Brescia. Quantifying cytotoxicity of thiostrepton on mesothelioma cells using MTT assay and the epoch microplate spectrophotometer, http://www.biotek.com/resources/articles/quontification-cell-viability-epoch.html, [Accessed: Jan 2017].

[3] C Bharti, U Nagaich, AK Pal, and N Gulati. Mesoporous silica nanoparticles in target drug delivery system: A review. *International Journal of Pharmaceutical Investigation*, 5:124–133, 2015.

[4] J Rytkonen, R Miettinen, M Kaasalainen, V Lehto, J Salonen, and A Narvanen. Functionalization of mesoporous silicon nanoparticles for targeting and bioimaging purposes. *Journal of Nanomaterials*, page doi:10.1155/2012/896562., 2012.

[5] M Enserink, PJ Hines, SN Vignieri, NS Wigginton, and JS Yeston. The pesticide paradox. *Science*, 16:728–729, 2013.

[6] V Ghormade, MV Deshpande, and KM Pakinikar. Perspectives for nanobiotechnology enabled protection and nutrition of plants. *Biotechnology Advances*, 29:792–803, 2011.

[7] A Gogos, K Knauer, and TD Bucheli. Nanomaterials in plant protection and fertilization: Current state, foreseen applications, and research priorities. *Journal of Agricultural Food Chemistry*, 60:9781–9792, 2012.

[8] M Kah, S Beulke, K Tiede, and T Hofmann. Nanopesticides: State of knowledge, environmental fate, and exposure modeling. *Critical Reviews in Environmental Science and Technology*, 43:1823–1867, 2013.

[9] M Nuruzzaman, MM Rahman, Y Liu, and R Naidu. Nanoencapsulation, nanoguard for pesticides: A new window for safe application. *Journal of Agricultural Food Chemistry*, 64:1447–1483, 2016.

[10] EVR Campos, JL de Oliveira, and LF Fraceto. Applications of controlled release systems for fungicides, herbicides, acaricides, nutrients, and plant growth hormones: A review. *Advanced Science, Engineering and Medicine*, 6:373–387, 2014.

[11] MG Mogul, H Akin, N Hasirci, DJ Trantolo, JD Gresser, and DL Wise. Controlled release of biologically active agents for purposes of agricultural crop management. *Resources, Conservation and Recycling*, 16:289–320, 1996.

[12] EVR Campos, JL de Oliveira, LF Fraceto, and B Singh. Polysaccharides as safer release systems for agrochemicals. *Agronomy for Sustainable Development*, 34:47–66, 2015.

[13] L Cao, H Zhang, C Cao, J Zhang, F Li, and Q Huang. Quaternized chitosan-capped mesoporous silica nanoparticles as nanocarriers for controlled pesticide release. *Nanomaterials*, 6:1–13, 2016.

[14] KE Shopsowitz WY Hamad JA Kelly, M Giese and MJ MacLachlan. The devel-

opment of chiral nematic mesoporous materials. *Accounts of Chemical Research*, 47:1088–1096, 2014.

[15] KE Shopsowitz, H Qi, WY Hamad, and MJ MacLachlan. Free-standing mesoporous silica films with tunable chiral nematic structures. *Nature*, 468:422–426, 2010.

[16] L Ye Y Zhao, X Zhou and SCE Tsang. Nanostructured niobium oxide catalysts. *Nano Reviews*, 3:17631, 2012.

Appendix A

Appendix: Some Technical Aspects in Mesoporous Materials

A.1 Powder X-ray Diffraction

Diffraction occurs in materials that possess an ordered structure and when the dimension of the diffracting object is comparable to the irradiation wavelength. It is possible to observe a reflection when the Bragg's Law is satisfied:

$$n\lambda = 2dsin\theta \tag{A.1}$$

where θ corresponds to the angle of the incident beam, λ to the wavelength of the beam, d_{hkl} is the reflecting lattice plane (hkl are Miller indices).

In the case of ordered mesoporous materials, such as MCM-41 -used in this thesis- powder X-ray diffraction can be used to assess its porosity. Typical values of Bragg's parameters for MCM-41 are presented on Table A.1.

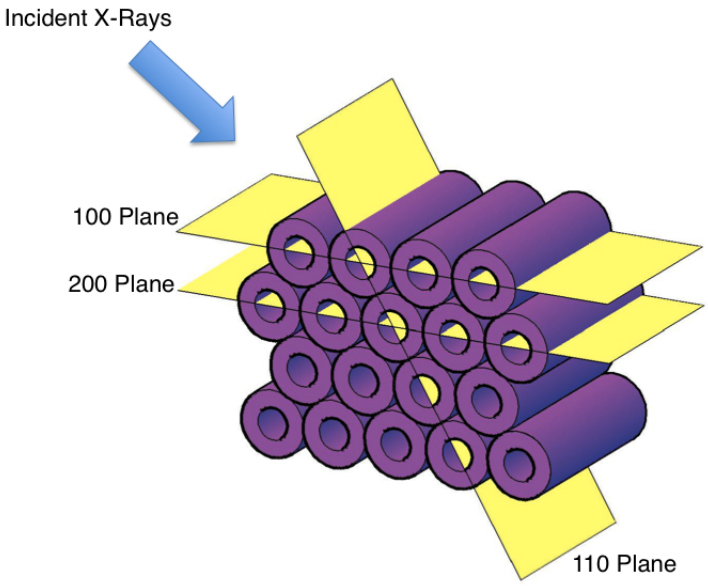

Figure A.1: Diagram of the structural planes of MCM-41 detected by X-Ray diffraction.

Table A.1: Typical Bragg's values obtained from XRD.[1]

2θ (deg)	θ (deg)	λ(nm)	n	d-spacing ($\mathring{A}$)	d/d_{max}
1.87	0.93	1.5418	1	47.3	1
3.25	1.62	1.5418	1	27.2	0.575
3.68	1.84	1.5418	1	23.6	0.49
4.96	2.48	1.5418	1	17.8	0.337

A.2 Nitrogen Adsorption Porosimetry

Nitrogen adsorption porosimetry -a technique based on physical adsorption- is an important technique used to characterize the surface and pore features of solids such as total pore volume and pore size.

This technique involves exposing a carefully prepared solid sample to an inert gas -usually nitrogen- typically at its liquefaction temperature. Sample preparation is often performed through inert gas purging while heating in order to remove weakly adsorbed molecules.

When performing nitrogen adsorption porosimetry, as the pressure is increased the number of molecules physisorbed increases. Initially, a monolayer is formed on the inner surface of the material. As presure increases, multiple layers of molecules are produced on the free surface and on pore walls. Ultimately, the surface is completely covered and pores are filled. The process of physisorption is governed by van der Waals' forces and has low heats of adsorption that allow to characterize solid samples while preserving the structural properties of the materials in study. The energy involved in physical adsorption does not exceed 40-50 kJ/mol meaning that the adsorbed molecules can be easily removed or desorbed by decreasing the pressure or increasing the temperature.

As the pressure is increased, the pores of the material are filled up through capillary condensation, enabling the measurement of pore size and pore volume param-

eters. During an adsorption analysis, the absolute pressure is increased until it approaches the staturation pressure -which corresponds to the vapor pressure of the pure liquid adsorbate- where adsorption is maximized. Then, the pressure is consistently decreased and desorption occurs. The quantity of gas adsorbed and desorbed as a function of the relative pressure are known as adsorption/desorption isotherms.

A.2.1 Types of Adsorption Isotherms

The shape of the adsorption isotherm can be considered as a fingerprint of the texture of the material according to the Brunauer-Emmet-Teller classification. There are 5 types of isotherms as shown in Figure A.2.

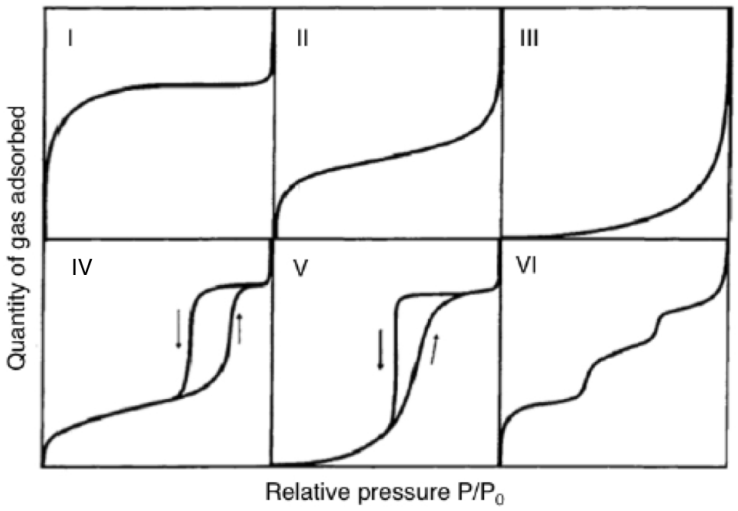

Figure A.2: Types of adsorption/desorption isotherms according to the IUPAC classification.[2] ©IUPAC, 1982.

Type I Adsorption Isotherms

Type I Adsorption isotherms are also called Langmuir adsorption isotherms. It is characterized by having an almost horizontal plateau that occurs at low relative pressures (0.1) and is related to the formation of a monolayer. This type of isotherms are characteristic of solids having pores whose diameter is less than 2 nm.

Type II Adsorption Isotherms

This isotherms present a flat region associated with the formation of a monolayer-followed by a further increase since saturation occurs at much higher relative pressure. This type of isotherms are characteristic of non porous solids or solids that possess large pore diameters (>50 nm).

Type III Adsorption Isotherms

This isotherms don't have a plateau indicating the formation of multilayers without going through monolayer formation. This occurs when the interactions between the adsorbent molecules is stronger than the interactions between the adsorbent and the solid.

Type IV Adsorption Isotherms

Type IV isotherms present a flat region, an increase followed by a second plateau. This indicates multilayer formation that occurs after the initial formation of a monolayer and they presents an hysteresis loop that is associated with the filling and emptying of the pores through capillary condensation. Such is the case of the hybrid mesoporous materials presented in chapter 2 and 3 of in this thesis.

Type V Adsorption Isotherms

Type V isotherms are quite similar to type IV isotherms in terms of the occurrence of capillary condensation and the presence of an hysteresis loop. However, no initial formation of a monolayer is present.

Type VI Isotherms

Type VI Isotherms are a rare case and corresponds to stepwise multilayer adsorption and corresponds to uniform non porous surfaces.

A.2.2 Surface Area

The Brunauer- Emmet-Teller (BET) is the most widely used method for the calculation of the surface area of a material.[3] This method assumes the initial formation of a monolayer (Langmuir's theory) followed by the formation of multilayers of adsorbate, and the following restrictions:

i) The gas molecules are physisorbed on the solid in the form of infinite layers.

ii) The interactions between each layer and between adsorbed molecules are null.

iii) The Langmuir theory of monolayer formation can be applied to each layer separately.

This theory describes the adsorption at high pressure through equation A.2.

$$\frac{P}{Va(P_0 - P)} = \frac{1}{V_m C} + \frac{(C-1)}{V_m C}(\frac{P}{P_0}) \tag{A.2}$$

where Va is the volume of gas adsorbed at equilibrium pressure,

P is the absolute pressure,

P_0 corresponds to the vapour pressure of the pure liquid adsorbate,

C is the isothermal constant,

and Vm is the volume of gas to achieve a monolayer.

The surface area of the material can then be calculated by plotting $P/Va(P\text{-}P_0)$ vs. P/P_0 (Figure A.3), which gives a straight line whose slope A can be used to determine the volume of the monolayer (equation A.3), the BET constant (equation A.4) and the corresponding surface area (equation A.5).

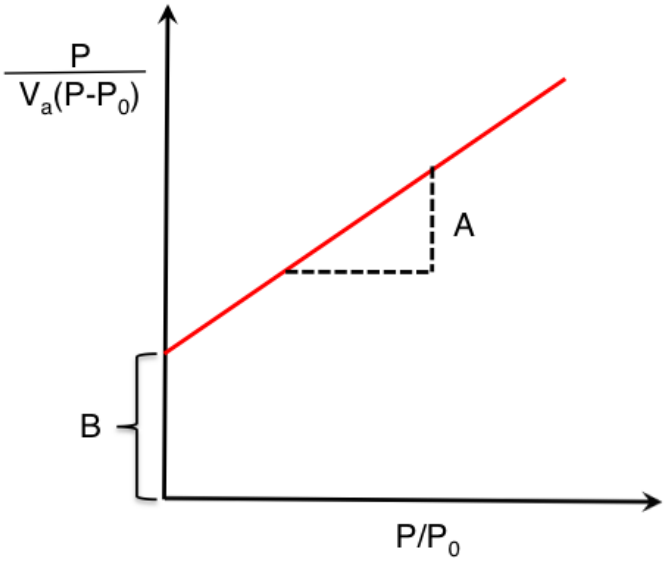

Figure A.3: Brunauer-Emmet-Teller (BET) plot for the calculation of surface area.

$$V_m = \frac{1}{A+B} \tag{A.3}$$

$$C = 1 + A/B \tag{A.4}$$

$$S_{BET} = \frac{V_m N \sigma_0}{m V_a} \tag{A.5}$$

where N is Avogadro's number,

σ_0 is the adsorption cross section of the adsorbate (16.2 nm^2 for nitrogen gas),

and m is the mass of sample in grams.

A.3 Pore Size and Total Pore Volume

To determine surface area, the relative pressure must not exceed a value of 0.4. However, for porosity determination, a full adsorption isotherm and often a desorption isotherms are needed. During adsorption, any micropores present are filled long before the formation of the monolayer. Therefore, at higher pressures mesopores and macropores are filled. As the relative pressure continues to rise, adsorption will take place in multilayers and capillary condensation is observed for mesoporous materials where the mesopores are filled with liquid nitrogen.

The Kelvin equation A.6 is often used to determine pore size. This equation relates the size of the pores to the pressure at which the gas undergoes capillary condensation.

$$ln(\frac{P}{P_0}) = -2\frac{V cos\theta}{r_k RT}; cos\theta = 1 \tag{A.6}$$

where P is the equilibrium vapor pressure within a pore of radius r_k,
P_0 corresponds to the vapor pressure over a flat surface at the same temperature,
is the surface tension of liquid nitrogen,
V is the molar volume of the condensed phase,
θ corresponds to the contact angle of the condensed phase, and
r_k is the radius of curvature of the meniscus of the liquid condensate in the filled pore.

The Barret, Joyner, Halenda method is based on the Kelvin equation where r_k permits the calculation of the radius of the pore using the following assumptions:

i) The pores have cylindrical shape

ii) Fluid-wall interactions are non existent

Prior to condensation, some adsorption has taken place on the pore walls so the actual radius of the pore is given by equation A.6

$$r_p = r_k + t \tag{A.7}$$

where r_p is the actual pore ratio, and
t is the thickness of the adsorbed layer.

The total pore volume is taken from the maximum amount of gas adsorbed at the "top" of the isotherm upon conversion of the gas volume to liquid volume by using a conversion factor (0.00156 for nitrogen).

A.4 Protocol and Composition of Simulated Body Fluid

A.4.1 Composition of SBF

Kokubo *et al.*[4] developed an simulated body fluid that has inorganic ion concentrations similar to those of human extracellular fluid. This fluid is often used for the evaluation of bioactivity of artificial materials *in vitro* as well as a coating of apatite on various materials under biomimetic conditions. Table A.2 shows the ion concentrations of SBF in comparison to those of human blood plasma. This protocol has been adapted from one presented by the Department of Material Chemistry, Graduate School of Engineering, Kyoto University.[5]

Table A.2: Ion concentration of simulated body fluid and human blood plasma (mM)

Ion	Simulated Body Fluid (SBF)	Human Blood Plasma
Na^+	142.0	142.0
K^+	5.0	5.0
Mg^{2+}	1.5	1.5
Ca^{2+}	2.5	2.5
Cl^-	147.8	103.0
HCO_3^-	4.2	27.0
HPO_4^{2-}	1.0	1.0
SO_4^{2-}	0.5	0.5

The pH of SBF is adjusted to pH 7.25 at 36.5°C, by using 50 mM of tris (hydroxymethyl) aminomethane and 45 mM of HCl.

A.4.2 Preparation of SBF

Glassware Cleaning

- Immerse all glassware and bottles in a dilute hydrochloric acid solution for several hours. Remove glassware and rinse with abundant tap water.
- Immerse all glassware and bottles in sterilizing liquid, leave overnight and then rinse with ultra-pure water.
- Wash bottles and glassware with ion-exchanged water for several times, dry and cover their mouths with wrapping film.
- The bottles must be dried below 50°C.

Dissolution of Chemicals

- Add 750 mL of ultra-pure water into a 1000 mL beaker (polyethylene beaker is preferred). Stir and heat to 36.5°C.
- Add each chemical given in Table A.3 into the water until reaching item #8, one by one in the order given in Table , after each reagent was completely dissolved. In order to achieve maximum precision the chemicals must be weighed using a weighing bottle and upon addition of the chemical in the water the weighing bottle must be rinsed with ultra-pure water and added to the solution.
- Add reagent 9 little by little -in portions less than about 1g- in order to avoid local increase in pH of the solution.

Table A.3: Reagents for the preparation of SBF (pH 7.25, 1L)

Order	Reagent	Assay min.	Amount
#1	NaCl	99.5%	7.996g
#2	$NaHCO_3$	99.5%-100.3%	0.350g
#3	KCl	99.5%	0.224g
#4	$K_2PO_4 \cdot 3H_2O$	99.0%	0.228g
#5	$MgCl_2 \cdot 6H_2O$	98.0	0.305g
#6	1M HCl	-	40 mL
#7	$CaCl_2$	95.0% (use after drying at 120° (12 h)	0.278g
#8	Na_2SO_4	99.0%	0.071g
#9	$(CH_2OH)_3CNH_2$	99.9%	6.057g
#10	1M HCl	-	pH adjusting

Adjustment of pH

- Calibrate the pH meter with fresh standard buffer solution. After addition of 9 on the order in Table A.3, measure the pH of the solution while the temperature is at 36.5°C. At this point, pH of the solution is approximately 7.5. Titrate 1 M HCl solution with pipette to adjust the pH to a value of 7.25.

- After adjusting the pH, transfer the solution from the beaker to a 1 litre glass volumetric flask. Wash the inside of the beaker with ultra-pure water several times and add the solution to the flask.

- Adjust the total volume of the solution -by adding water- to 1000 mL, and the shake well.

- Keep the flask at room temperature until it reaches a temperature of approximately 20°C. After cooling, add ultra-pure water again until achieving a total volume of the 1000 mL, and shake well.

Storage

- Rinse a polyethylene (or polystyrene) bottle of 1000 mL with a bit of the prepared solution (SBF), a minimum of three times.
- Transfer the solution from the flask to the polyethylene bottle and store the bottle in a refrigerator at 5-10°C.

Notes

- Examine the stability of the stability of the solution by putting 50 mL of the solution in a polystyrene bottle and place it in incubator at 36.5°C for 2-3 days. Then, check for the formation of any precipitate. If any precipitation would be found, do not use the solution.
- Bottles in which precipitation has occurred must not be used for any further experiments.

REFERENCES

[1] TS Srivatsan, M Gupta, and CYH Lim. *Processing and Fabrication of Advanced Materials XIII*. World Scientific Pub. Co. Inc., 2005.

[2] KSW Sing. Reporting physisorption data for gas/solid systems with special reference to the determination of surface area and porosity. *Pure and Applied Chemistry*, 54:2201–2218, 1982.

[3] S Brunauer, PH Emmet, and E Teller. Adsorption of gases in multimolecular layers. *Journal of the American Chemical Society*, 60:309–319, 1938.

[4] T Kokubo, H Kushitani, S Sakka, T Kitsugi, and T Yamamuro. Solutions able to reproduce in vivo surface-structure changes in bioactive glass-ceramic a-w. *Journal of Biomedical Material Research*, 24:721–734, 1990.

[5] C Ohtsuki. How to prepare the simulated body fluid (SBF) and its related solutions, http://www.life.kyutech.ac.jp/ tmiya/sbf-e.html, [Accessed Jan. 2017].